

國立交通大學

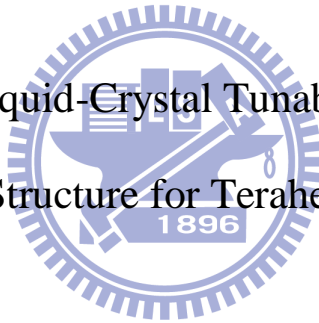
電子物理學系

博士論文

具有週期性光柵結構之可調式

液晶兆赫波元件之研究

Study on the Liquid-Crystal Tunable Devices with
Grating Structure for Terahertz waves



研究生：林家任

指導教授：趙如蘋 教授

潘犀靈 教授

中華民國九十九年五月

具有週期性光柵結構之可調式液晶兆赫波元件之研究

Study on the Liquid-Crystal Tunable Devices with Grating

Structure for Terahertz waves

研 究 生：林家任

Student : Chia-Jen Lin

指 導 教 授：趙如蘋 教授

Advisor : Prof. Ru-Pin Pan

潘犀靈 教授

Prof. Ci-Ling Pan

國 立 交 通 大 學



Submitted to Department of Electrophysics
College of Science
National Chiao Tung University
in Partial Fulfillment of the Requirements
for the Degree of
Doctor of Philosophy
in Electrophysics

May 2010

Hsinchu, Taiwan, Republic of China

中華民國九十九年五月

具有週期性光柵結構之可調式液晶兆赫波元件之研究

學生：林家任

指導教授：趙如蘋 教授

潘犀靈 教授

國立交通大學電子物理學系博士班



近二十年來，兆赫波科技與應用的發展非常迅速，但應用於兆赫波段的可調式元件仍然缺乏。目前大部分的可調式兆赫波元件有著可調範圍過小及操作溫度過低的缺點。我們實驗室發表過利用液晶製作用在兆赫波段並可在室溫操作的可調式元件。根據這些經驗，我們製作出具有光柵結構之可調式液晶元件並探討這些元件於此波段下的性質與研究。

本實驗中，我們架設一套鈦藍寶石為增益介質的飛秒脈衝雷射以用於激發及偵測兆赫波。此飛秒脈衝雷射的特性為擁有 450 mW 的光強度，90MHz 的重複率，及 64 飛秒的脈衝寬度。利用此雷射我們架設一套利用光導天線激發與接收的兆赫波時域分析儀，此套儀器可解

析兆赫波範圍為 0.1-4.0THz。另外，為了探討我們製作元件於兆赫波東方向轉換器的研究，我們利用光纖將兆赫波時域分析儀改良為可移動偵測端，此改良後的裝置可以解析兆赫波範圍為 0.1-1.0THz。相較於使用液態氮冷卻之熱輻射偵測儀測量不同位置之兆赫波訊號，改良後的兆赫波時域分析儀具有可解析寬頻訊號與價格便宜等優點。

本實驗用於設計兆赫波元件的材料為石英玻璃、向列型液晶 E7、MDA-00-3461，利用兆赫波時域分析儀我們發現這些材料在兆赫波段其吸收小且沒有特殊的共振吸收譜線。且此兩款向列型液晶具有高的雙折射性，非常適用於兆赫波段製作可調式元件。經過量測，石英玻璃的折射係數為： $n=1.95$, $\kappa < 0.01$ 。E7 的折射係數為： $n_o = 1.58$, $n_e = 1.71$, $\kappa_o=0.03$, $\kappa_e=0.01$ 。以及 MDA-00-3461 的折射係數為： $n_o = 1.54$, $n_e = 1.72$, $\kappa_o=0.03$, $\kappa_e=0.01$ 。

本實驗利用上述之材料製作具有光柵結構之可調式液晶元件，包含了磁控與電控之液晶相位光柵及兆赫波東方向轉換器。磁控式與電控式之液晶相位光柵可做為可調式之兆赫波分束器。兆赫波東方向轉換器是利用相位延遲器陣列分別調整不同位置的兆赫波相位，使兆赫波具有一梯度的相位差，達到兆赫波轉向的效果。

Study on the Liquid-Crystal-Based Tunable Devices with Grating Structure in Terahertz Range

Student: Chia-Jen Lin

Advisors: Prof. Ru-Pin Pan
Prof. Ci-Ling Pan

Doctor of Philosophy in Department of Electrophysics

National Chiao-Tung University

ABSTRACT

In the past two decades, terahertz photonics and applications have progressed remarkably. However, tunable components in terahertz range are relatively underdeveloped. The present tunable terahertz devices, however, have limited range of tunability and have to be operated at cryogenic temperatures far below room temperature. To conquer the drawbacks, various tunable terahertz devices operated at room temperature based on nematic liquid crystal have been demonstrated in our group. In this work, based on the experience of fabricating the nematic liquid-crystal-based tunable devices, we demonstrated several tunable devices with grating structure to manipulate THz waves.

We constructed a Kerr-lens mode-locking Ti:sapphire laser with maximum power 450 mW, 90 MHz repetition rate, and 64 fs in pulse width. A conventional photoconductive antenna based THz-TDS was constructed that can characterize the broadband terahertz signal in the

range, 0.1 - 4.0 THz. To investigate the terahertz beam steering, an improved THz-TDS with movable detecting part was constructed with an optical fiber. The improved THz-TDS can characterize the terahertz signal below 1.0 THz. It can detect the terahertz pulse directly and can be more convenient and lower cost than that using the liquid-helium-cooled Si bolometer.

We choose the fused silica and nematic liquid crystal E7 and MDA-00-3461 to fabricate our devices. The materials for tunable devices design should have the properties of large birefringence and small absorption. The complex refractive indices of these materials were characterized by the conventional THz-TDS at room temperature 24.5°C. In the THz range, 0.2-2.0 THz, the complex refractive indices of fused silica are $n=1.95$, $\kappa < 0.01$. The ordinary and extraordinary indices of E7 are $n_o = 1.58$, $n_e = 1.71$, $\kappa_o=0.03$, and $\kappa_e=0.01$, and which of MDA-00-3461 are $n_o = 1.54$, $n_e = 1.72$, $\kappa_o=0.03$, and $\kappa_e=0.01$, respectively. In this frequency range, these materials do not show any sharp resonant absorption and clear dispersion. The studies of the optical constants of NLC E7 and MDA-00-3461 in terahertz range show the attractive potential of the applications due to the comparable large birefringence and relative small extinction coefficient.

In this work, we demonstrated several liquid-crystal-based tunable devices with grating structure. These devices including magnetically and electrically controlled phase gratings, and the electrically phase shifter array. We designed the phase gratings that can be utilized as tunable beam splitters, and the phase shift array can be utilized as a beam steerer.

致謝

博士班修業的這段漫漫長路，有許多艱辛難熬的過程，在這一路上，感謝許多人的陪伴與鼓勵，最後才能收成這甜蜜歡樂的果實。

首先我要感謝我的指導教授趙如蘋老師以及潘犀靈老師，沒有他們專業上的指導以及計畫、經費上的支持，這個論文必定無法完成。而且在修業過程，老師耐心、細心教導我注意許多的細節，讓我了解，很多事情的成敗，小細節往往就是最大的關鍵。我想經過博士班的訓練，能將自己大喇喇的個性，轉變成一個夠細心、有耐心的研究人員，這已經是修業過程最大的收穫。

在修業的六年，感謝有很多學長姐、學弟妹的陪伴，每一位都為這段時間添上不同的色彩，為漫長的研究生活帶來歡樂，為枯燥的實驗工作注入能量，讓實驗室的生活不再只是空虛寂寞覺得冷。尤其是一起攻讀博士班的卓帆與宇泰，很高興能遇到兩位聰明、熱情的夥伴。常常在我低潮的時候給我打氣，告訴我要一起完成學業、一起拿畢業證書。在他們身上我也學到了很多，尤其是面對困境，要有克服困難的勇氣，也因此我能獲得博士生最應該擁有的技能—解決問題的能力。並能在遇到問題時，不再只是沮喪逃避，而是能享受克服困難後的成就感。

也在此感謝許多親朋好友在日常生活上的幫助及照顧。尤其是媽媽與哥哥，提供我衣食無憂的生活，並關心我的生活起居，也為我沮喪的時候擔憂操心，並告訴我，自己選擇了一條路，就必須勇往直前，堅持著走下去，並克服困難、達到目標。他們永遠是我最堅強的後盾，只要我自己不倒下，他們永遠都會扶持我。希望我這一點點小小的成就能讓他們感到欣慰。

最後，將我這份小小的榮耀與大大的喜悅，獻給在天上一直眷顧著我的父親，願他與我分享。

家任 2010/5/7

Contents

摘要.....	i
ABSTRACT	iii
致謝.....	v
Contents.....	vi
List of tables.....	viii
List of figures.....	viii
Chapter 1 Introduction	1
1-1 Terahertz technology and applications.....	1
1-2 Liquid crystals	3
1-2.1 Introduction to liquid crystals	3
1-2.2 Liquid crystal structure	5
1-2.3 Liquid crystal applications	7
1-3 Motivation	7
1-4 Organization of dissertation	8
Reference	10
Figures	14
Chapter 2 Experimental Apparatus and Principles.....	16
2-1 Ti:sapphire Pulsed Laser	16
2-1.1 Mode-locking technique	16
2-1.2 Experimental Ti:sapphire Laser Construction and Properties	19
2-1.3 Interferometric autocorrelator for pulse width measurement	20
2-2 Principles of Terahertz Time-domain Spectrometer.....	21
2-2.1 Generation of terahertz wave by using photoconductive antennas.....	22
2-2.2 Detection of terahertz wave by using photoconductive antennas.....	24
2-2.3 Terahertz time-domain spectroscopy (THz-TDS)	26
2-3 Principles of NLC alignment and deformation	27
2-3.1 Rubbing alignment method and chemical alignment method.....	28
2-3.2 Deformation and operation principle of NLC molecules..	29
Tables.....	31

Reference	32
Figures	35
Chapter 3 Optical Constants of Nematic Liquid Crystal in Terahertz	
Range.....	43
3-1 Experimental procedure	43
3-2 Optical constants determination	44
3-3 Results and discussions	48
3-3.1 Optical constants of fused silica substrates	48
3-3.2 Optical constants of NLC E7	49
3-3.3 Optical constants of NLC MDA-00-3461	50
3-4 Summary.....	51
Tables.....	52
Reference	53
Figures	54
Chapter 4 Manipulating Terahertz Wave by Nematic-Liquid-Crystal Based Grating structure devices	59
4-1 Magnetically controlled phase grating.....	60
4-1.1 Diffraction theory.....	60
4-1.2 Experimental method and setups	61
4-1.3 Results and discussions	63
4-1.4 Summary	66
4-2 Electrically controlled phase grating	67
4-2.1 Experimental method and setups	67
4-2.2 Insertion loss analysis.....	68
4-2.3 Results and discussions	69
4-2.4 Summary	74
4-3 Electrically controlled beam steerer	75
4-3.1 Experimental principles.....	75
4-3.2 Experimental method and setups	77
4-3.3 Results and discussions	79
4-3.4 Summary	80
Tables.....	82
Reference	83
Figures	86
Chapter 5 Conclusions and Future Work.....	107
Conclusions.....	107
Future work.....	109
Publication List.....	111

Curriculum Vitae	115
------------------------	-----

List of Tables

Table 2-1 Characteristics of photoconductive substrates	31
Table 3-1 NLC Data sheet from Merck Corp.	52
Table 4-1. Parameters of the fused silica and NLC E7	82
Table 4-2. Insertion loss of phase grating	82
Table 4-3 Control voltage and corresponding phase shift at 0.3 THz.....	82

List of Figures

Chapter 1

Figure 1-1 Electromagnetic spectrum.....	14
Figure 1-2 Applications of THz technology	14
Figure1-3 Regulated spectrum as designated by the U.S. Federal Communications Commission	15
Figure 1-4 Different types of LC: (a) nematic, (b) smetic, and (c) cholesteric.....	15

Chapter 2

Figure 2-1 Active mode-locking method with AO modulator.....	35
Figure 2-2 Passive mode-locking method with saturable absorber	35
Figure 2-3 Kerr-lens mode-locking method with hard aperture	36
Figure 2-4 Absorption and emission spectra of Ti:sappire	36
Figure 2-5 Construction of Ti:sappire pulsed femtosecond laser	37
Figure 2-6 Spectrum of mode-locked pulse.....	37
Figure 2-7 Pulse train of Ti:sappire pulsed femtosecond laser.	38
Figure 2-8 Photograph and schematic diagram of interferometric autocorrelator.....	38
Figure 2-9 Autocorrelation signal of Ti:sappire pulsed femtoscond laser.	39
Figure 2-10 Photoconductive antenna (Hertzian dipole antenna).	39
Figure 2-11 Calculated photocurrent in emitting photoconductive antenna and amplitude of THz field versus time.....	40
Figure 2-12 Schematic diagram of THz-TDS.....	40
Figure 2-13 Time domain THz signal measured by THz-TDS.	41
Figure 2-14 Power spectra of THz signal in frequency domain.	41
Figure 2-15 Surface alignment treatments: (a) rubbing method for homogeneous alignment, and (b) chemical treatment method for	

homeotropic alignment	42
Figure 2-16 Three different types of deformation occurring in NLC cell	42
Chapter 3	
Figure 3-1 Fundamental concept of complex refractive index measurement	54
Figure 3-2 THz beam path of (a) LC test cell, and (b) reference cell	55
Figure 3-3 Complex refractive indices of 1.0mm-thick fused silica	56
Figure 3-4 Complex refractive indices of 3.0mm-thick fused silica	56
Figure 3-5 Photographs of NLC E7 cell under crossed-polarizers with darkness-state and brightness-state.....	57
Figure 3-7 Photographs of NLC MDA-00-3461 cell under crossed-polarizers with darkness-state and brightness-state	58
Chapter 4	
Figure 4-1 Schematic of a generic binary phase grating	86
Figure 4-2 (a) Experimental setup; H: magnetic field, MHA: metallic hole array used as narrow band filter. (b) Construction of the LC phase grating; dimensions are shown	86
Figure 4-3 Construction of setup for grating diffraction profile measurement	87
Figure 4-4 Temporal profiles of the 0th order diffracted THz pulses through the phase grating and that of a reference sample	87
Figure 4-5 Diffraction efficiencies of the 0th order as a function of frequency.	88
Figure 4-6 Diffraction efficiencies as a function of diffraction angle (θ) for the 0.3 THz-beam.....	89
Figure 4-7 Polarization beam splitting using the LC phase grating. (a) Magnetic field was in the y-direction. (b) Magnetic field was in the z-direction.....	90
Figure 4-8 Schematic structure of the electrically controlled THz NLC phase grating.....	91
Figure 4-9 Time-domain (a) and spectral-domain (b) characteristics of the device	92
Figure 4-10 (a) FDTD simulation and (b) Experimental results of the frequency dependence of the 0 th diffraction efficiencies of the phase grating operated at four applied voltages.....	93
Figure 4-11 FDTD simulation - diffraction efficiency as a function of frequency for different thickness (a) o-wave (b) e-wave.	94
Figure 4-12 Diffraction efficiency as a function of diffraction angle for	

the 0.3-THz-beam	95
Figure 4-13 Dffraction efficiency of the devices (a) $h=17.5\text{mm}$ (b) $h=7.5\text{mm}$	96
Figure 4-14 Signal profiles in time domain. The turn-on and turn-off times are measured by monitoring the pulse signal (electric field) variation in time domain with THz-TDS. The monitoring position of THz-TDS for response time measurement is shown.....	97
Figure 4-15 Response time of phase grating (a) turn-on (b) turn-off	98
Figure 4-16 Schematic structure of the electrically controlled THz phase shifter array.....	99
Figure 4-17 Improved THz-TDS. Probe beam is guided with a 1m-long optical fiber directly to the antenna	100
Figure 4-18 Comparison of THz signals in time domain between probe beam in free space (black line) and fiber-guided (red line).....	100
Figure 4-19 Comparison of THz spectra in frequency domain between probe beam in free space (black line) and fiber-guided (red line).....	101
Figure 4-20 Transmitted properties of grating structure. S-state or P-state is represented the polarization of THz wave (P) perpendicular or parallel to the electrodes, respectively.....	102
Figure 4-21 Extinction ratio between P-state and S-state	102
Figure 4-22 THz signal delay in time domain	103
Figure 4-23 Spectra of phase shift of THz signal	103
Figure 4-24 Phase shift at 0.3 THz as a function of the control voltage.	104
Figure 4-25 THz signals before steered at $\theta=0^\circ$: (a) without sample; with sample (b) at no-state, (c) at ne-state; steered signals at $\theta=8.5^\circ$: (d) sample applied voltage to yield gradient phase, (e) without sample.....	105
Figure 4-26 Spectra of THz signals before steered at $\theta=0^\circ$: (a) without sample; with sample (b) at no-state, (c) at ne-state; steered signals at $\theta=8.5^\circ$: (d) sample applied voltage to yield gradient phase, (e) without sample.....	106

Chapter 1 Introduction

1-1 Terahertz technology and applications

The terahertz (THz) regime ranges from 0.1 THz to 10 THz, where 1 THz equals 33 wave numbers, 300 μ m in wavelength, or 4meV in photon energy. In the past two decades, THz waves are very difficult to generate and detect. For lower frequencies in the spectrum, e.g., microwaves and millimeter-waves can be exploited by electronic devices (up to about 100GHz). For higher frequencies, e.g., near-infrared and visible light are investigated by optical devices. THz wave is in the region of the electromagnetic spectrum between microwaves and infrared light (Fig. 1.1 [1]). This regime is deficient in generators and detectors, and forms “THz gap” in the electromagnetic spectrum until the mid-80s.

The dramatic developments in semiconductor physics and ultrafast laser system, especially those of femtosecond laser pulses, ultrafast photoconductive thin films, and semiconductor quantum structures, have fostered THz technology advance in the 1990s. The first sub-100fs solid-state laser was developed by Spence et al. in 1991 [2]. In 1999, mode-locking techniques are effective over such a large bandwidth that the resulting pulses can have duration of 6 fs or shorter [3]. With the ultrashort pulses incident into suitable semiconductor materials, the electron-hole pairs will be generated quickly, results photocurrent pulses, this acceleration processes will generate electromagnetic waves, with frequency lies in the THz range. In 1980, Auston [4] successfully used the

photoconductive dipole antenna to generate and detect coherently THz radiation in time domain, and this technology is called THz time-domain spectroscopy (THz-TDS). Other THz radiation generation methods, such as optical rectification [5,6], surge current in semiconductor surface [7], had been investigated.

THz technology has advanced rapidly in many diverse fields including ultrafast dynamics in materials, biomedical imaging, environmental surveillance, and communication (Fig 1-2) [1,8-10]. For the dynamics in materials investigation, THz spectroscopy provides information on the basic structure of molecules due to rotational frequencies of light molecules fall in this spectral region. Vibration modes of large molecules with many functional groupings, including many biologic molecules have broad resonances at THz frequencies.

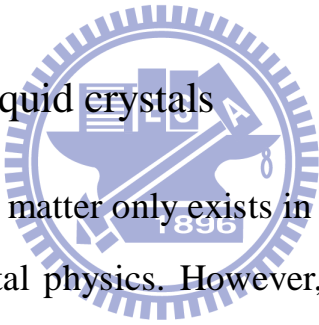
For biomedical imaging application and environmental surveillance uses, THz radiation can penetrate a wide range of materials such as human tissue, clothing, paper, plastic, and ceramics without ionizing (unlike X-rays). It is owing to the low electromagnetic energy that THz wave is not expected to damage biological cells. The THz-TDS could supply amplitude and phase information that makes 3-D imaging possible. These properties open up a variety of future commercial opportunities of which security and medical imaging applications offer the greatest potential. THz imaging applications are foreseen in drug discovery and non-destructive testing of foodstuffs, coatings, and semiconductor chips.

THz communication can mean communication with a THz carrier wave. According to Federal Communications Commission, the

frequencies above 300 GHz are currently unallocated as shown in the U.S. Frequency Allocation chart (Fig. 1-3). THz communication is in the very early stages of development. The availability of the frequency band and the communications bandwidth make communications at THz frequencies very attractive. The advantages of using THz technology are the larger bandwidth and therefore higher transmission rate as compared to microwave communications, without having to switch to a different set of hardware such as lasers for optical communications.

1-2 Liquid crystals

1-2.1 Introduction to liquid crystals



People are taught that matter only exists in three states as solid, liquid, and gas in the fundamental physics. However, certain organic materials do not show a single transition from solid to liquid, but exist transition of new phases. These phases have the mechanical properties and symmetry properties intermediate between those of isotropic liquid phase and crystalline solid phase. Therefore, the materials with these properties are called liquid crystals (LCs). The first observation and discovery of liquid crystal (LC) behavior were made in cholesteryl benzoate by Reinitzer and Lehmann in the end of 19th century [11, 12]. LCs arise under certain conditions in organic substances having sharply anisotropic molecular structure which is elongated (rod-like) or flat (disc-like) structure. In this study, the LC molecules are utilized the rod-like structure.

There are three basic phases of LCs, known as nematic phase, smectic phase, and cholesteric phase as shown in Fig. 1-4 [13, 14]. Figure 1-4 (a) illustrates the nematic phase. The nematic phase has the following features:

1. The centres of gravity of the molecules have no long-range order. The correlations in position between the centres of gravity of neighboring molecules are similar to those existing in a conventional liquid.
2. There is some order in the direction of the molecules. They tend to be parallel to some common axis, labeled by a unit vector (or director) \mathbf{n} . This is reflected in all macroscopic tensor properties. Optically, a nematic is a uniaxial medium with the optical axis along \mathbf{n} . In all known cases, there appears to be complete rotational symmetry around the axis \mathbf{n} .
3. The direction of \mathbf{n} is arbitrary in space, and it is imposed by minor forces such as the guiding effect of the walls of the container.
4. The states of \mathbf{n} and $-\mathbf{n}$ are indistinguishable.
5. Nematic phases occur only with materials that do not distinguish between right and left, either each constituent molecule must be identical to its mirror image (achiral).

In summary, nematic liquid crystal (NLC) is uniaxial molecule and its orientation could be effected by minor force. With these characteristics, the NLC is optically and electrically anisotropic.

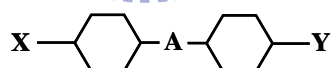
Smectics are layered structures with a well-defined interlayer spacing as shown in Fig. 1-4 (b) that can be measured by X-ray diffraction.

Smectics are thus more ordered than nematics. For a given material, the smectic phase usually occurs at temperatures below the nematic phase, and possesses the highest degree of order.

The cholesteric phase is also nematic type of LC except that it is composed of chiral molecules. As a result, the structure acquires a spontaneous twist about a helical axis normal to the director. The twist may be right-handed or left-handed depending on the molecular chirality. Figure 1-4 (c) illustrates the cholesteric phase of LC by viewing the distribution of molecules at several planes that are perpendicular to the helical axis.

1-2.2 Liquid crystal structure

Typical rod-like LC molecule has the following general molecular structure:



where X and Y are terminal groups and A is a linking group between two or more ring systems. The contribution of each group is discussed as follows.

Ring Systems. The rings can be either benzene rings (unsaturated) or cyclohexanes, or combination of both. The presence of the ring system is essential in most LCs that contains at least one ring (either phenyl or cyclohexyl). It is important to note that only σ electrons exist in cyclohexyl rings, whereas π electrons exist in phenyl rings. The presence of the rings provides the short range intermolecular forces needed to form

the nematic phase. They also affect the absorption, dielectric anisotropy, birefringence, elastic constants and viscosity.

Terminal Group X (Also called side chain). There are three common X-terminal groups: (1) alkyl chain C_nH_{2n+1} , (2) alkoxy chain $C_nH_{2n+1}O$, and (3) alkenyl chain that contains a double bond. The length of the chain can significantly influence the elastic constants of the nematic phase as well as the phase transition temperature. For short chains with one or two carbon atoms ($n=1,2$), the molecules are too rigid to exhibit LC phases. Terminal groups with medium chain length (e.g. $n=3-8$) are most suitable for nematic phases. Compounds with even longer chain length can exist smectic phases. Generally speaking, the melting point decreases with the increasing chain length. However, some compounds are irregular and unpredictable. The nematic-isotropic transition temperature (known as the clearing point) for LC compounds with an even number of carbon atoms. This is known as the “odd-even effect.”

Linking Group A. The linking group can be a single bond between the two rings. The generic name of these LCs is biphenyl. In case of an additional ring as the linking group, the generic name of these LCs is terphenyl. Some common linking groups are C_2H_4 (diphenylethane), C_2H_2 (stilbene), $-C\equiv C-$ (tolane), and $-N=N-$ (azobenzene).

Terminal Group Y. The terminal group Y plays an important role in determining the dielectric constants ϵ and its anisotropy $\Delta\epsilon$. For liquid crystal display application (LCD), the operation voltage is commonly a multiple of the threshold voltage, which is the minimum voltage required to induce a reorientation of the LC molecules. It is known that the

threshold voltage is inversely proportional to the square root of the dielectric anisotropy. Thus it is desirable to have a large $\Delta\epsilon$ for low voltage operations. The terminal group Y can be either polar or nonpolar. Nonpolar terminal group Y such as the alkyl chain C_nH_{2n+1} has very little effect on the dielectric anisotropy. On the other hand, a polar terminal group can contribute significantly to the dielectric anisotropy. Some common polar terminal groups Y include CN, F and Cl.

1-2.3 Liquid crystal applications

The most well-known LC device is the flat panel display which is revolutionary commercial success [15, 16]. Otherwise, the unique properties of LCs are also proper to fabricate and design tunable optical components, such as tunable lenses, filters, phase gratings and light valves [16-18]. Recently, studies of LCs properties were interested in millimeter wave and THz range [19-21], and followed various tunable devices in millimeter and THz ranges employing NLC, such as phase shifters, filters, and switches that are controlled either electrically or magnetically were demonstrated [22-27].

1-3 Motivation

In the past decades, THz photonics have progressed remarkably. However, essential quasi-optic components such as phase shifters, modulators, attenuators, polarizers, and beam splitters in the THz range

are relatively underdeveloped. For controlling electromagnetic waves, the periodic structures such as gratings are the commonly candidates. In the THz range, the tunable devices based on optically and electrically controlled carrier concentration in quantum-well structures are demonstrated [28-30]. These tunable THz devices, however, have limited range of tunability and have to be operated at cryogenic temperatures far below room temperature. To conquer the drawbacks, various tunable THz devices based on NLC, such as phase shifters and filters that are controlled either electrically or magnetically at room temperature, have been demonstrated in our group [25-27].

In this work, based on the experience of fabricating the NLC-based tunable devices, we demonstrated several tunable devices with grating structure to manipulate THz waves. These devices including magnetically and electrically controlled phase gratings, and the electrically phase shifter array. We designed the phase gratings that can be utilized as tunable beam splitters, and the phase shift array can be utilized as a beam steerer.

1-4 Organization of dissertation

This dissertation is divided into five chapters. In addition the introduction in chapter 1, the other chapters are arranged as following.

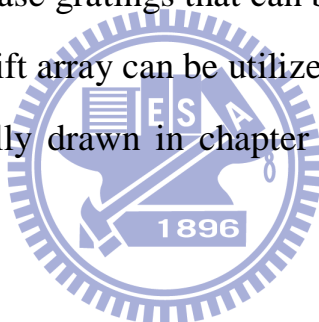
In chapter 2, we introduce the main experimental setups including the constructions of the Kerr-lens mode-locking Ti:sapphire laser and the THz time domain spectrometer (THZ-TDS). The properties of the ultrafast

laser and THz-TDS are described. The principles of NLC alignment and the fabrication processes are also down in this chapter.

In chapter 3, we introduce the properties of materials used in this work including fused silica substrate and two types of NLC. The complex refractive indices of these materials are characterized by the THz-TDS. We will introduce these materials that have the characteristics suitable in THz range.

In chapter 4, we demonstrated several tunable devices with grating structure to manipulate THz waves. These devices including magnetically and electrically controlled phase gratings and the electrically phase shifter array. We designed the phase gratings that can be utilized as tunable beam splitters, and the phase shift array can be utilized as a beam steerer.

Conclusions are finally drawn in chapter 5, along with suggestions for future research.



Reference

- [1] Michael J. Fitch and Robert Osiander, "Terahertz Waves for Communications and Sensing," *Johns Hopkins Apl Technical Digest*, 25, 4, 2004.
- [2] D. E. Spence, P. N. Kean, and W. Sibbett, "60-fsec pulse generation from a self-mode-locked Ti:sapphire laser," *Opt. Lett.*, 16, 42, 1991.
- [3] D. H. Sutter, G. Steinmeyer, L. Gallmann, N. Matuschek, F. Morier-Genoud, and U. Keller, "Semiconductor saturable-absorber mirror-assisted Kerr-lens mode-locked Ti:sapphire laser producing pulses in the two-cycle regime," *Opt. Lett.*, 24, 631, 1999.
- [4] D. H. Auston, K. P. Cheung, and P. R. Smith, "Picosecond photoconducting Hertzian dipoles," *Appl. Phys. Lett.*, 45, 284, 1984.
- [5] X.-C. Zhang, Y. Jin, and X. F. Ma, "Coherent measurement of THz optical rectification from electro-optic crystals," *Appl. Phys. Lett.* 61, 2764, 1992.
- [6] A. Rice, Y. Jin, X. F. Ma, and X.-C. Zhang, "Terahertz optical rectification from <110> zinc-blende crystals," *Appl. Phys. Lett.*, 64, 1324, 1994.
- [7] X.-C. Zhang, and D. H. Auston, "Optoelectronic measurement of semiconductor surfaces and interfaces with femtosecond optics," *J. Appl. Phys.*, 71, 326, 1992.
- [8] Masayoshi Tonouchi, "Cutting-edge terahertz technology," *Nature photonics*, 1, 97, 2007.
- [9] Clery, Daniel, "Brainstorming Their Way to An Imaging Revolution."

Science, 297, 761, 2002.

[10] T. Kleine-Ostmann, K. Pierz, G. Hein, P. Dawson, and M. Koch, “Audio signal transmission over THz communication channel using semiconductor modulator,” *Electron. Lett.*, 40, 2, 2004.

[11] F. Reinitzer, *Monatsch Chem.*, 9, 421, 1888.

[12] O. Lehmann, *Z. Physik. Cham.*, 4, 462, 1989.

[13] Pochi Yeh, and Claire Gu, “Optics of Liquid Crystal Displays,” A Wiley Interscience Publication, John Wiley & Sons, Inc.

[14] P. G. De Gennes, and J. Prost, “The Physics of Liquid Crystals,” second edition, Clarendon Press, Oxford, 1993.

[15] M. Schadt and W. Helfrich, “Voltage-Dependent Optical Activity of a Twisted Nematic Liquid Crystal,” *Appl. Phys. Lett.*, 18, 127, 1971.

[16] R. S. McEwen, “Instrument science and Technology,” *J. Phys. E: Sci. Instrum.*, 20, 364, 1987.

[17] J. Chen, P. J. Bos, H. Vithana, and D. L. Johnson, “An electro-optically controlled liquid crystal diffraction grating,” *Appl. Phys. Lett.*, 67, 2588, 1995.

[18] E. P. Raynes and I. A. Shanks, “Fast-Switching Twisted Nematic Electro-Optical Shutter and Colour Filter,” *Electron. Lett.* 10, 114, 1974.

[19] T. Nose, S. Sato, K. Mizuno, J. Bae, and T. Nozokido, “Refractive Index of Nematic Liquid Crystal in the Submillimeter Wave Region,” *Appl. Opt.*, 36, 6383, 1997.

[20] D. Turchinovich, P. Knobloch, G. Luessem, and M. Koch, “THz time-domain spectroscopy on 4-(trans-4-pentylcyclohexyl)-benzotrinitrile,” *Proc. SPIE*, 4463, 65, 2001.

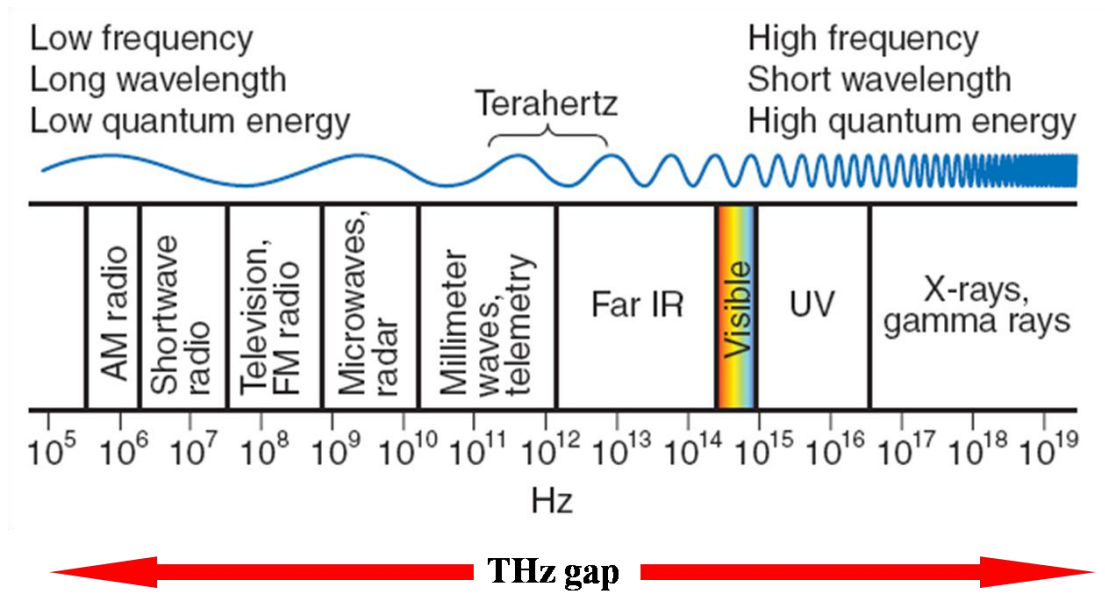
- [21] R. P. Pan, C. F. Hsieh, C. L. Pan, and C.Y. Chen, "Temperature-dependent optical constants and birefringence of nematic liquid crystal 5CB in the terahertz frequency range," *J. Appl. Phys.*, 103, 093523, 2008.
- [22] K. C. Lim, J. D. Margerum, A. M. Lackner, L. J. Miller, E. Sherman, and W. H. Smith, "Liquid crystal birefringence for millimeter wave radar," *Liq. Cryst.*, 14, 327 1993.
- [23] H. Fujikake, T. Kuki, H. Kamoda, F. Sato, and T. Nomoto, "Voltage-variable microwave delay line using ferroelectric liquid crystal with aligned submicron polymer fibers," *Appl. Phys. Lett.*, 83, 1815, 2003.
- [24] F. Yang and J. R. Sambles, "Microwave liquid-crystal variable phase grating," *Appl. Phys. Lett.*, 85, 2041, 2004.
- [25] H.-Y. Wu, C.-F. Hsieh, T.-T. Tang, R.-P. Pan, and C.-L. Pan, "Electrically Tunable Room-Temperature 2π Liquid Crystal Terahertz Phase Shifter," *IEEE Photonic Technology Lett.*, 18, 1488, 2006.
- [26] C.-Y. Chen, C.-F. Hsieh, Y.-F. Lin, C.-L. Pan, and R.-P. Pan, "Liquid-crystal-based terahertz tunable Lyot filter," *Appl. Phys. Lett.*, 88, 101107, 2006.
- [27] I.-C. Ho, C.-L. Pan, C.-F. Hsieh, and R.-P. Pan, "A Liquid-Crystal-Based Terahertz Tunable Solc Filter," *Opt. Lett.*, 33, 1401, 2008.
- [28] I. H. Libon, S. Baumgärtner, M. Hempel, N. E. Hecher, and J. Feldmann, "An optically controllable terahertz filter," *Appl. Phys. Lett.*, 76, 2821, 2000.
- [29] T. Kleine-Ostmann, P. Dawson, K. Pierz, and G. Hein, and M. Koch,

“Room-temperature operation of an electrically driven terahertz modulator,” *Appl. Phys. Lett.*, 84, 3555, 2004

[30] R. Kersting, G. Strasser, and K. Unterrainer, “Terahertz phase modulator,” *Electron. Lett.*, 36, 1156, 2000.



Figures



Electronics **Photonics**

Figure 1-1 Electromagnetic spectrum. THz wave locates between microwaves and infrared light.

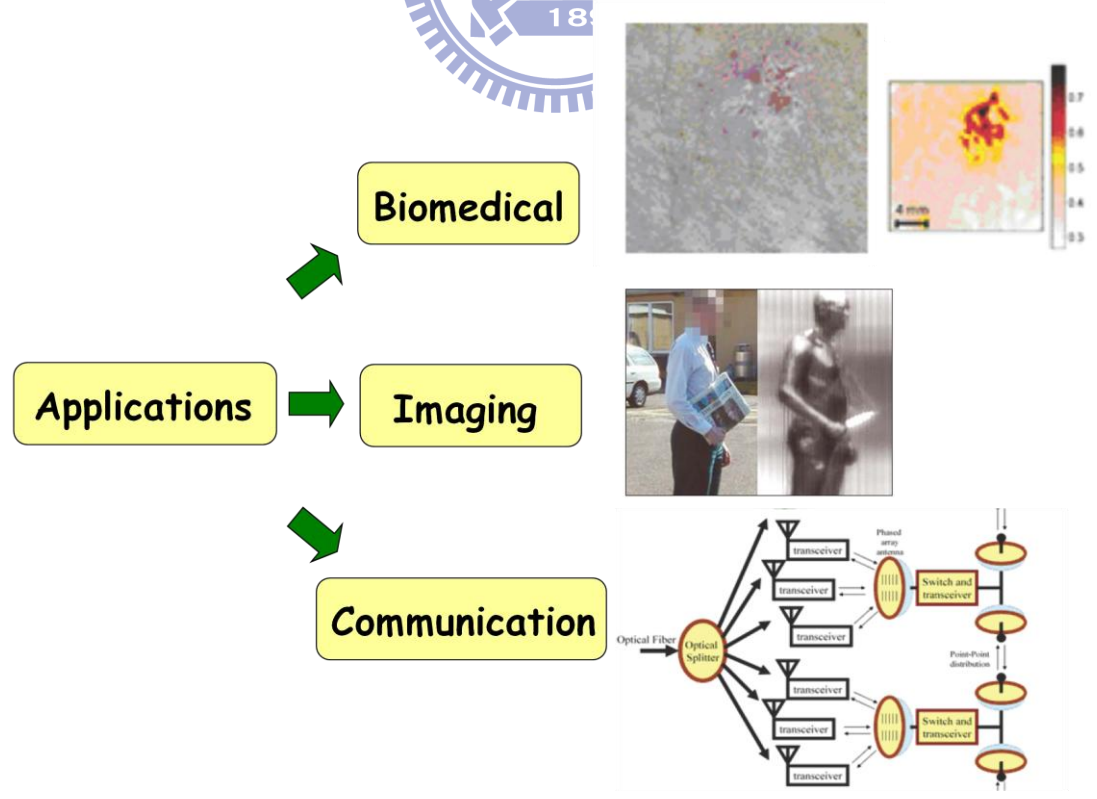


Figure 1-2 Applications of THz technology

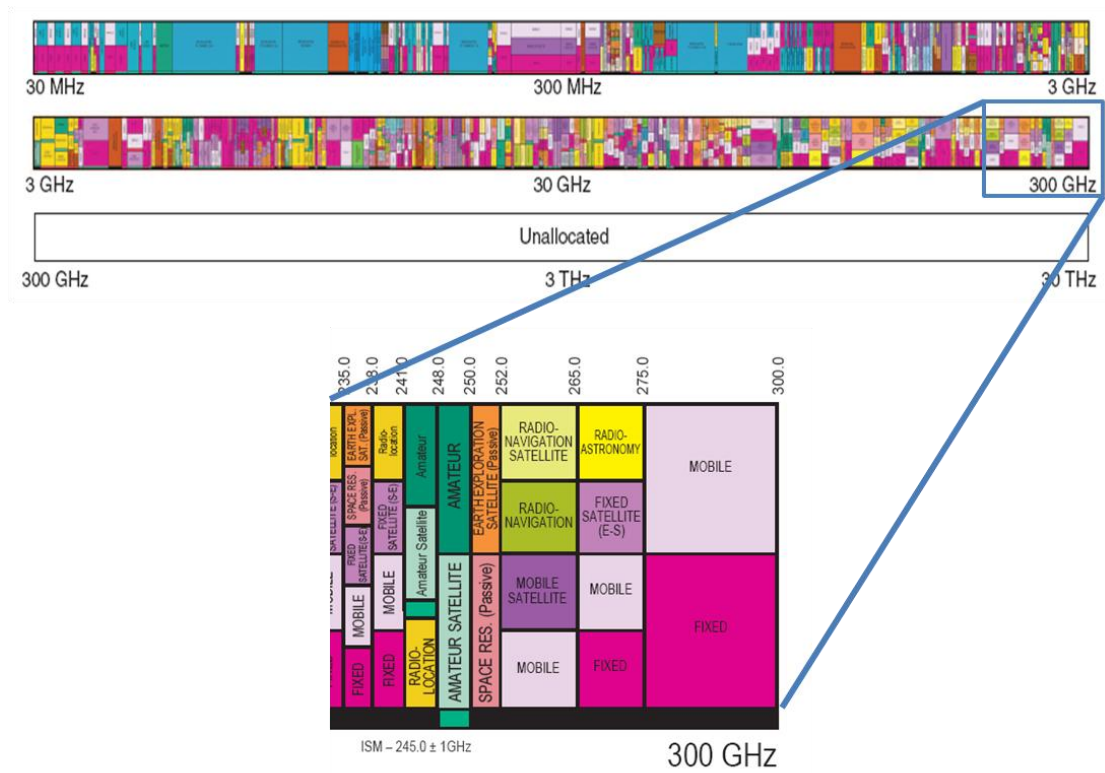


Figure1-3 Regulated spectrum as designated by the U.S. Federal Communications Commission

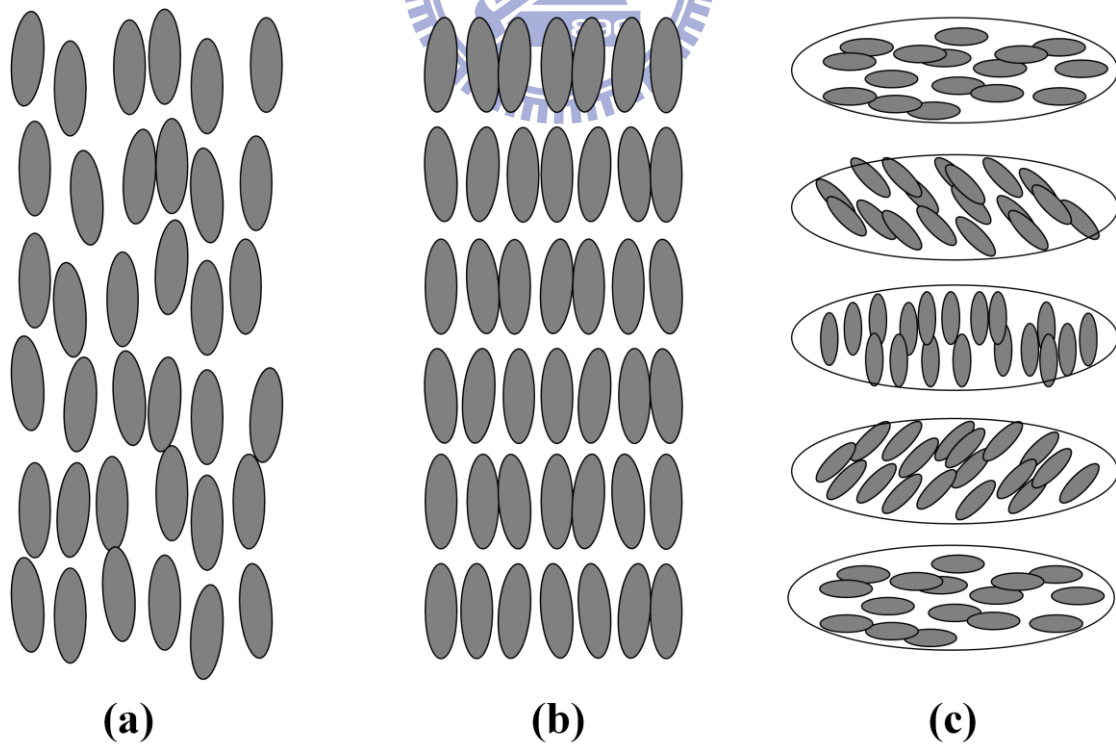


Figure 1-4 Different types of LC: (a) nematic, (b) smetic, and (c) cholesteric

Chapter 2 Experimental Apparatus and

Principles

2-1 Ti:sapphire Pulsed Laser

Ultrashort pulsed laser is a powerful tool for studying in ultrafast phenomena. The Ti:sapphire pulsed laser was first constructed by Moulton in 1982 and it was the best candidate to investigate the ultrafast phenomena [1]. The Ti:sapphire laser is tunable laser which emit red and near-infrared light in the range from 650 to 1100 nm. It has the properties of broad gain bandwidth, high saturate power intensity, high quantum efficiency, and high damage threshold.



2-1.1 Mode-locking technique

Mode-locking technique is the fundamental concept for generating ultrashort pulse. In general, the output of laser beam is not a single, pure frequency or wavelength. The gain medium of laser primarily determines the bandwidth of the output beam, and the range of operating frequencies is known as the gain bandwidth. Secondly, the resonant cavity of the laser also determines the emission frequencies. The discrete frequencies exit in the resonant cavity as standing waves are known as the longitudinal modes of the cavity. If a laser has a larger gain bandwidth, it would also have more emission modes. In a simple laser, the longitude modes do not

have a fixed relationship between each other. These modes oscillate independently. Therefore, the laser emits random fluctuations in intensity, and interference effects between the modes tend to average to a near-constant output intensity. The laser operation is known as a continuous wave (CW). On the other hand, if the resonant modes have a fixed relationship between each other, the modes of the laser will periodically all constructively interfere with one another, producing an intense pulse of light. Such laser is known as mode-locked or phase-locked laser.

Mode-locking methods are mainly classified as active mode-locking and passive mode-locking. Active mode-locking involves using the periodic modulation of the resonator losses or of the gain of the amplifying medium. The most common active mode-locking method places a standing wave acousto-optic (AO) modulator into the laser cavity as schematic diagram shown in Fig. 2-1. If the modulation is synchronized with the resonator round trips, this can lead to the generation of ultrashort pulses, usually with picosecond pulse durations.

Passive mode-locking method does not require a signal external to the laser to generate pulses. With this method, we use the light in the cavity to cause a change in some intra-cavity element, which will then itself produce a change in the intra-cavity light. The most common type of device which will do this is a saturable absorber as schematic diagram shown in Fig. 2-2. Passive mode locking allows the generation of femtosecond pulses, basically because a saturable absorber, which is driven by already short pulses, can modulate the resonator losses much

faster than electronic modulators.

In our experiment, we use the Kerr-lens mode-locking method to construct our ultrashort pulse laser. Kerr-lens mode-locking (KLM) is a passive mode-locking technique using a nonlinear optical process known as the optical Kerr effect [2]. The gain medium is nonlinear, and its refractive index is a function of the intensity: $n = n_0 + n_2I$. The Gaussian wave does not feel a homogeneous refractive index as it passes through the medium. If n_2 , the nonlinear coefficient of the refractive index, is positive, the refraction is stronger on the axis of the beam than away from it. So the amplifying medium behaves like a converging lens and focuses the beam just like a lens (Kerr lens). It is known as the phenomenon of self-focusing. However, self-focusing is proportionally more important for strong intensities. This means that the strong intensity maxima of the laser cavity will be much more strongly focused than the weaker ones, for which focusing will be negligible.

The KLM laser should be designed to favor the pulsed regime over the CW one. When an aperture placed at a proper position in the resonant cavity, the CW mode, which has larger spot size, will be cut off. On the other hand, KLM pulse, which has smaller spot size, will be amplified in the cavity. This concept is known as hard aperture effect as schematic diagram shown in Fig. 2-3. Furthermore, if the overlap between the pumped beam and the pulses in the cavity aligned well, the KLM pulse with smaller spot size will have higher gain than that of CW mode with larger spot size. With this effect, the laser will have self amplitude modulation [3], and this concept is known as soft aperture effect.

Therefore, the combination of the self-focusing Kerr effect with an intracavity aperture is equivalent to a fast response saturable absorber.

2-1.2 Experimental Ti:sapphire Laser Construction and Properties

The Heisenberg uncertainty principle states that there is a limit to the information we can acquire about conjugate variable of a system. Therefore, our simultaneous knowledge of both the time, t , and frequency ω , of a system is limited:

$$\Delta t \times \Delta \omega \geq \frac{1}{2}. \quad (2-1)$$

The construction of the ultrashort duration pulse laser requires a very broadband emission gain medium. In the past decades, the most spectacular advances in laser physics and in the field of ultrashort light pulse generation have been based on the development of titanium-doped aluminum oxide (Ti:Al₂O₃, Ti:sapphire) as gain medium [4, 5]. Figure 2-4 shows the normalized absorption and emission spectra of Ti:sapphire gain medium.

Our femtosecond laser system is shown as the schematic diagram in Fig. 2-5. The pump laser for the Ti:Sapphire laser (Kapteyn-Murnane Laboratories L. L. C.) is a 4.5W frequency doubled diode-pumped Nd:YVO₄ laser (Millennia Vs, Spectra-Physics) with a wavelength $\lambda = 532$ nm. The pump beam is focused by the lens ($f = 10$ cm, 532nm AR-coated) and the concave lens R₁ on the Ti:sapphire rod. The excited Ti:sapphire rod emits fluorescence lights with wavelength about 800nm which are collected by the concave lenses R₁ and R₂ (R=10cm, 532nm

AR-coated, 800nm HR-coated). One beam of the fluorescence lights from R_1 is propagated through a prism pair for dispersion compensation to the high reflection mirror R_4 , and the beam is retraced in the same optical path. The other beam from R_2 is propagated to the output coupler (OC) R_3 , and is retro-reflected and restrained in the resonant cavity. When the Ti:sapphire laser starts lasing, the output beam is CW mode, and the maximum power can reach 600~700 mW, and the wavelength can be tuned from 770nm to 830nm. Further, adjust the positions of R_1 , R_2 , and Ti:sapphire rod, meanwhile observes the output spectrum. Once, the spectrum broadening is recognized, which means the soft-aperture effect of KLM constructed successfully. The output power can reach 450~550 mW, the wavelength is centered at 820nm with about 30nm bandwidth. The spectrum of output pulse is shown as Fig. 2-6. Figure 2-7 shows the pulse train displayed on an oscilloscope, which reveals the repetition rate is about 90MHz. There is another prism pair for dispersion compensation outside the cavity.

2-1.3 Interferometric autocorrelator for pulse width measurement

The pulse duration of the ultrafast laser cannot easily be measured by optoelectronic methods, since the response time of photodiodes and oscilloscopes are at the best of a few hundreds of femtoseconds. Interferometric autocorrelator is commonly utilized to estimate the

duration of ultrashort pulses [6]. The n-th order autocorrelation function of a given electromagnetic field can be described as,

$$I_n(\tau) = \int_{-\infty}^{+\infty} \{|E(t) + E(t - \tau)|^2\}^n dt. \quad (2-2)$$

In our laboratory, we use a two-photo absorption photodiode (GaP, G1961, from Hamamatsu) as the detector to construct a second order autocorrelator as shown in Fig. 2-8. The setup is based on a modified Michelson interferometer with a 50/50 beam-splitter. One of the mirrors moves back on a translation stage, while the other can be moved using a translation stage to precisely calibrate the delay τ .

The measured autocorrelation result of our Ti:sapphire laser is shown as Fig. 2-9. To determine the pulse width, the knowledge of pulse shape is required. Most commonly, we assume the pulse is Gaussian shape, and the autocorrelation width, $\Delta\tau$, is $\sqrt{2}$ times of the pulse width, Δt . With Fig. 2-9, we can figure out the full width at half maximum (FWHM) of autocorrelation is 90 fs. According to the result, the pulse width of our Ti:sapphire laser is 64 fs.

2-2 Principles of Terahertz Time-domain

Spectrometer

The picoseconds pulses of broadband THz radiation can be generated by converting the femtosecond pulses in a nonlinear crystal or a photoconductive antenna. These are known as the two main mechanisms for the generation of THz radiation: optical rectification in a nonlinear

medium [7] and photoconductive switching [8]. Following, we introduce how to generate and detect the THz wave, and the terahertz time-domain spectroscopy (THz-TDS) system.

2-2.1 Generation of terahertz wave by using photoconductive antennas

In 1988, Grischkowsky et al. demonstrated the first coherent detection of THz radiation by using the ultrashort pulse and the photoconductive antenna [9, 10]. In order to construct the photoconductive antenna, the photoconductive substrate must have some excellent properties such as short carrier lifetime, high mobility, and high breakdown voltage. The characteristics of some commonly used photoconductive substrates are shown in Table 2-1 [11]. In our THz-TDS system, low-temperature-grown GaAs (LT-GaAs) have been employed as the substrate of photoconductive antenna. The thickness of the substrate is about 400 μm . The structure of the antenna is a Hertzian dipole antenna with a 5 μm central gap, line width of 10 μm , and two conductive lines are separated 20 μm apart, made of AuGe/Ni/Au metal material as shown in Fig. 2-10 [12]. When the femtosecond optical pulse with the energy larger than the bandgap of the photoconductive material ($E_g = 1.43\text{eV}$ for LT-GaAs at room temperature) is incident to photoconductive antenna, the free electrons and holes are excited in the conduction and valence band, respectively. The carriers (electron-hole pairs) are accelerated by the bias electric field, and then decayed with a time constant depended on the carrier lifetime. It results in a pulsed photocurrent in the photoconductive antenna. Because the modulated current is in sub-picosecond regime, it emits a sub-picosecond

electromagnetic wave, as THz pulse.

By using the classical Drude model [13], the dynamic behaviors of the free carriers generated by the ultrashort pulses can be described. According to this model, the differential average velocity of the free carriers is

$$\frac{dv_c(t)}{dt} = -\frac{v_c(t)}{\delta\tau} + \frac{q}{m_c} E(t), \quad (2-3)$$

where $v_c(t)$ is the average velocity of the carrier, $\delta\tau$ is the carrier collision time, q is the charge of the carrier (an electron or a hole), m_c is the effective mass of the carrier, and $E(t)$ is the biasing electric field [14]. The photocurrent density in the emitter corresponds to the convolution of the temporal shapes of the exciting ultrashort pulses and the impulse current response of the photoconductive antenna. It can be presented as

$$j_c(t) = P_{opt}(t) \otimes [n_c(t)qv_c(t)], \quad (2-4)$$

where $j_c(t)$ is the photocurrent density, $P_{opt}(t)$ is the optical power of the ultrashort pulses, \otimes denotes the convolution product, and $n_c(t)$ is the density of the photocarriers. The current density $[n_c(t)qv_c(t)]$ represents the impulse response of the photoconductive antenna, i.e., its response to a delta Dirac optical excitation. For a Hertzian dipole, assuming the THz detector is in the far-field range and neglecting the dispersion of the quasi-optical system that focuses the THz beam, the THz field at a distance r ($r \gg \lambda$) and time t can be presented as

$$E_{THz}(t) = \frac{l_e}{4\pi\epsilon_0 c^2 r} \frac{dj_c(t)}{dt} \sin\theta \propto \frac{dj_c(t)}{dt} \quad (2-5)$$

where l_e is the effective length of the dipole antenna, and θ is the

angle from the direction of the dipole antenna; ε_0 and c are the dielectric constant and the velocity of light in vacuum, respectively. Obviously, the THz field is directly proportional to the temporal derivative of the photocurrent density. Figure 2-12 shows the calculated photocurrent in the emitting photoconductive antenna and the amplitude of the THz field versus time. The temporal pulse shape of the ultrashort pulse is shown as a dotted line [14]. The THz waves generated by this method have average power levels on the order of nanowatt. The bandwidth of the generated THz wave is primarily limited by how quickly the carriers can accelerate in LT-GaAs substrate, rather than the pulse duration of the ultrashort laser pulse.

2-2.2 Detection of terahertz wave by using photoconductive antennas

For the detecting antenna, the physical process is similar to the emitting one. On the contrary, the photogenerated free carriers are accelerated by the electric field of the THz pulse in the detecting photoconductive antenna. The average velocity of the accelerated carriers obeys to the differential equation

$$\frac{dv_d(t; \Delta t)}{dt} = -\frac{v_d(t; \Delta t)}{\delta\tau_d} + \frac{q}{m_d} E_{THz}(t + \Delta t), \quad (2-6)$$

where Δt is the time delay between the optical pulse and the THz wave onto the detector, $v_d(t; \Delta t)$ is the average velocity of the accelerated carriers. $\delta\tau_d$ and m_d are the carriers collision time and the effective mass of the accelerated carriers in the detecting antenna, respectively. $E_{THz}(t + \Delta t)$ is the electric field of the THz pulse.

The actual photocurrent density in the detecting antenna is given by the convolution product of the temporal shapes of the ultrashort pulse that triggers the detector and of the impulse response of the photoswitch to a Dirac-like optical excitation. Consequently, the instantaneous photocurrent density in the detector is presented as

$$j_d(t; \Delta t) = P_d(t) \otimes [n_d(t) q v_d(t; \Delta t)] \quad (2-7)$$

Furthermore, the measured THz signal corresponds to the average current flowing through the gap of the detecting antenna. Therefore, the measured photocurrent is given by

$$\begin{aligned} J_d(\Delta t) &\propto \int_{-\infty}^{+\infty} j_d(t; \Delta t) dt \\ &\propto \int_{-\infty}^{+\infty} dt \int_{-\infty}^{+\infty} P_d(t') \otimes [n_d(t-t') q v_d(t-t'; \Delta t + t')] dt' \end{aligned} \quad (2-8)$$

Briefly, the measured photocurrent density $J_d(\Delta t)$ is relative to the THz electric field $E_{THz}(t + \Delta t)$ and the response function of the detector. The carrier life time, the transmission characteristics of LT-GaAs, the resonance characteristics of antenna, the pulse shape, the power of the probe beam, and the diffractive effect of the THz beam determine the transient response of the THz signal. The electric field of THz generates the current across the gap of photoconductive antenna amplified using a low-bandwidth amplifier, such as Lock-in amplifier. This amplified current corresponds to the THz field. Because the carriers in the LT-GaAs substrate have an extremely short lifetime, the THz electric field is only sampled by using an extremely narrow slice, such as the femtosecond pulse.

2-2.3 Terahertz time-domain spectroscopy (THz-TDS)

Terahertz time-domain spectroscopy (THz-TDS) is a spectroscopic technique based on generating and detecting electromagnetic transients to probe material properties with the THz radiation. This method is sensitive to the sample material's effect on both the amplitude and the phase of the THz radiation.

Figure 2-12 shows a schematic of the experimental setup of the THz-TDS system. Briefly, the femtosecond pulse comes from the Ti:sapphire laser is split into pump beam and probe beam that illuminate the emitting and detecting antennas. Both of the emitter and the detector is attached on the hyper-hemispherical silicon lens to collimate the THz radiation. The emitting photoconductive dipole antenna is biased with a 1kHz-modulation square wave, and the bias voltage is 5V. The generated THz radiation is collimated and collected by a pair of off-axis parabolic gold mirrors. The transient current was induced in the gap of the detecting antenna with the focused THz electric field, which accelerated the photocurrents excited by the probing ultrashort pulse. A digital lock-in amplifier with a current-voltage preamplifier module (Model SR830, Stanford Research System) is connected to the electrodes of the detecting antenna, to synchronously detect the photoconductive current. Because the detecting electronics are much slower than the THz signals, it is difficult to measure the whole THz transients directly. By scanning the pulse delay of the emitting beam with respect to the detecting beam, the THz signal can be acquired sequentially. The data acquisition and the control of the stepping stage for the delay are conducted with a LabVIEW program using the GPIB interface. The time dependent electric transient through the gap of the antenna depends on both the magnitude and the direction of THz wave.

The experimental data of THz signal in time domain through air is shown as Fig. 2-13. The red and black line is the signal in air with and without N₂ purged, respectively. After the main signal (~25 ps), the signal fluctuation is shown in the signal without N₂ purged (black line). This fluctuation came from the water vapor absorption from the moist atmosphere of which the relative humidity (R.H.) is about 50%. On the other hand, the signal in the atmosphere with N₂ purged (red line) is much smoother because of the dry air condition (R.H. ~ 3 %). By applying Fast Fourier Transform (FFT) to both of the THz time domain signal, the power spectrum in frequency domain is obtained as shown in Figure 2-14. It shows several water vapor absorption peaks below 1.5 THz [15]. The reliable THz signal is from 0.2 to 3.5 THz. The signal and noise ratio is around 10⁷:1.



2-3 Principles of NLC alignment and deformation

For NLC applications, uniformly align the NLC molecules is the most fundamental and essential subject. There are many surface treatments for NLC alignment, such as rubbing alignment method, photoalignment method, ion beam bombardment method, and chemical treatment method [16-19]. In our work, we use the most commonly surface alignment methods: rubbing alignment method, and chemical treatment method, for homogeneous and homeotropic alignment, respectively.

2-3.1 Rubbing alignment method and chemical alignment

method

As mentioned in Chapter 1, the orientation of NLC molecules can be easily aligned by the surface. For surface alignment treatment, the substrate is coated with an alignment layer. The major mechanisms of surface alignment are the micro-morphology of the alignment surface and the interaction force between the LC molecules and the alignment molecules. With this concept, we can align the NLC molecules before applying field.

Homogeneous alignment mentions that all NLC molecules in the cell are parallel aligned to both substrates and the directors have the same orientation as shown in Fig. 2-15(a). The rubbing alignment method is the most commonly method to obtain the achievement. In our experiment, basically, we utilize the fused silica as substrates for sample fabrication. The substrates are cleaned with synthetic detergent, acetone, methanol, and DI water. For rubbing alignment, the substrates are coated with polyimide (PI), Nissan SE-130B. The PI is soft baked at 80°C for 5 min, and hard baked at 180°C for 60 min, respectively. The rubbing machine includes a cotton velvet covered roller, and a movable substrate holding stage. The rotation speed of the roller is 900 rpm and the roller contacts the substrate to apply pressure on it. The holding stage moves forward with a constant speed. We can repeat this process to enhance the rubbing alignment strength [20].

Homeotropic alignment mentions that all NLC molecules in the cell

are perpendicular aligned to both substrates and the directors have the same orientation as shown in Fig. 2-15(b). To obtain the homeotropic alignment in our work, we use the surfactant, N, N-dimehtyl-N-octadecyl-3-amino-propyl-trimeth oxysilyl chloride (DMOAP), which is coated on cleaned substrate. The molecular interaction force will lead the injected NLC molecules to align perpendicular to the substrate surface.

2-3.2 Deformation and operation principle of NLC molecules

There are three basic types of elastic energy, splay, twist, and bend, to describe the deformations of NLC under external stress [21, 22] as shown in Fig. 2-16. The elastic energy density of a deformed NLC can be written as,

$$f_d = \frac{1}{2}k_1(\nabla \cdot \mathbf{n})^2 + \frac{1}{2}k_2(\mathbf{n} \cdot \nabla \times \mathbf{n})^2 + \frac{1}{2}k_3(\mathbf{n} \times \nabla \times \mathbf{n})^2, \quad (2-9)$$

where k_1 , k_2 , and k_3 are the splay, twist, and bend elastic constants, respectively.

When we apply an external electric or magnetic field, the total free energy F can be written as,

$$F = \int (f_d + f_{E/M}) d\rho, \quad (2-10)$$

where the $f_{E/M}$ is the induced energy density of the external field, and ρ is the unit volume. The elastic constants of NLC determine the restoring torques that arise when the system is perturbed from its equilibrium configuration. These restoring torques are usually very weak. Therefore,

an external electric or magnetic is often applied to cause a reorientation of the molecules. According to Eq. 2-10, there will be a phase transition, at a certain critical value of the external field (E_c , H_c), between the unperturbed conformation and the distorted conformation. The critical value of the electric field or magnetic field can be written as,

$$E_c = \frac{\pi}{d} \sqrt{\frac{k}{\Delta\epsilon\epsilon_0}}, \text{ and} \quad (2-11. a)$$

$$H_c = \frac{\pi}{d} \sqrt{\frac{k}{\Delta\chi}}, \quad (2-11. b)$$

where k is the elastic constant, d is the distance of the boundaries, ϵ_0 is the dielectric constant in the vacuum, and $\Delta\epsilon$ and $\Delta\chi$ are dielectric constant anisotropy and magnetic susceptibility anisotropy, respectively.

In this work, we use two types of NLC, E7 and MDA-00-3461, which are positive dielectric constant anisotropy and magnetic susceptibility anisotropy. The NLC molecules are tend to align parallel to the external electric or magnetic field.

Tables

Table 2-1 Characteristics of photoconductive substrates

Photoconductive materials	Carrier lifetime (ps)	Mobility ($\text{cm}^2/(\text{V} \cdot \text{s})$)	Resistivity ($\Omega \cdot \text{cm}$) (Breakdown field, V/cm)	Band gap (eV at R.T.)
Cr:doped SI-GaAs	50–100.0	≈ 1000	10^7	1.43
LT-GaAs	0.3	150– 200	10^6 (5×10^5)	1.43
SI-InP	50–100.0	≈ 1000	4×10^7	1.34
Ion-Implanted InP	2– 4.0	200	$> 10^6$	1.34
RD-SOS	0.6	30		1.10
Amorphous Si	0.8– 20.0	1	10^7	1.10
MOCVD CdTe	0.5	180		1.49
LT-In _{0.52} Al _{0.48} As	0.4	5		1.45
Ion-implanted Ge	0.6	100		0.66



Reference

- [1] P. F. Moulton, "Spectroscopic and laser characteristics of Ti:Al₂O₃," *J. Opt. Soc. Am. B*, 3, 125, 1986.
- [2] Robert W. Boyd, "Nonlinear Optics," 3rd ed., New York USA, Academic press.
- [3] Miguel A. Larotonda, "Saturation of Kerr-lens mode locking and the self-amplitude modulation coefficient," *Optics Communications*, 228, 381, 2003.
- [4] P. Lacovara, L. Esterowitz, and M. Kokta, "Growth, Spectroscopy, and Lasing of Titanium-Doped Sapphire," *IEEE J. Quantum Electronics*, QE-21, 1614, 1985.
- [5] D. E. Spence, P. N. Kean, and W. Sibbett, "60-fsec pulse generation from a self-mode-locked Ti:sapphire laser," *Opt. Lett.*, 16, 42, 1991.
- [6] Claude Rullière (Ed.), "Femtosecond Laser Pulses," Springer.
- [7] B. Greene, P. Sateta, D. Dykaar, S. Schmitt-Rink, and S. L. Chuang, "Far-infrared light generation at semiconductor surface and its spectroscopic applications," *IEEE J. Quantum Electron*, 28, 2302, 1992.
- [8] X.-C. Zhang, "Generation and detection of terahertz electromagnetic pulses from semiconductors with femtosecond optics," *J. Luminescence*, 66&67, 488, 1996.
- [9] Ch. Fattinger, D. Grischkowsky, "Point source terahertz optics," *Appl. Phys. Lett.*, 53, 1480, 1988.
- [10] M. van Exter, D. Grischkowsky, "Characterization of an optoelectronic terahertz beam system," *IEEE Trans. Microwave Theory*

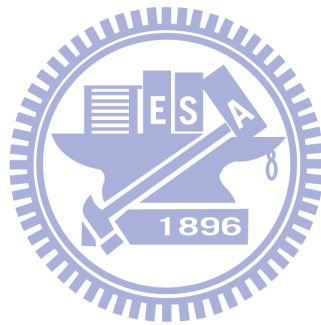
Tech., 38, 1684, 1990.

- [11] K. Sakai (Ed.), “*Terahertz Optoelectronics*,” Springer, 2004.
- [12] D. H. Auston, K. P. Cheung, and P. R. Smith, “Picosecond photoconducting Hertzian dipoles,” *Appl. Phys. Lett.*, 45, 284, 1984.
- [13] D. Grischkowsky, S. Keiding, M. van Exter, and Ch. Fattinger, “Far-infrared time-domain spectroscopy with terahertz beams of dielectrics and semiconductors,” *J. Opt. Soc. Am. B*, 7, 2006, 1990.
- [14] L. Duvillaret, F. Garet, J.-F. Roux, and J.-L. Coutaz, “Analytical modeling and optimization of terahertz time-domain spectroscopy experiments, using photoswitches as antennas,” *IEEE Journal on Selected Topics in Quantum Electronics*, 7, 615, 2001.
- [15] M. van Exter, Ch. Fattinger, and D. Grischkowsky, “Terahertz time-domain spectroscopy of water vapor,” *Optics Letters*, 14, 1128, 1989.
- [16] T. Uchida, M. Hirano, and H. Sakai, “Director orientation of a ferroelectric liquid crystal on substrates with rubbing treatment: The effect of surface anchoring strength,” *Liquid Crystals*, 5, 1127, 1989.
- [17] W. M. Gibbons, P. J. Shannon, S. T. Sun, and B. J. Swetlin, “Surface-mediated alignment of nematic liquid crystals with polarized laser light,” *Nature*, 351, 49, 1991.
- [18] P. Chaudhari, J. Lacey et al., “Atomic-beam alignment of inorganic materials for liquid-crystal displays,” *Nature*, 411, 56, 2001.
- [19] F. J. Kahn, “Orientation of liquid crystals by surface coupling agents,” *Appl. Phys. Lett.*, 22, 386, 1973.
- [20] N. A. J. M. van Aerle, M. Barmantlo, and R. W. J. Hollering, “Effect

of rubbing on the molecular orientation within polyimide orienting layers of liquid –crystal displays,” J. Appl. Phys., 74, 3111, 1993.

[21] Pochi Yeh, and Claire Gu, “Optics of Liquid Crystal Displays,” A Weiley Interscience Publication, John Wiley & Sons, Inc.

[22] P. G. De Gennes, and J. Prost, “The Physics of Liquid Crystals,” second edition, Clarendon Press, Oxford, 1993.



Figures

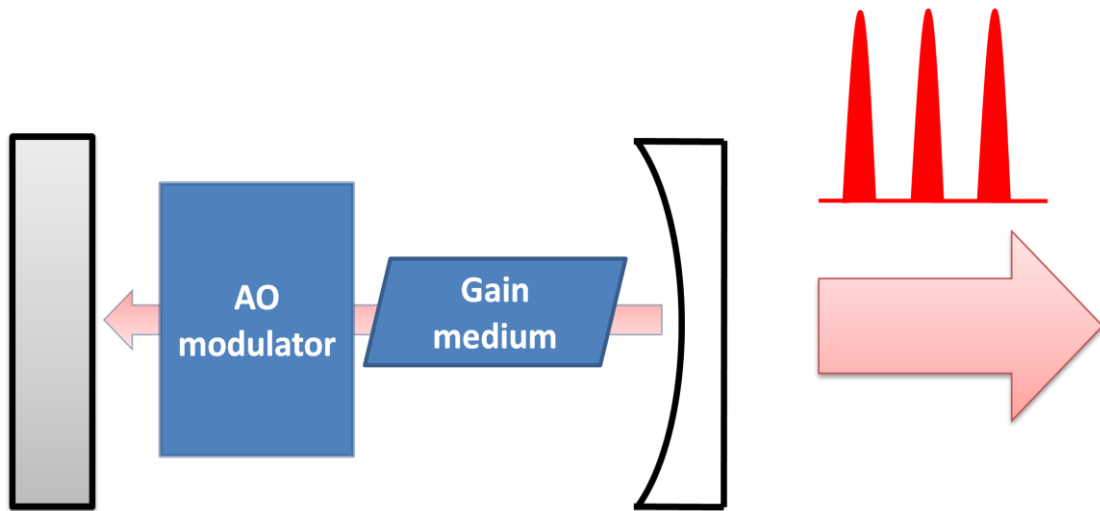


Figure 2-1 Active mode-locking method with AO modulator

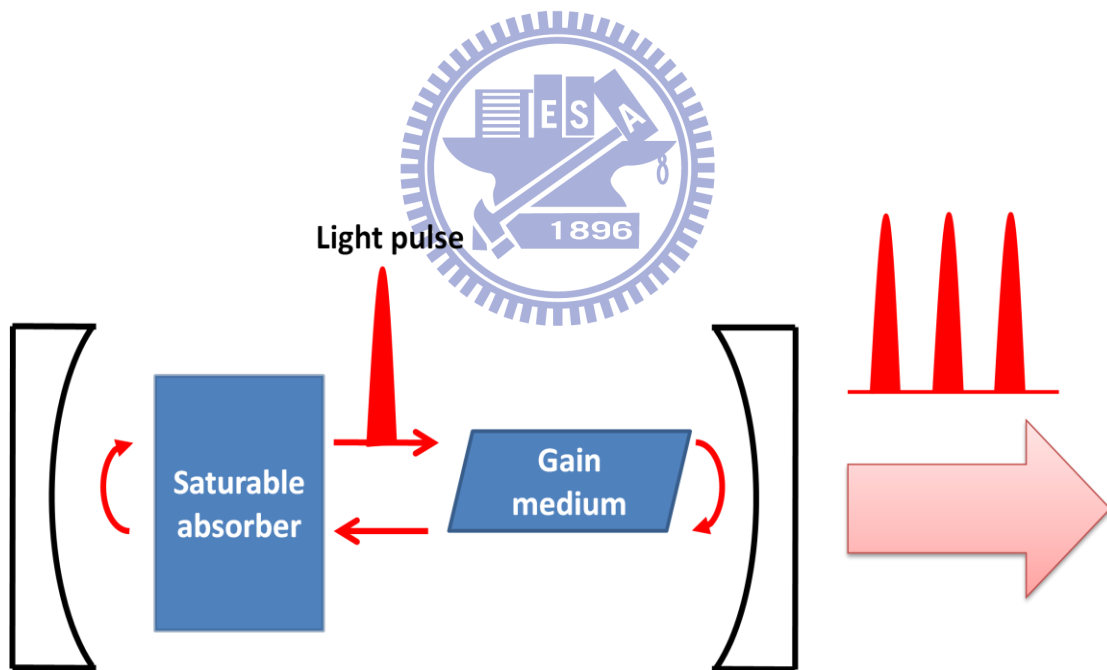


Figure 2-2 Passive mode-locking method with saturable absorber

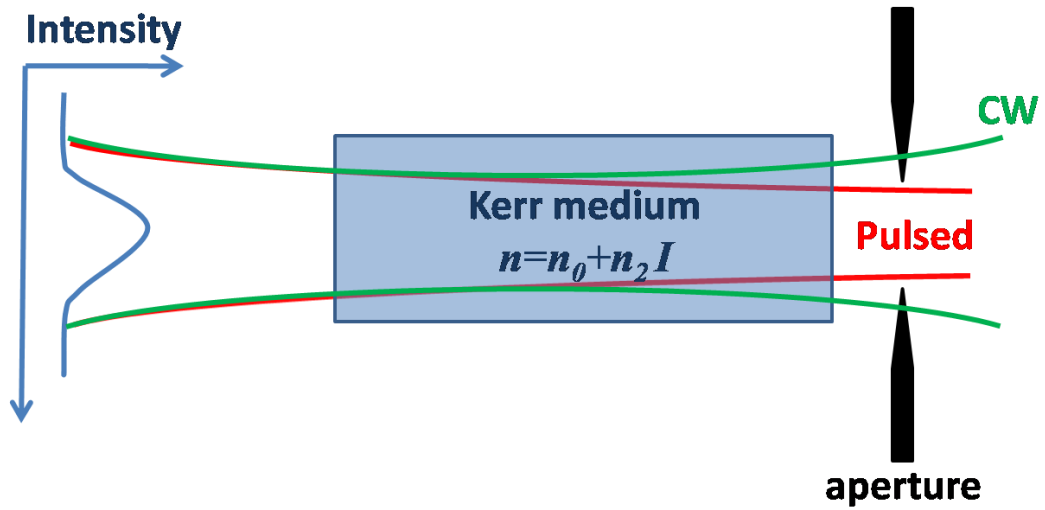


Figure 2-3 Kerr-lens mode-locking method with hard aperture

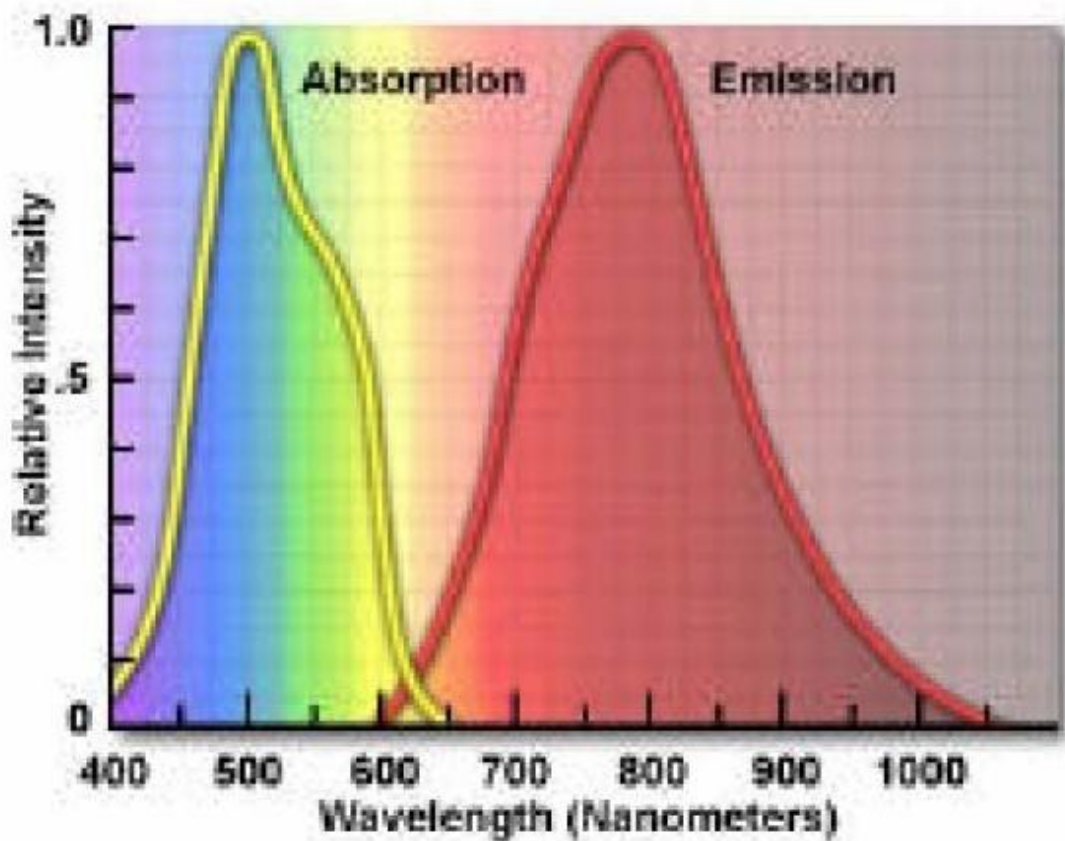


Figure 2-4 Absorption and emission spectra of Ti:sapphire

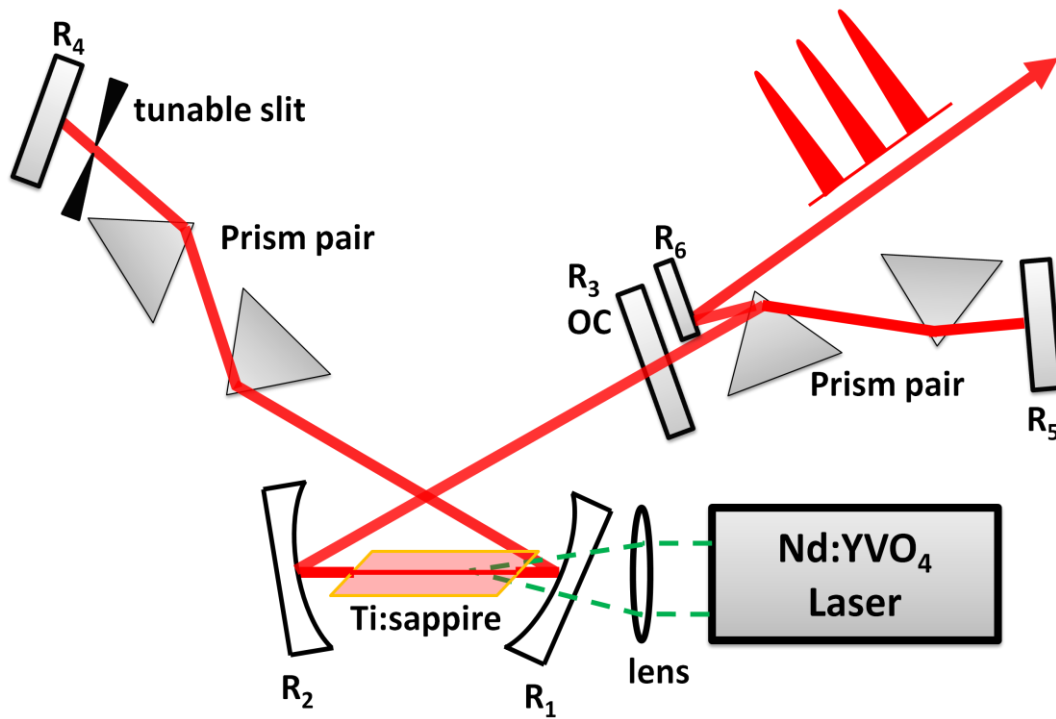


Figure 2-5 Construction of Ti:sapphire pulsed femtosecond laser. R: reflective mirror, OC: output coupler.

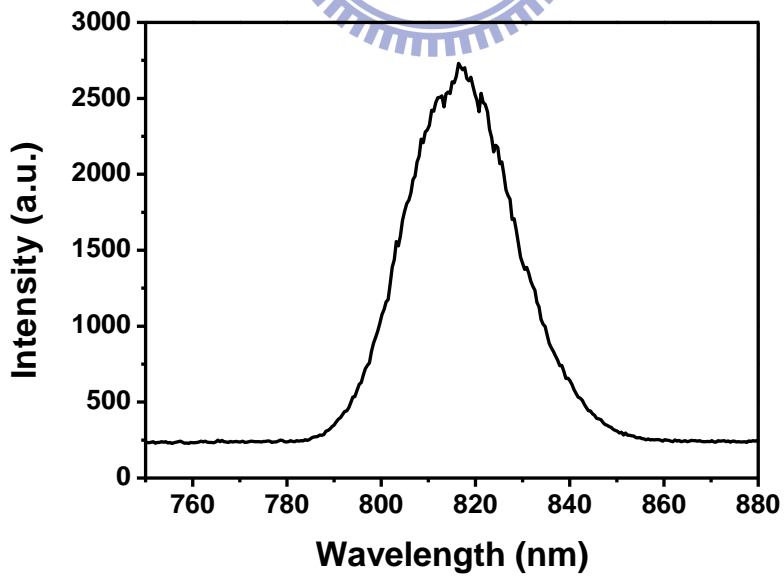


Figure 2-6 Spectrum of mode-locked pulse

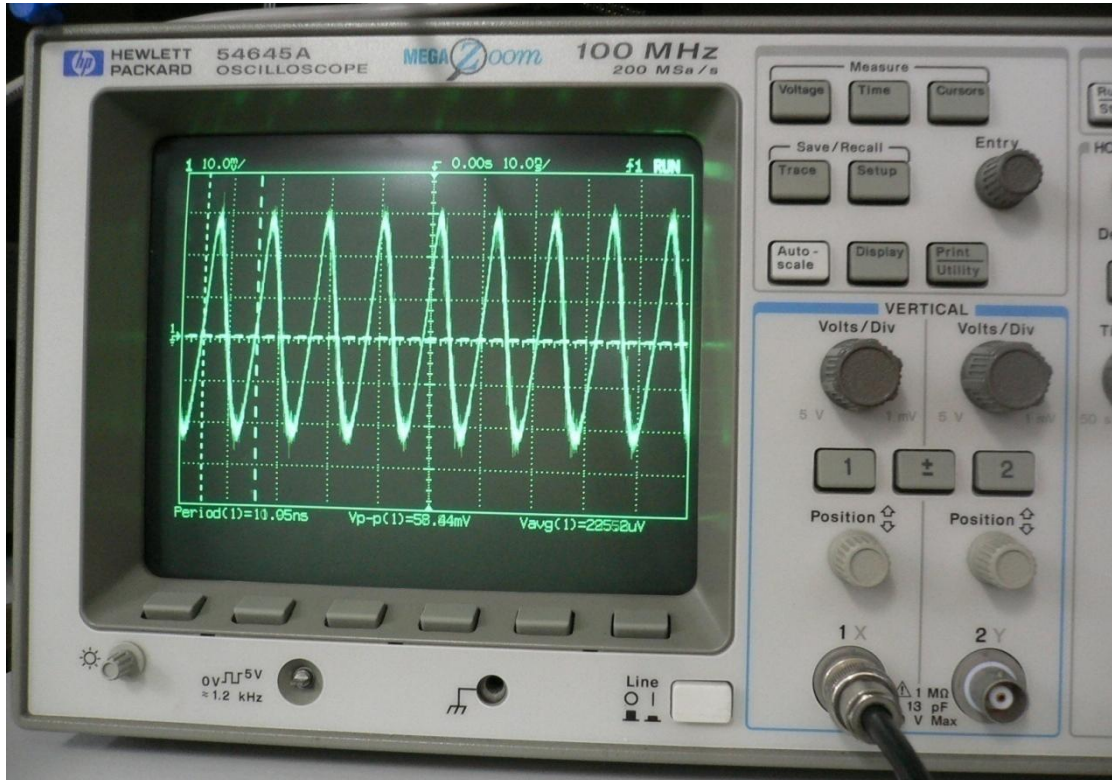


Figure 2-7 Pulse train of Ti:sapphire pulsed femtosecond laser. Repetition rate is about 90 MHz



Autocorrelator

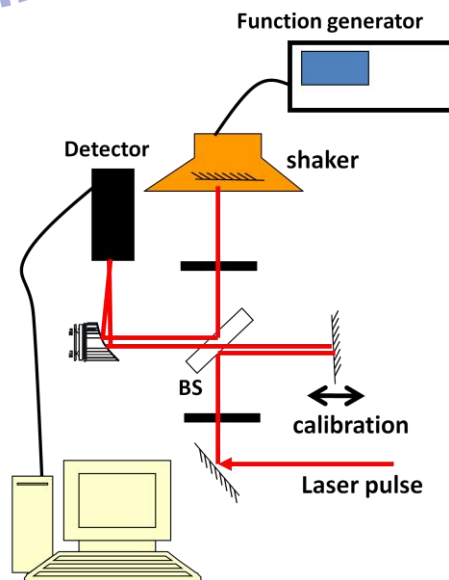
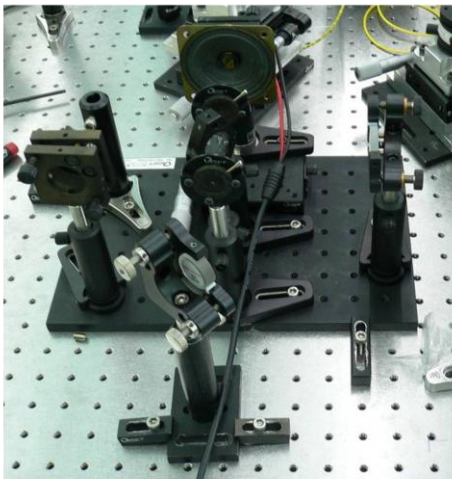


Figure 2-8 Photograph and schematic diagram of interferometric autocorrelator

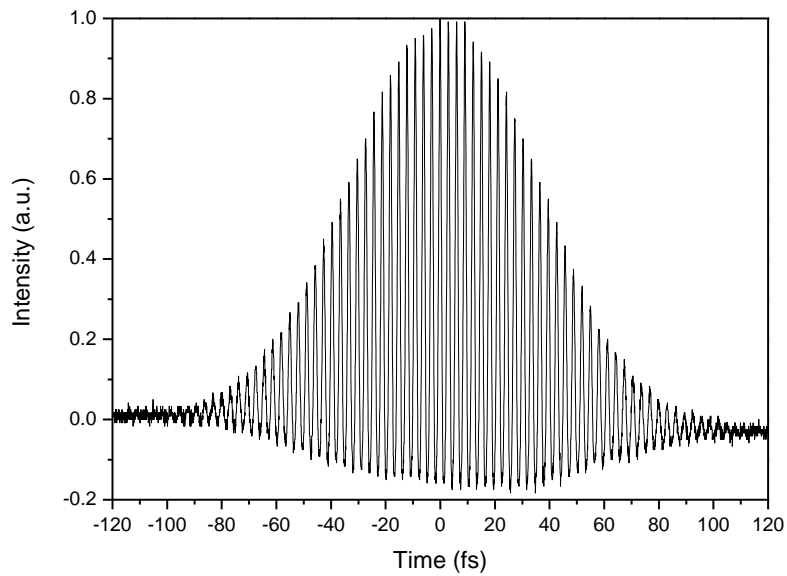


Figure 2-9 Autocorrelation signal of Ti:sapphire pulsed femtosecond laser. Autocorrelation signal has 90 fs in FWHM, which corresponds to 64 fs pulse width

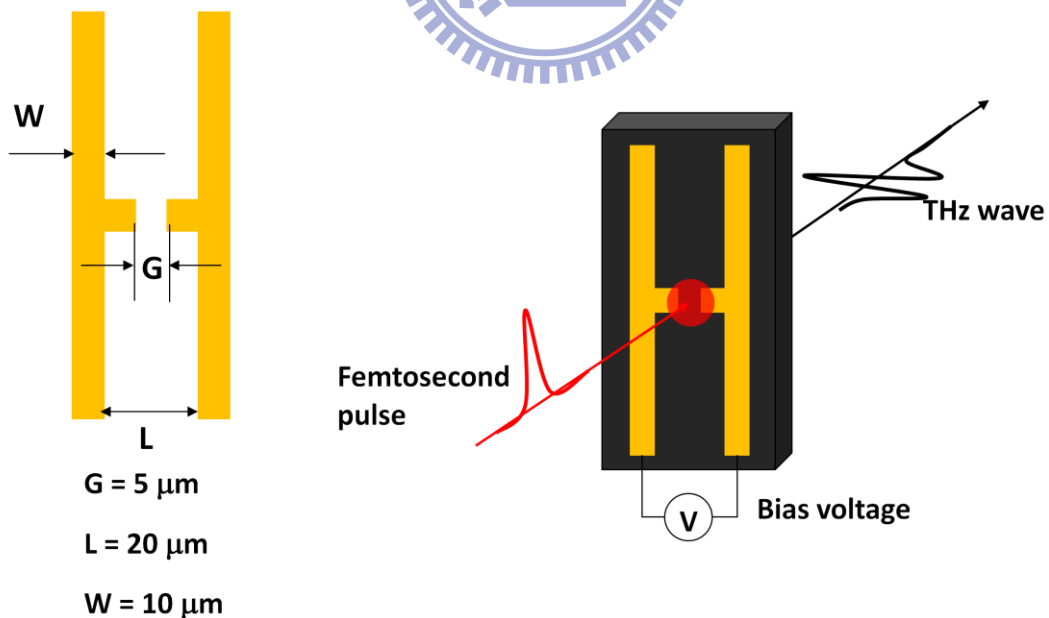
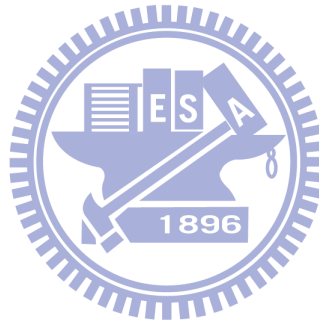


Figure 2-10 Photoconductive antenna (Hertzian dipole antenna). Dimensions of pattern are shown.

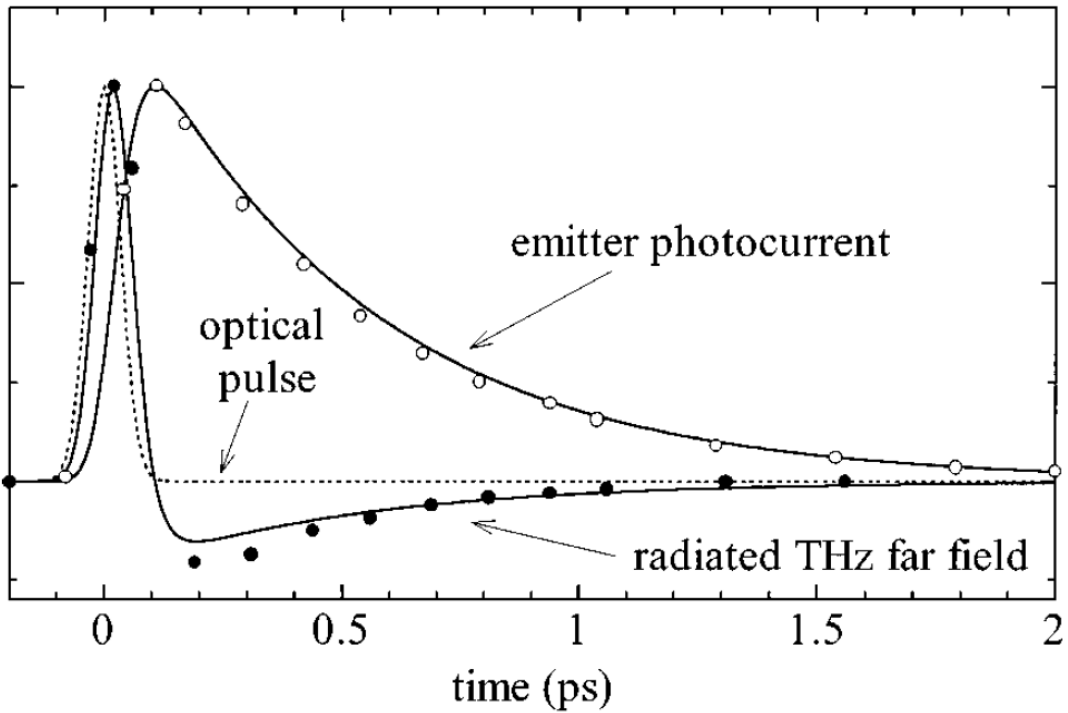


Figure 2-11 Calculated photocurrent in emitting photoconductive antenna and amplitude of THz field versus time. Temporal pulse shape of ultrashort pulse is shown as a dotted line.

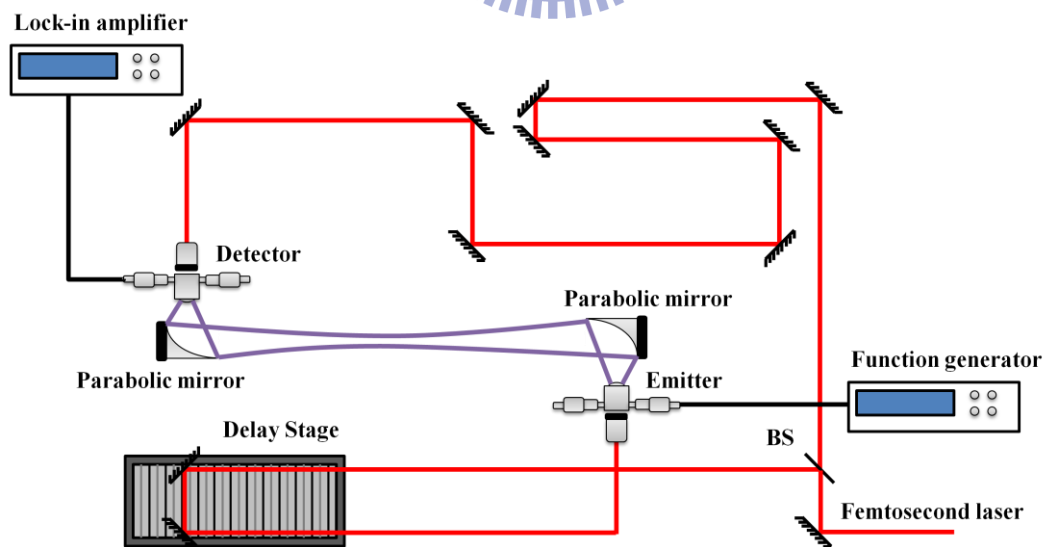


Figure 2-12 Schematic diagram of THz-TDS

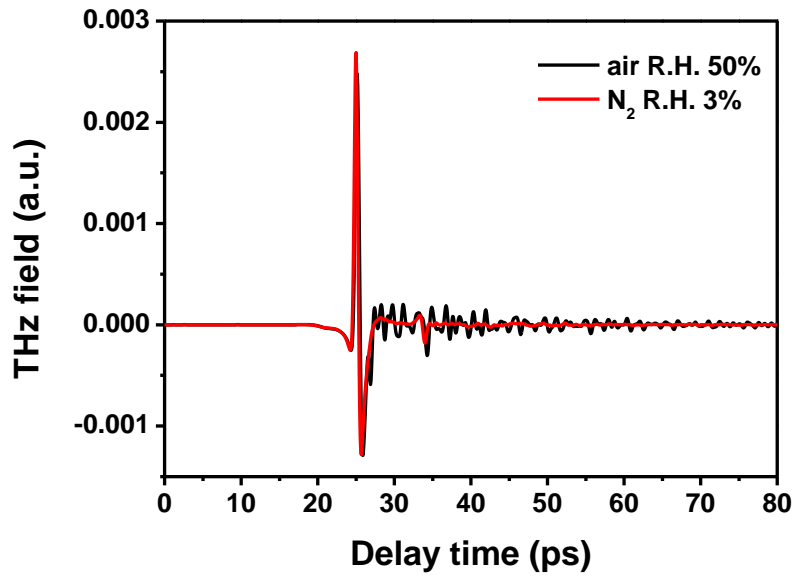


Figure 2-13 Time domain THz signal measured by THz-TDS. Non-purged (R.H. 50%) and N₂ purged (R.H. 3%) are shown as black and red lines, respectively.

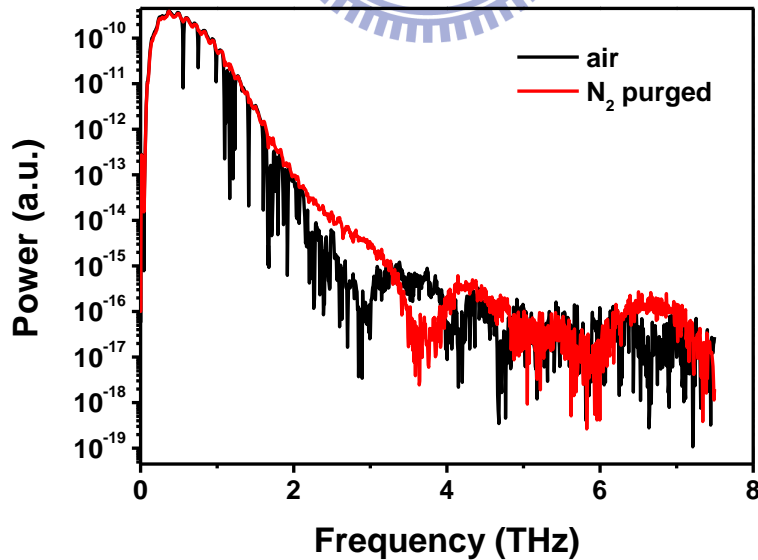
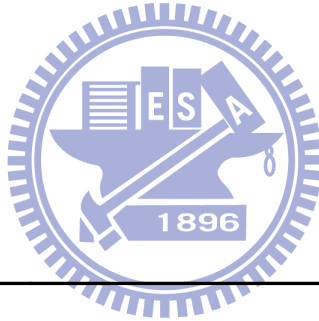
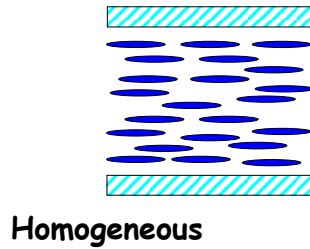
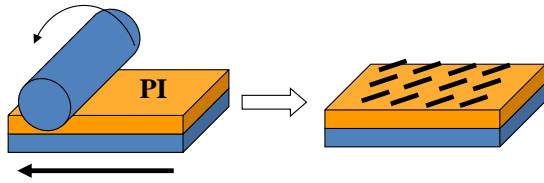


Figure 2-14 Power spectra of THz signal in frequency domain. Non-purged (R.H. 50%) and N₂ purged (R.H. 3%) are shown as black and red lines, respectively.

• Rubbing process

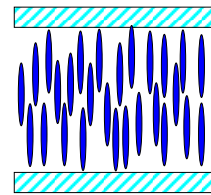
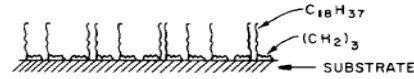
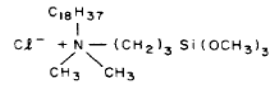


Homogeneous

(a)

• Coated with surfactant

N,N-dimethyl-N-octadecyl-3-aminopropyltrimethoxysilyl chloride (DMOAP)



Homeotropic

(b)

Figure 2-15 Surface alignment treatments: (a) rubbing method for homogeneous alignment, and (b) chemical treatment method for homeotropic alignment

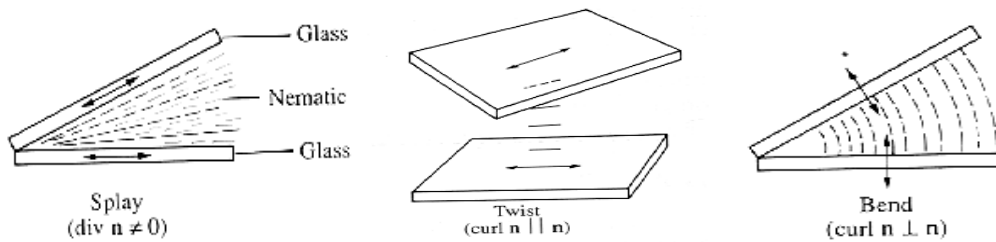


Figure 2-16 Three different types of deformation occurring in NLC cell

Chapter 3 Optical Constants of Nematic Liquid

Crystal in Terahertz Range

The tunable devices based on NLC have been widely utilized in the visible region. It is the NLC has the characteristics of large birefringence and low absorption in the visible [1, 2] that NLC is the suitable material for the tunable device. For tunable devices design in the THz range, we should have the knowledge of optical constants of NLC and the fused silica substrate. In this chapter, we will introduce how we use the THz-TDS to characterize the optical constants and the analysis theory. In this thesis, we use NLC E7, MDA-00-3461 (from Merck) for devices design. Table 3-1 is the data sheet from Merck Company to show the properties of NLC E7 and MDA-00-3461 basically in visible. We will show the optical constants of NLC E7, MDA-00-3461, and the fused silica substrates in the THz range.

3-1 Experimental procedure

The fundamental concept of complex refractive index measurement with THz-TDS is shown schematically in Fig 3-1 [4]. As mentioned in chapter 2, we can obtain the amplitude and the phase information of THz signal with THz-TDS. Therefore, comparing the phase delay and amplitude attenuation of the signal through material and with that through air, we can obtain the complex refractive index. In fact, the condition is

more complicate to evaluate the complex refractive index, and we will discuss in detail later.

Two types of cells, a reference cell and a homogeneously aligned liquid crystal cell were prepared. The reference cell was constructed by two fused silica windows coated with PI and with nominal thickness of 3.0 mm each and in contact to each other. For the liquid crystal cell, NLC E7 layer was sandwiched between two fused silica windows as substrates (the thickness of fused silica is 3.17 mm). Thickness of the liquid crystal layer was controlled with Teflon spacers and measured by subtracting the substrates thicknesses from the total cell thickness. The LC layer thickness in this work is $688 \pm 3 \mu\text{m}$. For MDA-00-3461 cell, the dimension of which was $660 \pm 3 \mu\text{m}$ in thickness.

The test cell was placed in the THz-TDS and the THz beam was collimated at the sample position [3]. The THz fields of e-wave and o-wave are parallel and perpendicular to the aligned direction of LC cell, respectively. We usually confine spot size of THz beam as 0.8 cm by using an aperture to make sure all THz signal pass through LCs layer only. The THz-TDS was purged with nitrogen and maintained at a relative humidity of $3.5 \pm 0.5\%$ for optical constants measurement.

3-2 Optical constants determination

We assume that the THz signal is a plane wave passing through the cell at normal incidence. Figure 3-2 (a) is shown the schematic of the pathway of THz wave through the liquid crystal cell with two substrates.

The electric field of the THz wave can be presented as

$$E_{LC}(t) = \int_{-\infty}^{+\infty} E_0(f) \tilde{t}_{AW} e^{i2\pi f \left(\frac{\tilde{n}_W d_{W1}}{c}\right)} \tilde{t}_{WS} FP_{LC}(f, d_S) e^{i2\pi f \left(\frac{\tilde{n}_S d_S}{c}\right)} \tilde{t}_{SW} e^{i2\pi f \left(\frac{\tilde{n}_W d_{W2}}{c}\right)} \tilde{t}_{WA} e^{-i2\pi f t} df, \quad (3-1)$$

where $E_0(f)$ is the electric field of the incident THz wave. d_{W1} and d_{W2} are the thickness of the first and second sample substrate, respectively, and d_S is the thickness of the liquid crystal layer.

$\tilde{n}_W = n_W + i\kappa_W$ and $\tilde{n}_S = n_S + i\kappa_S$, are the complex refractive index of window and thin film, respectively. \tilde{t}_{AW} , \tilde{t}_{WS} , \tilde{t}_{SW} and \tilde{t}_{WA} are the Fresnel transmission coefficient at the air-window, window-liquid crystal, liquid crystal- window and window-air interfaces, respectively. These four complex transmission coefficient are presented as

$$\tilde{t}_{AW} = \frac{2 \times \tilde{n}_A}{\tilde{n}_A + \tilde{n}_W}, \quad \tilde{t}_{WS} = \frac{2 \times \tilde{n}_W}{\tilde{n}_W + \tilde{n}_S}, \quad \tilde{t}_{SW} = \frac{2 \times \tilde{n}_S}{\tilde{n}_S + \tilde{n}_W} \quad \text{and} \quad \tilde{t}_{WA} = \frac{2 \times \tilde{n}_W}{\tilde{n}_W + \tilde{n}_A}. \quad (3-2)$$

where \tilde{r}_{SW} is the Fresnel reflection coefficient of the liquid crystal-window interface. This complex reflective coefficient is presented as

$$\tilde{r}_{SW} = \frac{\tilde{n}_S - \tilde{n}_W}{\tilde{n}_S + \tilde{n}_W}. \quad (3-3)$$

The Fabry-Perot coefficient in the liquid crystal layer with a thickness of d_S is $FP_{LC}(f, d_S)$, presented as

$$\sum_{m=0}^N \left[\tilde{r}_{SW}^{2m} e^{i2\pi f \left(\frac{\tilde{n}_S d_S \times 2m}{c}\right)} \right]. \quad (3-4)$$

According to Figure 3-2 (b), the electric field of the THz wave transmitted through only substrates at a frequency f can be obtained as

$$E_{ref}(t) = \int_{-\infty}^{+\infty} E_0(f) \tilde{t}_{AW} e^{i2\pi f \left(\frac{\tilde{n}_W d_{W3}}{c}\right)} e^{i2\pi f \left(\frac{\tilde{n}_W d_{W4}}{c}\right)} \tilde{t}_{WA} e^{i2\pi f \left(\frac{\tilde{n}_A (d_S + \Delta d)}{c}\right)} e^{-i2\pi f t} df, \quad (3-5)$$

where d_{W3} and d_{W4} are the thickness of the two reference substrate, and $\tilde{n}_W = n_W + i\kappa_W$ is the complex refractive index of air. The complex transmission coefficients \tilde{t}_{AW} and \tilde{t}_{WA} , which indicate the complex amplitude transmittance at the air-window and window-air interfaces, respectively, are presented as

$$\tilde{t}_{AW} = \frac{2 \times \tilde{n}_A}{\tilde{n}_A + \tilde{n}_W}, \text{ and } \tilde{t}_{WA} = \frac{2 \times \tilde{n}_W}{\tilde{n}_W + \tilde{n}_A}. \quad (3-6)$$

Let $d_W = d_{W1} + d_{W2}$ and $d'_W = d_{W3} + d_{W4}$. In order to compare two THz signal with each other, the total optical path of these two cases need to be equal.

$$d_W + d_S = d'_W + d_S + \Delta d$$

$$\Delta d = d_W - d'_W$$

(3-7)

Here, Δd is the total differential thickness between sample substrate and reference substrate.

The complex transmittance of the sample is presented using Equation (3-1) and (3-5) as,

$$\begin{aligned} \sqrt{T_{LC}} e^{i(\phi_{LC})} &= \frac{E_{LC}(t)}{E_{ref}(t)} \\ &= \tilde{t}_{WS} \tilde{t}_{SW} FP_{LC}(f, d_S) e^{i \frac{2\pi f}{c} (\tilde{n}_W (d_{W1} + d_{W2}) + \tilde{n}_S d_S - \tilde{n}_W (d_{W3} + d_{W4}) - \tilde{n}_A (d_S + \Delta d))} \\ &= \tilde{t}_{WS} \tilde{t}_{SW} FP_{LC}(f, d_S) e^{i \frac{2\pi f}{c} (\tilde{n}_W d_W + \tilde{n}_S d_S - \tilde{n}_W d'_W - \tilde{n}_A (d_S + \Delta d))} \\ &= \tilde{t}_{WS} \tilde{t}_{SW} FP_{LC}(f, d_S) e^{i \frac{2\pi f}{c} (\tilde{n}_W \Delta d + \tilde{n}_S d_S - \tilde{n}_A d_S - \tilde{n}_A \Delta d)} \\ &= \left[\tilde{t}_{WS} \tilde{t}_{SW} FP_{LC}(f, d_S) e^{-\frac{2\pi f}{c} [(\kappa_S - \kappa_A) d_S + (\kappa_W - \kappa_A) \Delta d]} \right] \\ &\quad \times e^{i \frac{2\pi f}{c} [(n_S - n_A) d_S + (n_W - n_A) \Delta d]} \end{aligned} \quad (3-8)$$

where $\sqrt{T_{LC}}$ and ϕ_{LC} indicate the power transmittance and the phase shift, respectively. According to complex number calculation, we can convert the right part of Equation (3-8) into a point in the complex plane. The radius and angle of this point are presented as the power transmittance and phase shift, respectively.

$$e^{i(\phi_{LC})} = e^{i \arg \left(\tilde{t}_{WS} \tilde{t}_{SW} \sum_{m=0}^N \left[\tilde{r}_{SW}^{2m} e^{i 2\pi f \left(\frac{\tilde{n}_S d_S}{c} \times 2m \right)} \right] \right)} e^{i \frac{2\pi f}{c} [(n_S - n_A) d_S + (n_W - n_A) \Delta d]}$$

$$\sqrt{T_{LC}} = \left| \tilde{t}_{WS} \tilde{t}_{SW} \sum_{m=0}^N \left[\tilde{r}_{SW}^{2m} e^{i 2\pi f \left(\frac{\tilde{n}_S d_S}{c} \times 2m \right)} \right] \right| \times e^{\frac{-2\pi f}{c} [(\kappa_S - \kappa_A) d_S + (\kappa_W - \kappa_A) \Delta d]}$$
(3-9)

From Equation (3-9) the complex refractive index $\tilde{n}_S = n_S + i\kappa_S$ is derived as follows,

$$n_S = \frac{1}{2\pi f \frac{d_S}{c}} \left[(\phi_{LC}) - \arg \left(\tilde{t}_{WS} \tilde{t}_{SW} \sum_{m=0}^N \left[\tilde{r}_{SW}^{2m} e^{i 2\pi f \left(\frac{\tilde{n}_S d_S}{c} \right)} \right]^{2m} \right) \right] + n_A - \frac{(n_W - n_A) \Delta d}{d_S}$$

$$\kappa_S = \frac{1}{-2\pi f \frac{d_S}{c}} \ln \left[\frac{\sqrt{T_{LC}}}{\tilde{t}_{WS} \tilde{t}_{SW} \sum_{m=0}^N \left[\tilde{r}_{SW}^{2m} e^{i 2\pi f \left(\frac{\tilde{n}_S d_S}{c} \right)} \right]^{2m}} + \kappa_A + \frac{(\kappa_W - \kappa_A) \Delta d}{d_S} \right]$$
(3-10)

Most of the THz-TDS system is operated in the atmosphere at room temperature. The complex refractive index of air $\tilde{n}_A = 1$ is assumed. Because of the N₂ purged, the absorption coefficient $\tilde{\kappa}_A = 0$ is also assumed.

3-3 Results and discussions

3-3.1 Optical constants of fused silica substrates

In this work, two dimensions of thickness, nominal 1.0mm and 3.0mm, of fused silica were utilized to design devices or to fabricate the NLC cells for optical constants measurement. In order to understand the properties of fused silica, the optical constants of the fused silica are characterized by THz-TDS system. Figure 3-3 shows the optical constants of nominal 1.0mm fused silica substrate (measured value, $d = 1.034$ mm) in THz region. There is small ripple observed in the data. It is the Fabry-Perot effect that causes the fluctuation. For the thin fused silica, the reflection signal is close to the main signal. Therefore, it is difficult to cut off the reflection signal that the reflection signal affected the measured results. The refractive index and extinction coefficient of the 1.0mm-thick fused silica in the range from 0.2 to 2.0 THz are, $n = 1.950$ and $\kappa < 0.01$, respectively.

In order to cancel the Fabry-Perot effect, the optical constants are measured by using the thicker substrate. Figure 3-4 shows the optical constants of nominal 3.0mm fused silica substrate (measured value, $d = 3.175$ mm). The refractive index and the extinction coefficient of the 3.0mm-thick fused silica between 0.2 THz and 2.0 THz are, $n = 1.955$ and $\kappa < 0.01$. According to the spectrum of fused silica substrate, there is no any obvious absorption peak and the refractive index is constant between 0.2 THz and 2.0 THz. It shows fused silica is a good candidate for substrate in the THz experiment.

3-3.2 Optical constants of NLC E7

The NLC E7 is a mixture and has a large temperature range in nematic phase, from -10°C to 61°C . This characteristic makes NLC E7 a good material for practical applications [5-7]. We prepared a test cell which was well aligned with rubbing treatment. Figure 3-6 shows the photos of the test cell between a pair of crossed polarizers. The notation R represents the easy direction of the NLC E7, and it can be observed the brightness of the sample is uniform and the contrast is good.

The experimental method is mentioned as chapter 3-1, and we did the measurements at room temperature 24.5°C . Figure 3-7 shows the complex refractive index of NLC E7 for o-wave and e-wave as red lines and black lines, respectively. The refractive indices of NLC E7 in the THz range from 0.2 THz to 2.5 THz for o-wave and e-wave are $n_o=1.58$ and $n_e=1.71$, respectively. As expected, the strong polarizability of the NLC in direction of the long molecular axis leads to a positive anisotropy (i.e. $n_e>n_o$). The birefringence of NLC E7 is 0.13 in the THz range. The extinction coefficients of NLC E7 in this range for o-wave and e-wave are $\kappa_o=0.03$ and $\kappa_e=0.01$, respectively. The ordinary absorption is higher than the extraordinary absorption as THz waves oriented along the ordinary direction excite a broad torsional vibration mode located around 5 THz [8]. There is no sharp resonance in 0.2 – 2.5 THz. Thus NLC E7 exhibits large birefringence, small losses and broad temperature range, which are suitable for applications in THz range.

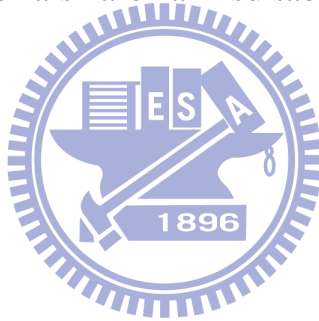
3-3.3 Optical constants of NLC MDA-00-3461

NLC MDA-00-3461 is a new material for Merck Company to replace the commercially used NLC E7. It has large temperature range (up to 90°C) in nematic phase. We prepared a test cell the same process with NLC E7 cell. Figure 3-8 shows the photos of the test cell between a pair of crossed polarizers. The notation R represents the easy direction of the NLC MDA-00-3461, and it can be observed the brightness of the sample is uniform and the contrast is good.

Figure 3-7 shows the complex refractive index of NLC MDA-00-3461 for o-wave and e-wave as red lines and black lines, respectively. The refractive indices of NLC MDA-00-3461 in the THz range from 0.2 THz to 2.0 THz for o-wave and e-wave are $n_o=1.54$ and $n_e=1.72$, respectively, in the room temperature 24.5°C. NLC MDA-00-3461 also has a positive anisotropy. The birefringence of NLC MDA-00-3461 is 0.18 in the THz range, which is larger than that of NLC E7. The extinction coefficients of NLC MDA-00-3461 in this range for o-wave and e-wave are smaller than 0.03, and $\kappa_o > \kappa_e$. The reason is the same with that of NLC E7. There is no sharp resonance in 0.2 – 2.0 THz. Thus NLC MDA-00-3461 also exhibits the characteristics of large birefringence, small absorptions and broad temperature range in THz range.

3-4 Summary

In this chapter, we demonstrate the optical constants of the materials in THz range including the calculation principles and the experimental results. In this thesis, we utilize the fused silica substrate and NLC, E7 and MDA-00-3461, for devices design. The knowledge of optical constants of these materials is important for devices design. The experimental results show the fused silica substrate has a small absorption in the investigating THz range. Moreover, the NLCs we use in this work have the characteristics of large birefringence and small absorption in this range. Thus, these materials are all suitable for THz science and applications.



Tables

Table 3-1 NLC Data sheet from Merck Corp.

Properties		E7	MDA-00-3461
Melting point		-10°C	--
Clearing point		61°C	92°C
Optical anisotropy (20°C, 589nm)	Δn	0.2246	0.2578
	n_e	1.7462	1.7718
	n_o	1.5216	1.5140
Dielectric anisotropy (20°C, 1 kHz)	$\Delta\epsilon$	13.8	11.2
	ϵ_{\parallel}	19.0	15.6
	ϵ_{\perp}	5.2	4.4
Elastic constants (20°C)	K_1	11.10 pN	12.6 pN
	K_3	17.10 pN	15.4 pN
	K_3/K_1	1.54 pN	1.22 pN

Reference

- [1] R. A. Soref, and M. J. Rafuse, "Electrically Controlled Birefringence of Thin Nematic Films," *J. Appl. Phys.*, 43, 2029, 1972.
- [2] E. Miraldi, C. Oldano, L. Trossi, and P. Taverna Valabrega, "Direct measurement of the two principal refractive indexes of a nematic liquid crystal slab," *Appl. Opt.*, 21, 4163, 1982.
- [3] C. L. Pan, C. F. Hsieh, R. P. Pan, M. Tanaka, F. Miyamaru, M. Tani, and M. Hangyo, "Control of enhanced THz transmission through metallic hole arrays using nematic liquid crystal," *Opt. Exp.*, 13, 3921, 2005.
- [4] T. T. Tang, "Study on Alignment Properties of Liquid Crystal on the Substrate with Anodic Aluminum Oxide Films and Grooved PDMS Substrate," Ph. D. dissertation in National Chiao Tung University, 2009.
- [5] M. R. Costa, R. A. C. Altafim, and A. P. Mammana, "Electrical Modeling of Liquid Crystal Displays-LCDs," *IEEE Transactions on Dielectrics and Electrical Insulation*, 13, 204, 2006.
- [6] S. Brugioni, and R. Meucci, "Liquid crystals in the mid-infrared region and their applications," *Infrared Physics & Technology*, 46, 17, 2004.
- [7] S. Brugioni, R. Meucci, and S. Faetti, "Refractive indices of liquid crystals E7 and K15 in the mid- and near-IR regions," *J. Opt. Technol.*, 73, 315, 2006.
- [8] M. Evans, M. Davies, and I. Larkin, "Molecular Motion and Molecular Interaction in the Nematic and Isotropic Phases of a Liquid Crystal Compound," *J. C. S. Faraday II*, 69, 1011, 1973.

Figures

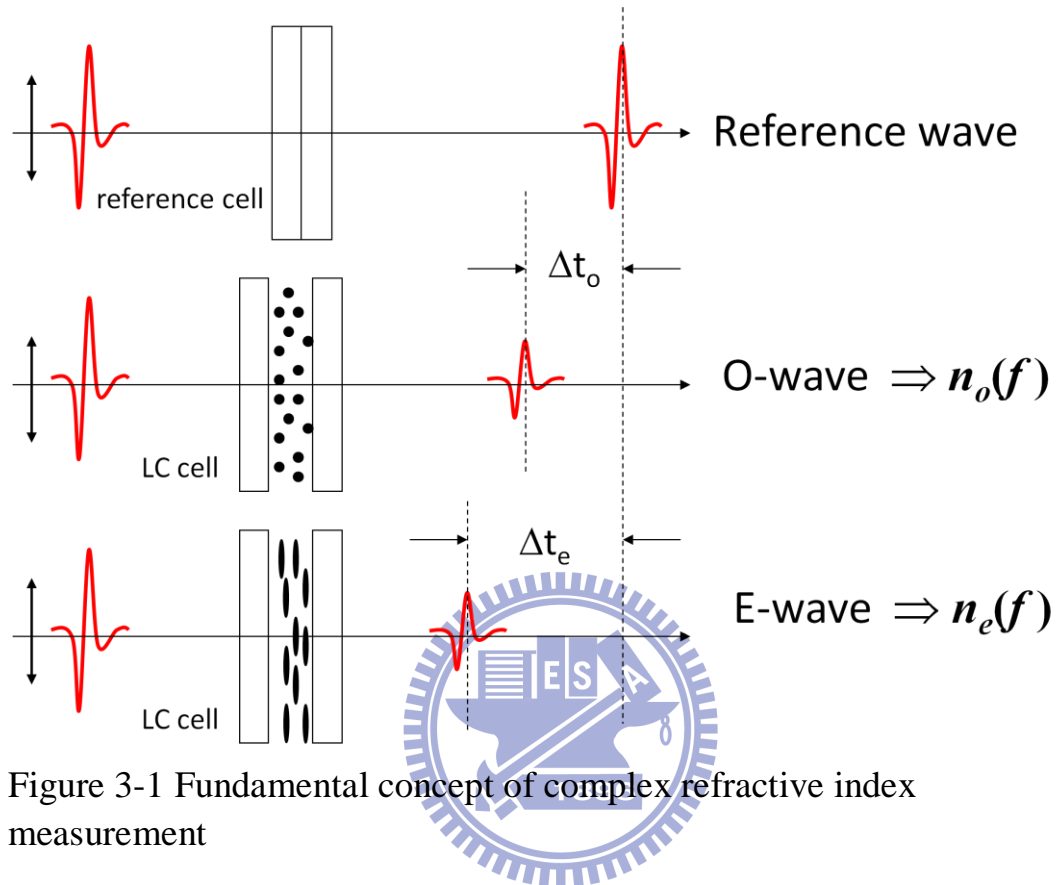
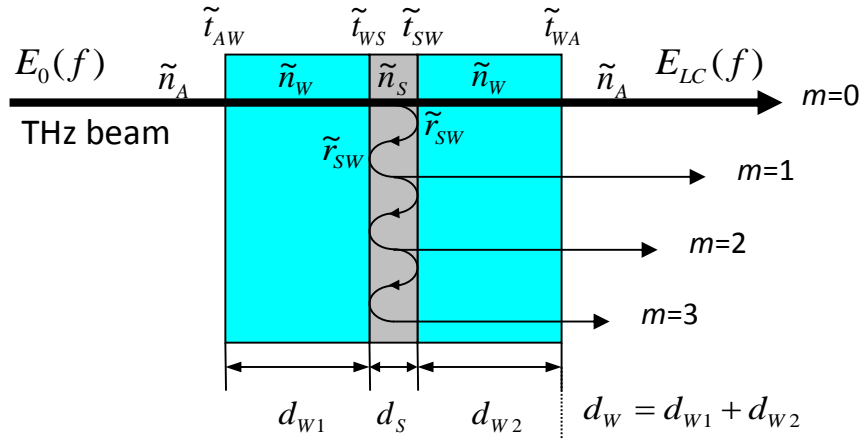


Figure 3-1 Fundamental concept of complex refractive index measurement

(a) cell with two substrates



(b) Two substrates

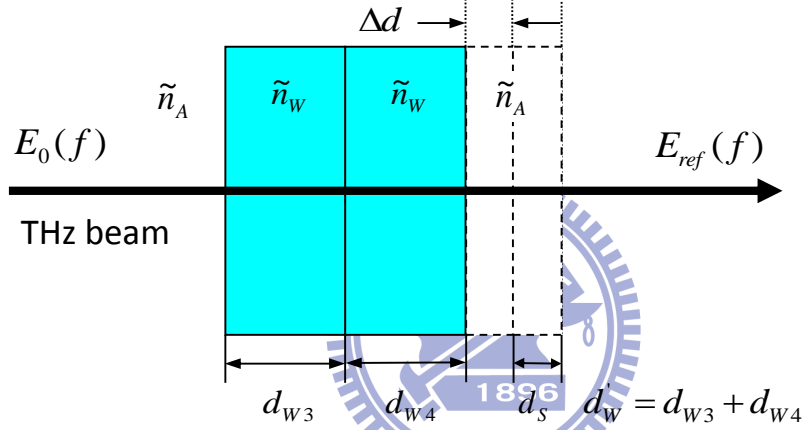


Figure 3-2 THz beam path of (a) LC test cell, and (b) reference cell

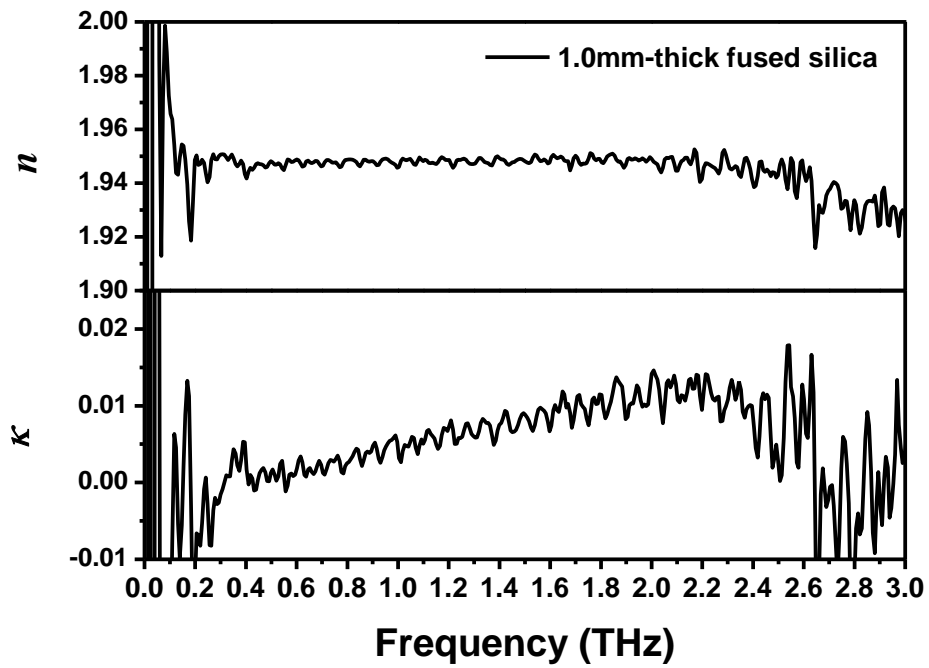


Figure 3-3 Complex refractive indices of 1.0mm-thick fused silica

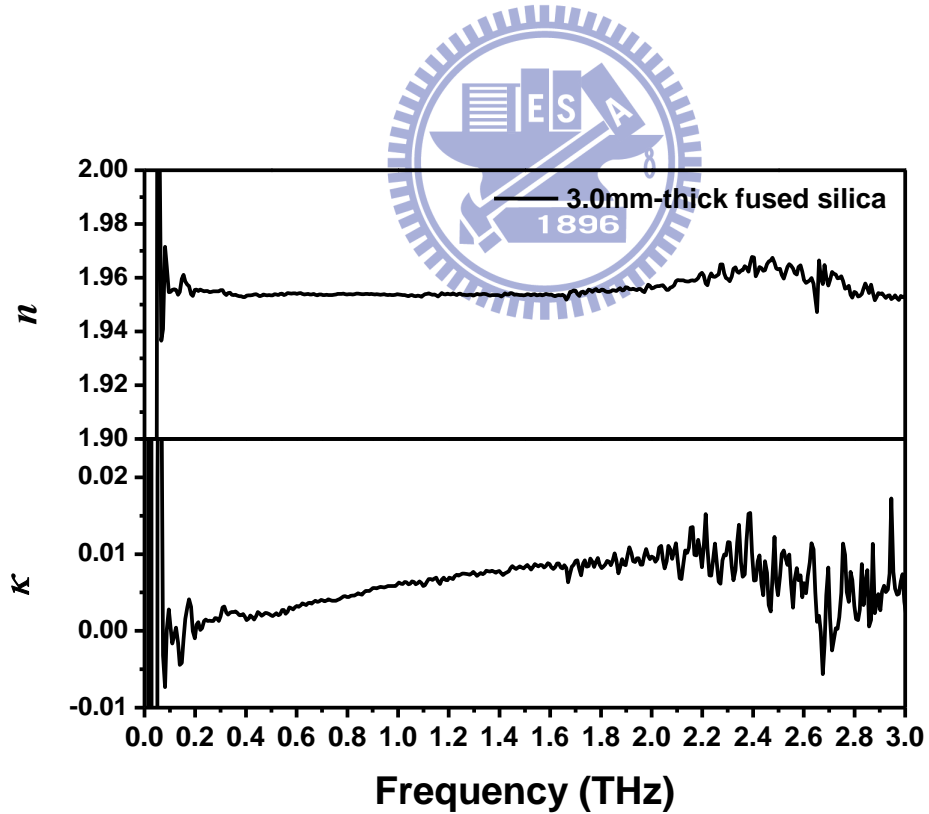


Figure 3-4 Complex refractive indices of 3.0mm-thick fused silica

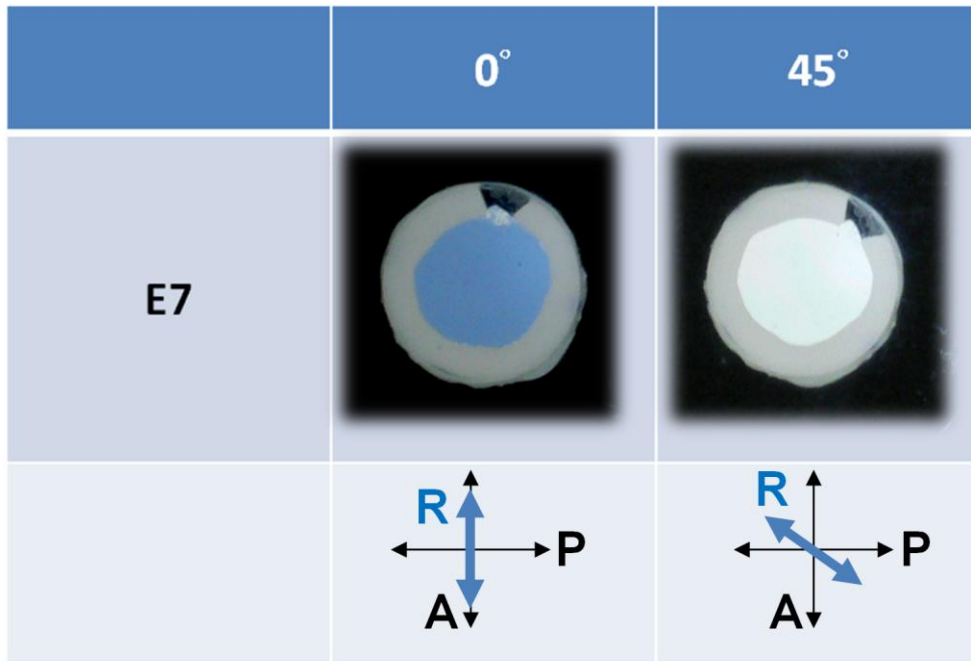


Figure 3-5 Photographs of NLC E7 cell under crossed-polarizers with darkness-state and brightness-state

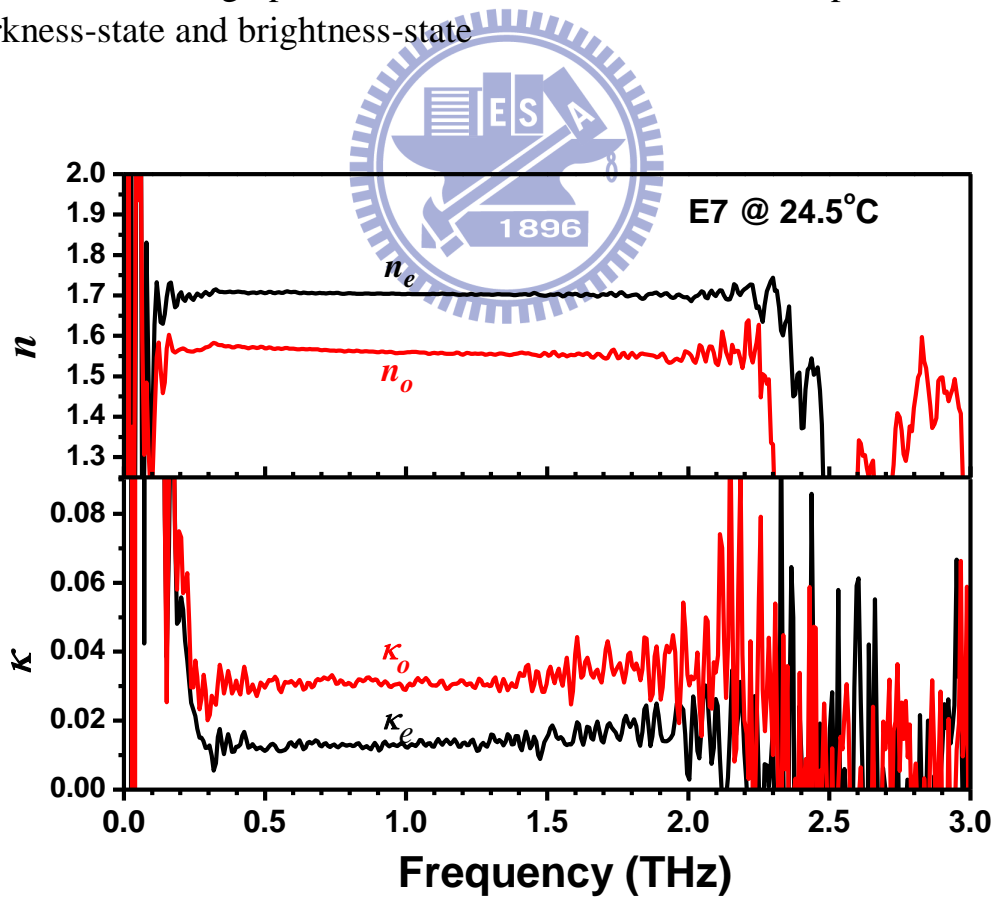


Figure 3-6 Complex refractive indices of NLC E7. Ordinary and extraordinary indices are shown as black and red lines, respectively.

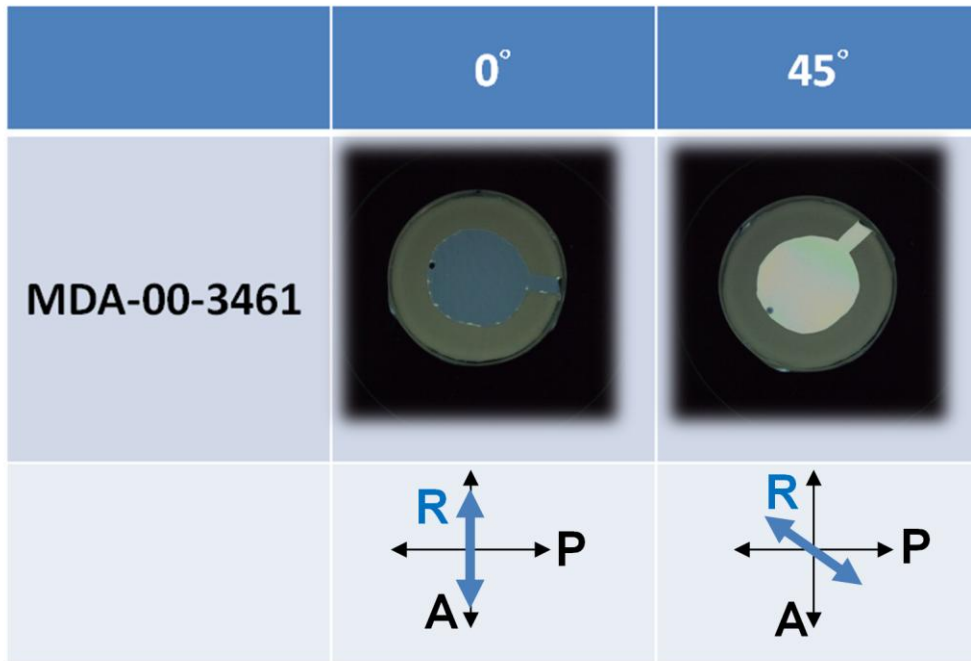


Figure 3-7 Photographs of NLC MDA-00-3461 cell under crossed-polarizers with darkness-state and brightness-state

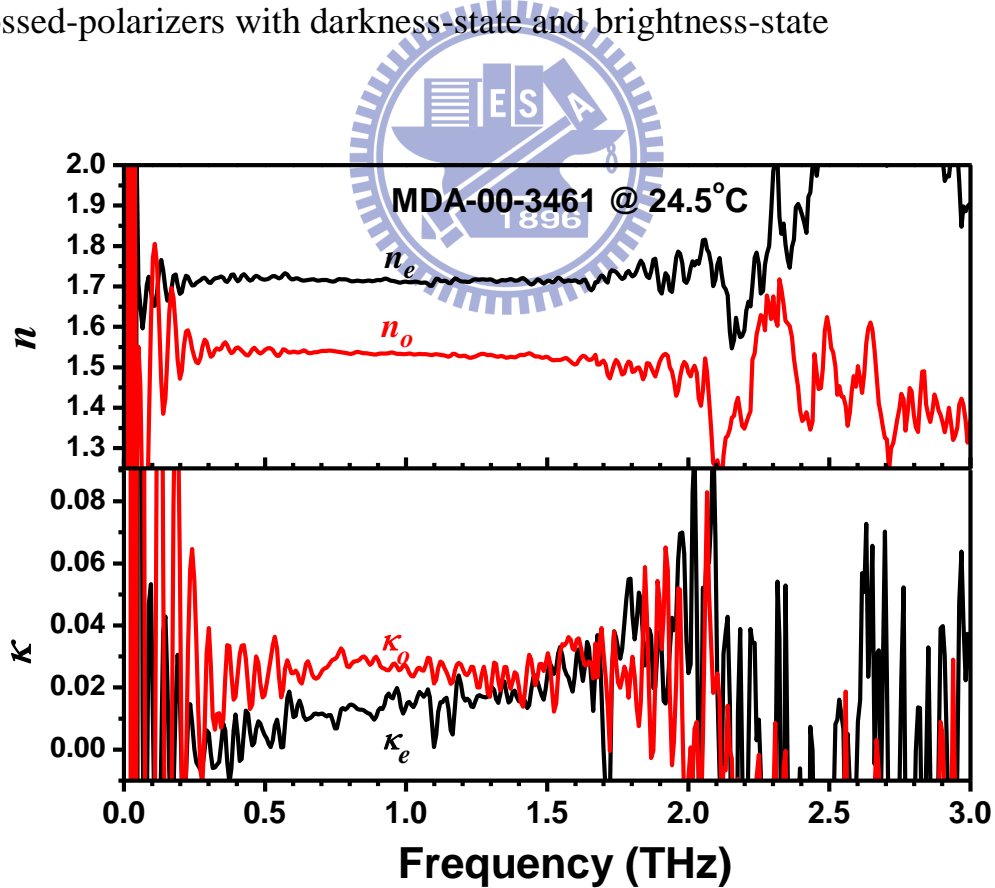


Figure 3-8 Complex refractive indices of NLC MDA-00-3461. Ordinary and extraordinary indices are shown as black and red lines, respectively.

Chapter 4 Manipulating Terahertz Wave by Nematic-Liquid-Crystal Based Grating Structure Devices

Quasi-optical components for sub-millimeter or THz waves are in high demand due to the recent rapid progress in THz science and technology [1, 2]. Periodic structures such as gratings are commonly used to control electromagnetic waves. The use of gratings as couplers and filters was also investigated in THz range [3, 4]. On the other hand, gratings with liquid-crystal-enabled functionalities have been extensively studied as spectrometers, filters, beam splitters, and holographic optical elements for visible and microwave wavelengths [5-8]. Moreover, various tunable THz devices based on NLC, such as phase shifters and filters that are controlled either electrically or magnetically, have been demonstrated in our group [9-11].

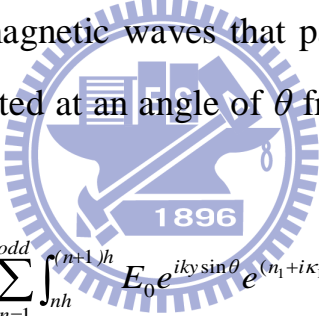
In this chapter, we will demonstrate the NLC based periodic structure devices for manipulating the THz waves. These devices are either electrically or magnetically controlled as beam splitter, phase shifter, or beam steerer. Performances of these devices are in good agreements with theoretical predictions.

4-1 Magnetically controlled phase grating

This work presents for the first time a tunable NLC phase grating in the THz frequency range. The diffraction effect of the grating is magnetically switchable by changing the effective refractive index of the NLC.

4-1.1 Diffraction theory

A generic binary phase grating is sketched in Fig. 4-1. It contains alternate sections of two materials with different refractive indices. The electric fields of electromagnetic waves that pass through materials 1, 2 and the total field E detected at an angle of θ from the incident beam can be written as,



$$\begin{aligned}
 E_1(\theta) &= \sum_{n=1}^{odd} \int_{nh}^{(n+1)h} E_0 e^{iky \sin \theta} e^{(n_1 + i\kappa_1)kd} dy, \\
 E_2(\theta) &= \sum_{n=0}^{even} \int_{nh}^{(n+1)h} E_0 e^{iky \sin \theta} e^{(n_2 + i\kappa_2)kd} dy, \\
 E &= E_1(\theta) + E_2(\theta),
 \end{aligned} \tag{4-1}$$

where E_0 is the amplitude of the incident electric field, θ is the diffraction angle, k is the wave number of the electromagnetic wave in free space, h is the width of each material, d is the thickness of the grating, and $n_1 + i\kappa_1$ and $n_2 + i\kappa_2$ are complex refractive indices of materials 1 and 2, respectively.

For an ideal phase grating, the diffraction efficiency of the m -th order diffracted wave, defined as the intensity ratio of the diffracted beam to that of the incident beam, is given by,

$$\eta_m = \frac{1}{\Lambda^2} \left| \int_{-\Lambda/2}^{\Lambda/2} e^{i\phi} e^{-i(2\pi my/\Lambda)} dy \right|^2, \quad (4-2)$$

where ϕ is the y-dependent phase shift of the grating for one grating period of Λ [12]. Following Ref. 6, we can write

$$\eta_m = \begin{cases} \cos^2(\Delta\phi/2) & \text{if } m = 0, \\ [(2/m\pi)\sin(m\pi/2)]^2 \sin^2(\Delta\phi/2) & \text{if } m \neq 0, \end{cases} \quad (4-3)$$

where $\Delta\phi$ is the relative phase difference between two adjacent domains in the phase grating. For $\Delta\phi = (2n+1)\pi$ ($n = \text{integer}$), the diffraction efficiencies of the odd orders ($m = \pm 1, \pm 3, \pm 5, \dots$) are maximal. Equation (4-3) reveals that the diffraction efficiency of the 3rd order $\eta_{\pm 3} = 4.5\%$ is nine times smaller than that of the 1st order $\eta_{\pm 1} = 40.5\%$. Therefore, we will only consider the 0th and 1st orders of the diffracted beam in this work. Equations (4-2) and (4-3) were used as a guide for designing parameters of the grating. Because only a finite number of grooves are fabricated instead of the infinite number of elements assumed in Eqs. (4-2) and (4-3), experimentally observed efficiencies are expected to be smaller.

4-1.2 Experimental method and setups

A. Sample preparation

Figure 4-2 illustrates schematically our experimental setup and structure of the LC phase grating, which was designed such that the 1st order diffraction efficiency would be highest around 0.3 – 0.5 THz.

Parallel grooves having a period of 2.0 mm, a width of 1.0 mm, and a groove-depth of 2.5 mm were fabricated on a 10.0 mm thick fused silica substrate, for which the refractive index is 1.95 in the THz frequency region (0.2 – 0.8 THz). The grooves were filled with the NLC E7, and sealed with a sheet of Teflon.

The dimensions of the grating were designed to have the maximum range of adjustment for the beam splitting ratio at 0.3 THz. Since E7 is a birefringent material with positive magnetic susceptibility anisotropy, the molecules tend to be aligned parallel to the direction of the applied magnetic field. The applied magnetic field in this work was ~ 1800 G, much higher than the threshold field for reorienting the LC, $H_c \sim 100$ G. We can thus assume that the average direction of LC molecules are reoriented parallel to the magnetic field direction. The incident THz beam was polarized along the y-direction in our setup. The refractive index of E7 could thus be switched from the value for the o-wave (THz field polarized perpendicular to H , $n_o=1.58$) to that for the e-wave (THz field polarized parallel to H , $n_e=1.71$) by changing direction of the magnetic field from the z-direction to the y-direction. The corresponding imaginary indices are κ_o (0.03) to κ_e (0.01). A block of fused silica identical in dimension to that of the grating with a Teflon sheet was prepared as the reference. The data presented below, were obtained at room temperature $23\pm 0.5^\circ\text{C}$.

B. Experimental setups

Two THz investigating setups were used to characterize the

diffraction effect of the device. THz-TDS was utilized to measure the frequency dependant 0th order diffraction spectra of the device. A pair of parallel wire-grid polarizers (Specac, No. GS57204) was placed before and after the device under test.

In the second set of experiments, the broadband THz signal was filtered by a metallic hole array (MHA) to yield a narrow-band THz (0.3 THz) beam [13]. The diffraction pattern of this beam by the grating with various NLC orientations is detected and mapped by a liquid-helium-cooled Si bolometer, which is 20 cm away from the device and located on a rotation arm that can be swung with respect to the fixed grating. The bolometer has an aperture about 2.5 cm in diameter.

4-1.3 Results and discussions

A. THz-TDS measurement results

In Fig. 4-4, we present waveforms of the 0th order diffracted THz pulses transmitted through the phase grating for both extraordinary and ordinary waves and that of the reference (black, red, and blue curves). An oscillating component can be seen arriving 1.9 ps and 3.1 ps before the main pulse for extraordinary and ordinary waves, respectively. This is attributed to the propagation time difference between the waves through fused silica and LC. The calculated times, $\delta nd/c$, where δn is the difference of the refractive indices between fused silica and LC, d is the groove depth, and c is the speed of light in vacuum, are 2.0 ps and 3.1 ps, respectively. They are very close to the experimentally observed time

difference.

Applying fast Fourier transform algorithms to time domain waveforms and normalizing the diffracted signals for e-ray and o-ray with respect to that of the reference, we are able to determine the corresponding diffraction efficiencies, η , in the frequency domain (see Fig. 4-5). The solid and dashed lines are theoretical curves calculated using Eq. (1) for the ordinary and extraordinary waves, respectively. The experimental data were in good agreement with the predictions by classical diffraction theory, i.e., Eq. (1). Figure 4 clearly demonstrated that the diffraction efficiency was highest at the frequency of 0.3 THz, according to our design. For ordinary wave at 0.3 THz, the phase difference $\Delta\phi$ between fused silica and E7 was close to 2π . Therefore, the transmission of the grating was higher and the diffraction efficiency was 0.37. The THz wave was mainly concentrated in the 0th order. In contrast, the phase difference $\Delta\phi$ is close to π for extraordinary waves. The diffraction efficiency was 0.10 for the 0th order, because the THz wave was mostly diffracted into the 1st order. A straightforward analysis of the spectral phase was also performed. It does not shed further light on operation of the device.

B. Diffraction profile measurement results

A liquid-helium-cooled Si bolometer was employed to trace the angular distribution of the diffracted THz beam by the LC phase grating. In these experiments, the broadband THz pulse was filtered by the MHA (a 0.5 mm-thick aluminum plate perforated with circular holes arrayed in

a triangular lattice of lattice constant $s = 0.99$ mm and the diameter of each hole, $l = 0.56$ mm) as a filter to yield a quasi-monochromatic wave centered at 0.3 THz with a line width of 0.03 THz [13].

Figure 4-6 illustrated the diffracted intensity profiles of the 0.3 THz-beam polarized in the y-direction. The measured diffraction efficiencies for 0th and 1st orders were 0.43 and 0.08 for o-ray, 0.13 and 0.23 for e-ray, respectively. These were also in good agreement with the theoretical estimate, taking into account of the finite dimension of the grating and acceptance angle of the bolometer. The acceptance angle of $\pm 3^\circ$ associated with the detection area of the bolometer was considered and the result predicted by Eq. (4-1) adjusted accordingly.

A diffraction maximum was detected at $\theta = 30^\circ$, which corresponded to the 1st order diffracted beam that was predicted by the grating equation. As mentioned in the preceding paragraph, when the phase difference $\Delta\phi$ was close to 2π , most of the THz signal propagated in the direction of the 0th order diffraction if the refraction index of E7 was n_o . Experimentally, we found the diffraction efficiencies were 0.43 and 0.08 for the 0th and 1st orders diffracted beams, respectively. When the phase difference $\Delta\phi$ was close to π , the refractive index of E7 was n_e and the THz wave mostly propagated as 1st order diffracted beam. The diffraction efficiencies were 0.13 and 0.23 for the 0th and 1st orders diffracted beams, respectively. The grating thus served as a variable beam splitter. Rotating the magnetic field direction enabled the beam splitting ratio between the 0th and 1st orders diffracted beams to be tuned from 4:1 to 1:2.

If the THz beam was linearly polarized in any other direction, the

phase grating also showed the potential for operating as a switchable polarizing beam splitter. Figure 4-7 shows the experimental results measured using the same setup as described above as well as the theoretical curves. The polarization of the incident 0.3 THz-beam was set by rotating the wire-grid polarizer before the grating to an angle of 45° with respect to the y-direction while the magnetic field remained in the y-direction. The transmitted y-polarized THz beam propagated mostly as the 1st order diffracted beam, while the z-polarized THz wave mostly propagated as the 0th order diffracted beam. When the applied magnetic field was switched to that along the z-direction, the diffraction patterns of the above two polarized THz waves were interchanged.

4-1.4 Summary



In summary, a magnetically controlled tunable LC phase grating for manipulating the THz wave at room temperature was demonstrated. The waveform of the broadband THz wave was modified in the time-domain and the spectral transmittance could be varied in the frequency-domain. The splitting ratio of the diffracted THz-beam (0.3 THz) polarized in a direction perpendicular to that of the grooves of the grating could be tuned from 4:1 to 1:2. Additionally, when the THz wave was polarized in any other direction, this device had the potential to operate as a polarizing beam splitter.

4-2 Electrically controlled phase grating

In this work, we proposed and demonstrated an electrically controlled phase grating using NLC for THz waves. Performance of the device is in good agreement with theoretical predictions. For practical application, the insertion loss of the device should be as low as possible. We also discussed how to lower the insertion loss of the devices in detail.

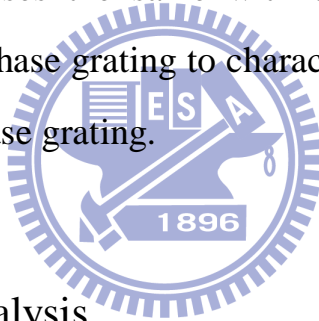
4-2.1 Experimental method and setups

Figure 4-8 is the schematic structure of the electrically controlled THz phase grating. The incident THz wave is polarized in the y-direction. Orientations of the LC molecules for two possible configurations are also shown. The device is designed such that the zeroth-order diffraction efficiency would be highest in the band around 0.3 – 0.5 THz, which is the most distinguishable region for photoconductive antenna made of LT-GaAs.

Parallel grooves having a period of 2.0 mm, a width of 1.0 mm, and a groove-depth of 2.5 mm are fabricated by stacking Indium Tin Oxide (ITO) coated fused silica substrates, for which the refractive index is 1.95 in the sub-THz frequency region (0.2 – 0.8 THz). The surfaces of the fused silica substrates are coated with polyimide (PI, SE-130B by Nissan), and then rubbed for homogenous alignment. The grooves are filled with the NLC E7 and sealed with a sheet of fused silica coated with DMOAP. At room temperature, E7 is a birefringent material with positive dielectric

anisotropy. Its molecules tend to be aligned parallel to the direction of the applied electric field when the applied voltage is larger than the threshold voltage. The effective refractive index of E7, n_{eff} , can be tuned from the value for the ordinary refractive index ($n_o = 1.58$) to that for the extraordinary refractive index ($n_e = 1.71$) by varying the applied voltage. To simplify handmade sample constitution, previously, we use larger substrates to fabricate the device. A stack of ITO-coated fused silica plates identical in dimension to that of the grating was prepared as the reference. Later, for analyzing the insertion loss, another phase grating was fabricated with smaller fused silica substrates.

We utilized apparatuses the same with that in the experiment of magnetically controlled phase grating to characterize the properties of the electrically controlled phase grating.



4-2.2 Insertion loss analysis

To estimate the insertion loss of the THz grating, we regarded this device as stacked parallel-plate waveguides. Considering the ITO conductive film is not a perfect conductor and the way we excited the waveguide, we can assume TM mode propagation. The cutoff frequency of parallel-plate can be written as $f_c = \frac{c}{2nl}$, where c is the velocity of light, l is the distance between two conductive layers, and n is the refractive index of the dielectric material within the waveguide. The respective attenuation constants α_c and α_d corresponding to conductor loss and dielectric loss can be given by [14, 15]

$$\alpha_c = \sqrt{\frac{\pi f \varepsilon}{\sigma_c}} \frac{2}{l \sqrt{(f_c / f)[1 - (f_c / f)^2]}} , \quad (4-4)$$

$$\alpha_d = \frac{\pi f \tan \delta \sqrt{\varepsilon_r}}{2c \sqrt{1 - (f_c / f)^2}}$$

where f is the frequency, ε is the permittivity of the dielectric material, σ_c is the conductivity of the electrode, $\tan \delta$ is the loss tangent, and ε_r is the relative permittivity of the dielectric material. For practical use, the insertion loss should be as low as possible. Two different base dimensions of the sample ($h_1=17.5$ mm and $h_2=7.5$ mm) are prepared to analyze the loss caused by the base.

4-2.3 Results and discussions

A. THz-TDS measurement results

The zeroth-order diffracted THz pulses transmitted through the phase grating for both ordinary and extraordinary waves, (black and red curves), are shown in Fig. 4-9 (a). For comparison, we also plotted the incident and the transmitted THz waveforms through the reference (the blue and cyan curves). The signals that passed through the reference and the device are 3 times magnified in Fig. 4-9 (a).

Figure 4-9(a) clearly shows oscillating components arriving 3.0 ps and 1.9 ps before the main pulse for ordinary and extraordinary waves, respectively. These are attributed to the propagation time difference between the waves through fused silica and NLC. The calculated times, $\delta n d / c$, where δn is the difference of the refractive indices between fused silica and NLC, d is groove depth and c is the speed of light in vacuum, are 3.1 ps and 2.0 ps, respectively. These are very close to the

experimental observed time difference. The spectral characteristics for all cases discussed in Fig. 4-9 (a) are illustrated in Fig. 4-9 (b).

The diffraction efficiencies, η , in the frequency domain can be determined by normalizing the diffracted signals in the frequency domain with respect to that of the reference. A finite-difference time-domain (FDTD) algorithm (RSoft Design Group, Inc.) is employed to simulate the diffraction of THz waves transmitted through the device as shown in figure 4-10 (a). In the FDTD simulation, the size of the grid is $10\mu\text{m} \times 10\mu\text{m}$ while the time step is 1.67×10^{-14} s. Figure 4-10 (b) shows the experimentally determined diffraction efficiencies as a function of frequency with the device operating at 0, 15, 20, and 90 V. The FDTD simulation and experimental results are in general agreement. There are, however, some discrepancies in efficiencies and peak positions. This is acceptable, as the thickness of the fused silica plates in the grating assembly varies by ± 0.1 mm. Further FDTD simulations show such variations could change efficiencies by 0.1 and the peak positions by 0.02 THz.

The experimental diffraction efficiency is highest near 0.3 THz, in agreement with the designed frequency. For ordinary wave at 0.3 THz, the phase difference between fused silica and E7 is close to 2π . Therefore, the transmission of the grating is higher. The THz wave is mainly concentrated in the zeroth-order. In contrast, the phase difference is close to π for extraordinary waves. The diffraction efficiency is smaller for the zeroth-order, because the THz wave is mostly diffracted into the first order.

There is a little shift between experimental results and simulations. We suppose this disagreement attributes to the misassembling of handmade devices. The phase grating is designed to have alternate 2.5mm thick fused silica and LC layers. We estimate that there is about 0.1mm misassembling of the grating because the prepared substrates are non-uniform and have about 0.1mm deviation. It can shift the efficiency about 0.1 and the maximum position can also be shifted about 0.02 THz. Figure 4-11 (a) and (b) show diffraction efficiency curves for the 2.4, 2.5, and 2.6mm thick grating calculated by FDTD soft for o-wave and e-wave, respectively. Randomly arrangement within 0.1mm deviation for simulating sample misassembling is also shown in figures. The shifts of the curves are clear. Therefore, we suppose the experimental results are reliable.

The periodic arranged ITO film can be considered as a wire-grid polarizer. Only the THz wave polarized perpendicular to the grooves can pass through the electrically-tuned phase grating. The extinction ratio is 100:1 at 0.3 THz.

B. Diffraction profile measurement

Figure 4-12 illustrates the intensity profiles of the diffracted 0.3-THz-beam polarized in the y-direction. A diffraction maximum is detected at $\phi = 30^\circ$, which corresponds to the first order diffracted beam that is predicted by the grating equation. The measured diffraction efficiencies for zeroth- and first-orders are also in good agreement with the theoretical values predicted by Eq. (4-1), taking into account the finite

dimension of the grating and acceptance angle of the bolometer ($\pm 3^\circ$).

When the E7 molecules are aligned such that the refractive index is n_o , the phase difference is close to 2π . Most of the THz signal propagates in the direction of the zeroth-order diffraction. Experimentally, we find the diffraction efficiencies are 0.62 and 0.06 for the zeroth- and first-orders, respectively. On the other hand, when the E7 molecules are aligned such that the refractive index is n_e , the phase difference is close to π . The THz wave propagates mostly as the first-order diffracted beam. The diffraction efficiencies are 0.18 and 0.25 for the zeroth- and first-orders, respectively. The grating would then function as a variable beam splitter. Varying the applied voltage, the beam splitting ratio of the zeroth- to the first-orders can be tuned from 10:1 to 1:1.

C. Insertion loss analysis

Figure 4-13 shows the diffraction efficiency of the device obtained by normalizing the diffracted signals for o-ray and e-ray with respect to that of air. The experimentally measured diffraction efficiency for o-ray at 0.3 THz is about 0.07. The diffraction efficiency for o-wave at 0.3 THz predicted by classic diffraction theory or evaluated by FDTD simulation are about 0.45. The loss of the device is thus -8.0 dB for o-wave at 0.3 THz. Similarly, the diffraction efficiency for e-wave at 0.5 THz is about 0.046, as opposed to theoretical prediction is about 0.45. The loss value of the grating for e-wave at 0.5 THz is therefore -10 dB. Another shorter grating device in the base ($h=7.5\text{mm}$) is prepared to compare the effect of insertion loss. The diffraction efficiency of the shorter device obtained by

normalizing the diffracted signals for o-wave and e-wave with respect to that of air are shown in fig. 4-13 (b). The diffraction efficiency of the shorter device is obviously higher than the larger one. The experimentally measured diffraction efficiency for o-wave at 0.3 THz is about 0.11, and the loss is -6.1 dB. The diffraction efficiency for e-wave at 0.5 THz is about 0.083, and the loss value is -7.4 dB.

The resistivity of ITO is $1.5 \times 10^{-6} \Omega\text{m}$, thus $\sigma = 6.7 \times 10^5 \text{ S/m}$ [16]. The parameters of fused silica and LC with different diffractive index at the frequency of 0.2-0.8 THz are shown in Table 4-1. Following eq. (4-4), the estimated loss value can be obtained. For larger grating device ($h=17.5\text{mm}$), the total loss for o-wave at 0.3 THz and for e-wave at 0.5 THz are estimated -9.0 dB and -13 dB, respectively. Similarly, for shorter grating device ($h=7.5\text{mm}$), the total loss for o-wave at 0.3 THz and for e-wave at 0.5 THz are estimated -5.5 dB and -6.9 dB, respectively. Table 4-2 shows the estimated and measured results in details. The discrepancy could be due to finite collection efficiency of the detection system and misassembling of the sample structure. As the experimental results, by decreasing the thickness of fused silica plates in the base of the device, the insertion loss can be reduced to lower.

D. Response of device

For NLC devices utilizing, the response time of the device may be concerned. The turn-on and turn-off times are measured by monitoring the pulse signal (electric field) variation in time domain with THz-TDS. The signal profiles in time domain are shown in Fig. 4-14 which also

demonstrates the monitoring position of THz-TDS for the response time measurement. Figure 4-15 (a) and (b) show the normalized power as functions of time for driving voltage at voltage-on and voltage-off states, respectively. We defined that rising time is the duration of driving voltage turned on to the power reduced to 37% of the maximum. Falling time is the duration of driving voltage turned off to the power increased to 63% of the maximum. The rising and falling times of the grating are about 23 and 290 seconds, respectively. The phase grating does not have fast response because of the thick LC layer. As a result, the present device is not suitable for applications that require fast modulation. Instead, the device is excellent for instrumentation or apparatus that require, e.g., a fixed beam splitting ratio with occasional fine tuning.

4-2.4 Summary



In this work, we successfully demonstrated the electrically controlled liquid-crystal-based phase grating for manipulating the terahertz waves. This device can be utilized as a tunable terahertz beam splitter and its beam splitting ratio of the zeroth- to the first-order diffractions can be tuned from 10:1 to 1:1. The finite-differential time-domain simulation was used to investigate the diffraction effect of the phase grating. The experimental and simulation results were in general agreement. The signal losses of this device were also discussed and the insertion loss can be reduced by decreasing the thickness of fused silica plates in the base of the device. The phase grating does not have fast response because of the thick LC layer. As a result, the present device is not suitable for

applications that require fast modulation. Instead, the device is excellent for instrumentation or apparatus that require, e.g., a fixed beam splitting ratio with occasional fine tuning.

4-3 Electrically controlled beam steerer

Recently, the development of a reconfigurable antenna, which can electrically steer radiation beams or vary beam shapes, are interesting due to the emergence of many applications, such as adaptive wireless and satellite communication networks and automobile radar systems [17, 18]. The concept of beam steering using the LC to construct the phase array in millimeter wave range has been reported [14]. In this work, we utilize the NLC MDA-00-3461 (Merck) to construct an electrically tunable phase shifter array device to modulate the phase of THz beam. By applying different voltages on each part of the phase array, we can yield a gradient phase shift. Therefore, the incident THz wave can be steered towards a selected direction.

4-3.1 Experimental principles

We designed the THz beam steerer as an electrically tunable phase shifter array. Figure 4-16 shows the structure of the phase shifter array, which is constructed by alternately stacking a number of NLC layers and electrodes. Voltage sources are connected to the electrodes to apply control voltages to each NLC layer. The effective refractive index, $n_{eff}(V)$, of NLC of each layer can be electrically tuned by applying voltage. The

polarization of the THz wave was along z-direction and the wave was normally incident to the device. The way we designed how the device worked was that when no voltage was applied, the NLC molecules are aligned along the y-direction, the effective refractive index equals to ordinary component n_o . While sufficient control voltage is applied, the NLC molecules orientate toward to the direction parallel to the polarization of THz wave (z-direction), or the effective refractive index equals to extraordinary component n_e . The traversing time, which the THz wave takes to pass through the NLC layers, can be changed by applying voltages. The corresponding phase shift $\Delta\phi(V)$ in the applying voltage V is given by

$$\Delta\phi(V) = kd(n_o - n_{eff}(V)), \quad (4-5)$$

where k is the wave number in free space and d is the propagation length of the NLC layer. When a certain phase gradient was created across the aperture of the device by adjusting the phase shift in each NLC layer, the wavefront of the transmitted wave was inclined against the aperture. According to the limited voltage source channels, we divided two NLC layers as a block. The steering angle θ can be determined by the aperture size A and the optical length delay Δd between the top NLC block and the bottom NLC block. The optical length delay Δd was according to the phase shift between the top and bottom NLC blocks $\Delta\phi_{max}$. Therefore, the relationship between steering angle θ , optical length delay Δd , and the phase shift $\Delta\phi_{max}$, was shown in Fig. 4-16 (a), and can be written as,

$$\Delta d = \frac{\Delta\phi_{max}}{2\pi} \lambda, \text{ and } \tan\theta = \frac{\Delta d}{A}. \quad (4-6)$$

where λ is the corresponding wavelength of THz wave.

Accordingly, the THz wave can be steered by the control voltage. The phase shift $\Delta\phi_i$ in the certain i th NLC block, in our case can be written as,

$$\Delta\phi_i = (i-1)k(2h)\tan\theta, \quad (4-7)$$

where $2h$ was the thickness of the i th NLC block, and θ was the steering angle against the normal of the aperture. We can see the construction of the device in Fig. 4-16 (b), in which each NLC block includes two NLC layers and two electrodes.

4-3.2 Experimental method and setups

A. Sample preparation

We used the 550- μm -thick Teflon sheet as the spacer and the 100- μm -thick copper foil as the electrode. The copper foil was coated with PI Nissan SE-130B on both sides and rubbed for homogeneous alignment along y-direction before applying the voltage. The 18 NLC layers and 19 electrodes were stacked up alternately. The total thickness of the device was 12.1mm, which corresponded to the size of the aperture, A , along z-direction. The size of the aperture along x-direction was designed to be 20.0mm, and the propagation length, d , of the THz wave was designed to be 10.0mm. Control voltage sources connected to the electrodes provided 1kHz-sinusoidal waves to the NLC layers.

According to the data sheet as shown in Tab. 3.1, the threshold voltage V_c can be estimated by $V_c = \pi (k/\epsilon_0 \Delta\epsilon)^{1/2} = 1.20 \text{ V}_{\text{rms}}$. The complex refractive indices of NLC MDA-00-3461 for ordinary and extraordinary in THz range are $n_o=1.54$, $n_e=1.72$, $\kappa_o=0.03$, and $\kappa_e=0.01$, respectively. At

a frequency of 0.3 THz, the estimated maximum phase shift applied to a propagation wave passing through NLC layer would be 11.31 rad, which is calculated by Eq. 4-5 and the refractive indices of NLC MDA-00-3461. The maximum steering angle was estimated to be approximately 9° from Eq. (4-7) taking the maximum phase shift and aperture size into account.

B. Experiment setups

The constructed THz beam steerer was characterized by THz-TDS for phase shift measurement. For THz beam steering, we improved the THz-TDS for movable detecting part to measure the steered THz signal. We used a 1m-long single mode fiber (F-SF-C-1FC, from Newport Corp.) to guide the femtosecond laser directly to the detecting antenna, and the optical length was fixed when the detecting part was moved. The schematic diagram of the setup is shown in Fig. 4-17. The detecting part was 20 cm away from the sample and located on a rotation arm that can be swung with respect to the fixed sample. The laser pulse would be broader due to the dispersion in the fiber, and the detected THz pulse became broader in time domain as shown in Fig 4-18. In the frequency domain, the THz bandwidth became narrower and the detected signal was mainly below 1THz as shown in Fig.4-19. It has been reported that the frequencies below 0.5THz are almost independent of the optical pulse widths, THz frequency spectra above 0.5THz change markedly with the excited pulse width which is irradiated to the detector [19]. The improved THz-TDS can detect the steered THz pulse and the cost can be lower than that of using liquid-helium-cooled Si bolometer.

4-3.3 Results and discussions

A. Sample test

Before injecting NLC in the sample, the structure of the device was similar with wire-grid polarizer, and we measured its transmitted signal with THz-TDS. We defined the S-state and P-state as the polarization of THz wave was perpendicular or parallel to the electrodes, respectively. As prediction, the grating structure worked as a wire-grid polarizer and the most signal can pass through the device in S-state, but not in P-state. The construction of the experiment and the transmitted spectra are shown in Fig. 4-20. Figure 4-21 shows the extinction ratio as the function of frequency.



B. Phase shift

The phase shift against the control voltage was measured under conditions where control voltages were applied equally to all NLC layers. Figure 4-22 shows the THz pulses in time domain. It is obviously that the pulses delay increase as applying voltages increased, as the NLC molecules re-orientate gradually from ordinary to extraordinary refractive index. Applying FFT analysis, the phase shift as a function of frequency is shown in Fig. 4-23. The phase shift increased with increasing applying voltages. Figure 4-24 plots the phase shift at 0.3 THz as a function of the control voltage. Above the threshold voltage, as the prediction, $1.20 V_{\text{rms}}$, the phase shift increases as the applying voltage increases. The maximum phase shift reached approximately 11.24 rad. This value is in close agreement with the calculated value.

C. Beam steering

We measured the beam steering characteristics with the improved THz-TDS. Although the applying voltage should be adjusted layer-by-layer for beam steering, only 9 control voltages was applied to each NLC block consisting 2 NLC layers. As phase shift $\Delta\phi_i$ in each NLC block needed for beam steering is given by Eq. (4-6), the control voltage corresponding to phase shift can be determined from the experimental results in Fig. 4.23, and are shown in Table 4-3.

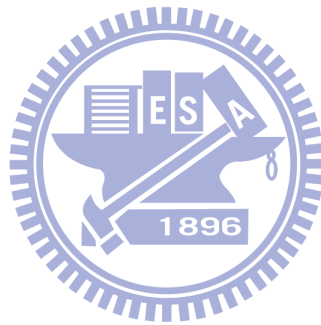
The experimental results including the radiation pattern at $\theta=0^\circ$ are shown in Fig 4-25 in the time domain. Figure 4-25 (a) shows the THz signal before transmitted to the device, and (b) and (c) show the THz signal transmitted the device with ordinary and extraordinary refractive indices at $\theta=0^\circ$, respectively. The main beam was steered in the direction of $\theta= 8.5^\circ$ as the control voltages were varied to yield the phase gradient as shown in (d). The signal vanishes as we removed the device as shown in (e). Applying FFT analysis, the corresponding THz spectra in frequency domain are shown in Fig 4-26. According to the results, the device can steer the broadband THz signal mainly under 0.5THz.

4-3.4 Summary

We demonstrated a grating structure phase shifter array that can be the THz shifter and THz beam steerer. An improved THz-TDS was constructed for characterizing the properties of the device. The improved THz-TDS has movable detecting part, which can detect the THz signal at various positions. It can detect the THz pulse directly and can be more

convenient and lower cost than that using the liquid-helium-cooled Si bolometer.

For phase shift, applying the controlled voltages equally on the NLC layers of the device to vary the refractive index of NLC can shift the phase of THz signal. For beam steering, the broadband THz signal below 0.5 THz can be steered to the direction that has 8.5° with respect to the incident beam as the control voltages were varied to yield the phase gradient. The experimental results are in good agreement with theoretical predictions.



Tables

Table 4-1. Parameters of the fused silica and NLC E7

Material	Fused silica	E7 (n_o)	E7 (n_e)
ϵ_r	3.80	2.50	2.92
ϵ_i	0.008	0.095	0.041
$\tan\delta$	0.0021	0.038	0.014

Table 4-2. Insertion loss of phase grating

Phase grating	h=17.5mm		h=7.5mm	
	0V (n_o) At 0.3THz	90V (n_e) At 0.5THz	0V (n_o) At 0.3THz	90V (n_e) At 0.5THz
(Estimated)				
Conductor loss	4.7 dB	7.8 dB	2.3 dB	3.8 dB
Dielectric loss	4.3 dB	4.9 dB	3.2 dB	3.1 dB
Total	9.0 dB	13 dB	5.5 dB	6.9 dB
Measured value	8.0 dB	11.0 dB	6.1 dB	7.4 dB

Table 4-3 Control voltage and corresponding phase shift at 0.3 THz

	Applied Voltage (V_{rms})	Phase shift (rad) at 0.3 THZ
V_1	0	0
V_2	1.32	1.41
V_3	1.44	2.81
V_4	1.57	4.22
V_5	1.77	5.62
V_6	2.18	7.03
V_7	2.96	8.43
V_8	2.88	9.84
V_9	28.80	11.24

Reference

- [1] P. Goldsmith, "Quasi-optical techniques," *Proc. IEEE*, 80, 1729, 1992.
- [2] M. Tonouchi, "Cutting-edge terahertz technology," *Nature Photonics*, 1, 97, 2007.
- [3] F. Garet, J. -L. Coutaz, M. Narzarov, E. Bonnet, O. Parriaux, and G. Racine, "THz time-domain spectroscopy study of grating couplers and segmented grating filters," *Digest of Joint Int. Conf. on Infrared and Millimeter Waves and Terahertz Electron.*, 181, 2004.
- [4] R. Kersting, G. Strasser and K. Unterrainer, "Terahertz phase modulator," *Electron. Lett.*, 36, 1156, 2000.
- [5] J. Chen, P. J. Bos, H. Vithana, and D. L. Johnson, "An electro-optically controlled liquid crystal diffraction grating," *Appl. Phys. Lett.*, 67, 2588, 1995.
- [6] Jae-Hong Park, Chang-Jae Yu, Jinyool Kim, Sung-Yeop Chung, and Sin-Doo Lee, "Concept of a liquid-crystal polarization beamsplitter based on binary phase gratings," *Appl. Phys. Lett.*, 83, 1918, 2003.
- [7] Fuzi Yang, and J. R. Sambles, "Microwave liquid-crystal variable phase grating," *Appl. Phys. Lett.*, 85, 2041, 2004.
- [8] F. Vita, A. Marino, V. Tkachenko, G. Abbate, D. E. Lucchetta, and F. Simoni, "Visible and near-infrared characterization and modeling of nanosized holographic-polymer-dispersed liquid crystal gratings," *Phys. Rev. E*, 72, art. 011702, 2005.
- [9] Hsin-Ying. Wu, Cho-Fan Hsieh, Tsung-Ta. Tang, Ru-Pin Pan, and Ci-Ling. Pan, "Electrically Tunable Room-Temperature 2π Liquid Crystal

- Terahertz Phase Shifter,” *IEEE Photon. Technol. Lett.*, 18, 1488, 2006.
- [10] Chao-Yuan Chen, Cho-Fan Hsieh, Yea-Feng Lin, Ci-Ling Pan, and Ru-Pin Pan, “Liquid-crystal-based terahertz tunable Lyot filter,” *Appl. Phys. Lett.*, 88, art. 101107, 2006.
- [11] Chao-Yuan Chen, Cho-Fan Hsieh, Yea-Feng Lin, Ru-Pin Pan, and Ci-Ling Pan, “Magnetically tunable room-temperature 2π liquid crystal terahertz phase shifter,” *Opt. Exp.*, 12, 2625, 2004.
- [12] Joseph W. Goodman, “Introduction to Fourier Optics,” 2nd ed., McGraw-Hill, 1996.
- [13] Ci-Ling Pan, Cho-Fan Hsieh, Ru-Pin Pan, Masaki Tanaka, Fumiaki Miyamaru, Masahiko Tani, and Masanori Hangyo, “Control of enhanced THz transmission through metallic hole arrays using nematic liquid crystal,” *Opt. Exp.*, 13, 3921, 2005.
- [14] H. Kamoda, T. Kuki, H. Fujikake, and T. Nomoto, “Millimeter-wave beam former using liquid crystal,” *Proc. 34th European Microwave Conf.*, Amsterdam, Netherlands, 1141, 2004.
- [15] David K. Cheng, “Field and Wave Electromagnetics,” 1st ed., Addison-Wesley, 1983.
- [16] Adrian Dobroiu, Masatsugu Yamashita, Yuichi N. Ohshima, Yasuyuki Morita, Chiko Otani, and Kodo Kawase, “Terahertz imaging system based on a backward-wave oscillator,” *Appl. Opt.*, 43, 5637, 2004.
- [17] H. Tsuji and M. Mizuno, “Applications of adaptive array antenna in mobile communications,” *IEJCE Trans. Fundamentals (Japanese Edition)*, J82-A, 779, 1999.
- [18] S. Tokoro, K. Kuroda, A. Kawakube, K. Fujita, and H. Fujinami,

“Electronically scanned millimeter-wave radar for pre-crash safety and adaptive cruise control system,” *Proc. 4th Intelligent Vehicles Symp.*, 304, 2003.

[19] R. Inoue, T. Ohno, and M. Tonouchi, “Development of Fiber-Coupled Compact Terahertz Time-Domain Spectroscopy Imaging Head,” *Jpn. J. Appl. Phys.*, 45, 7928, 2006.



Figures

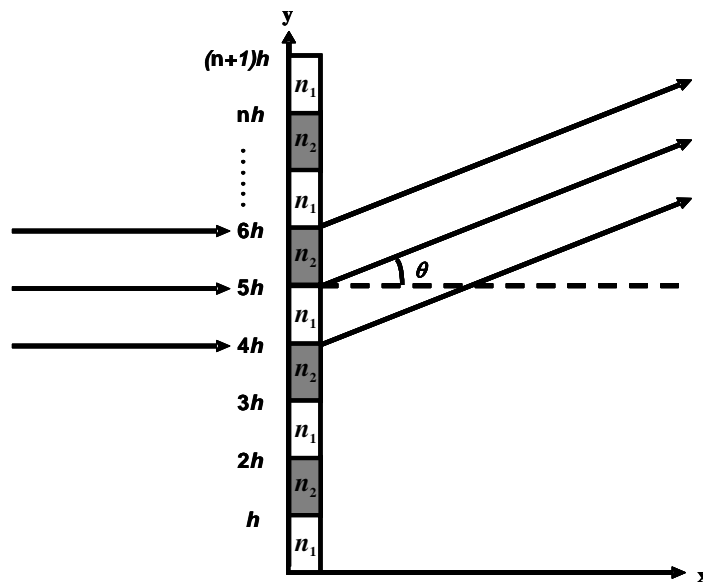


Figure 4-1 Schematic of a generic binary phase grating

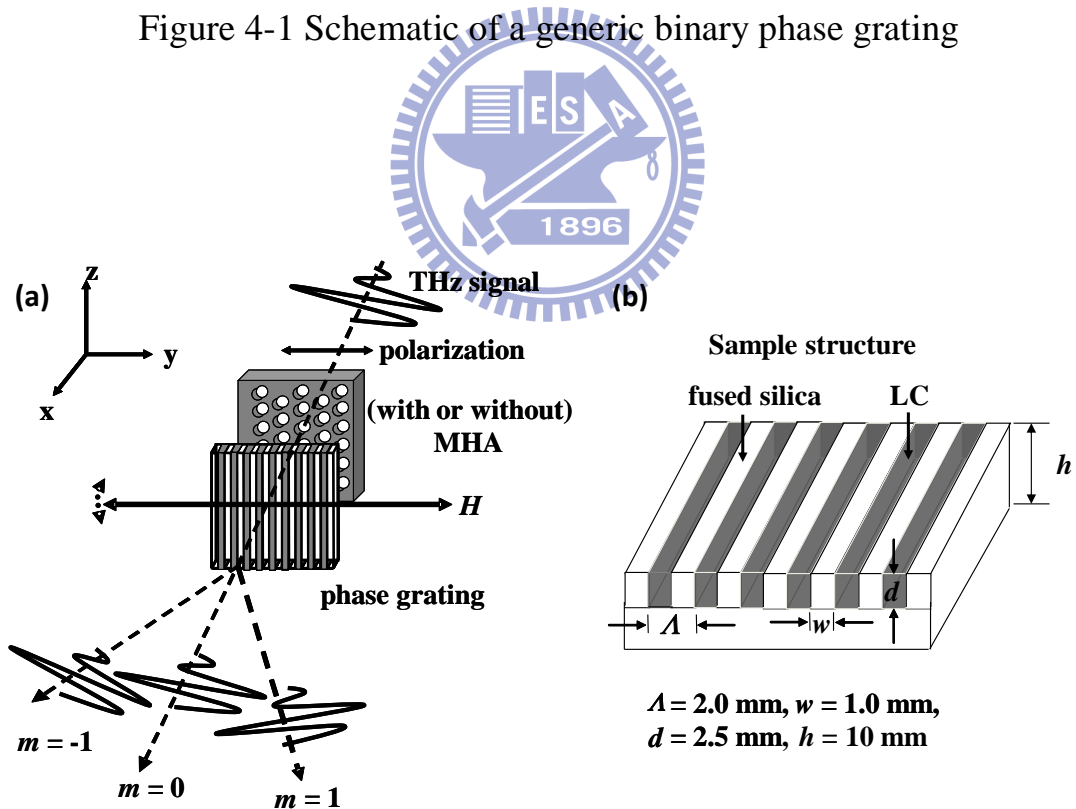


Figure 4-2 (a) Experimental setup; H: magnetic field, MHA: metallic hole array used as narrow band filter. (b) Structure of the LC phase grating; dimensions are shown. Another substrate (not shown) is on the top.

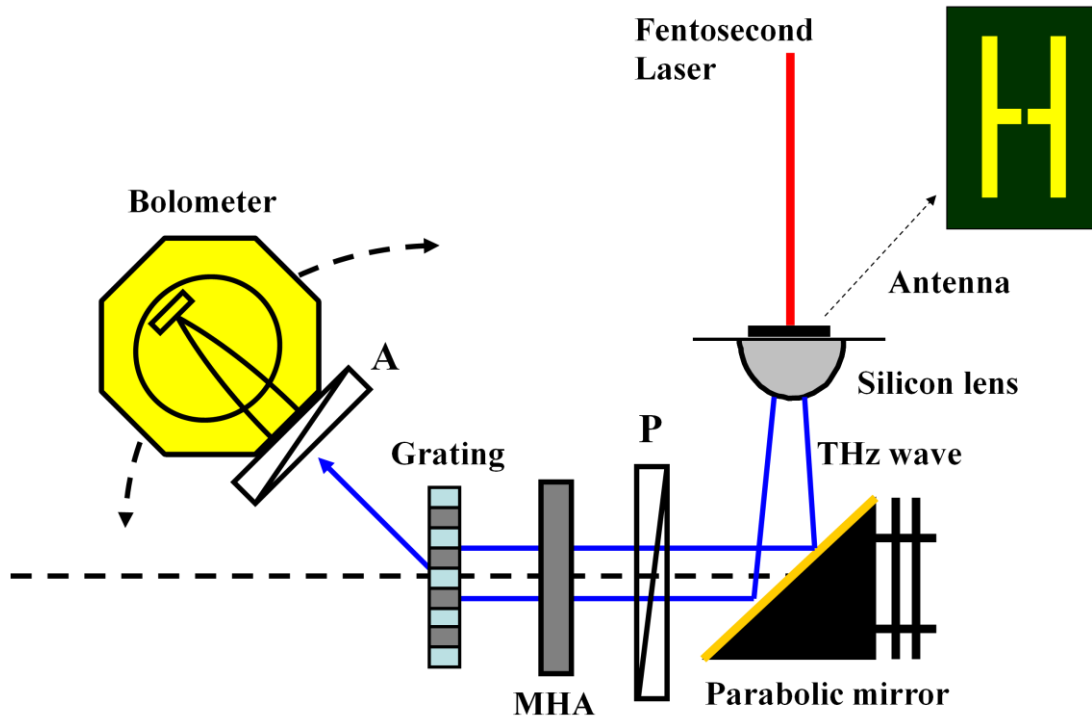


Figure 4-3 Construction of setup for grating diffraction profile measurement

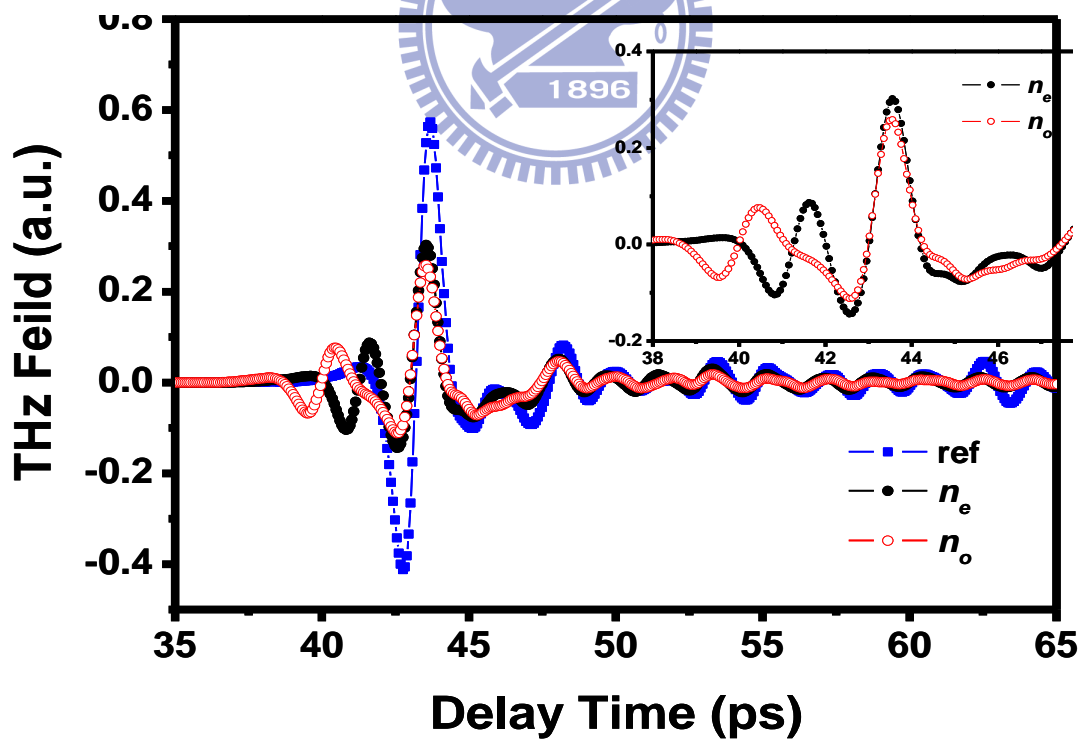


Figure 4-4 Temporal profiles of the 0th order diffracted THz pulses through the phase grating and that of a reference sample. The inset presented the magnified view for extraordinary and ordinary waves.

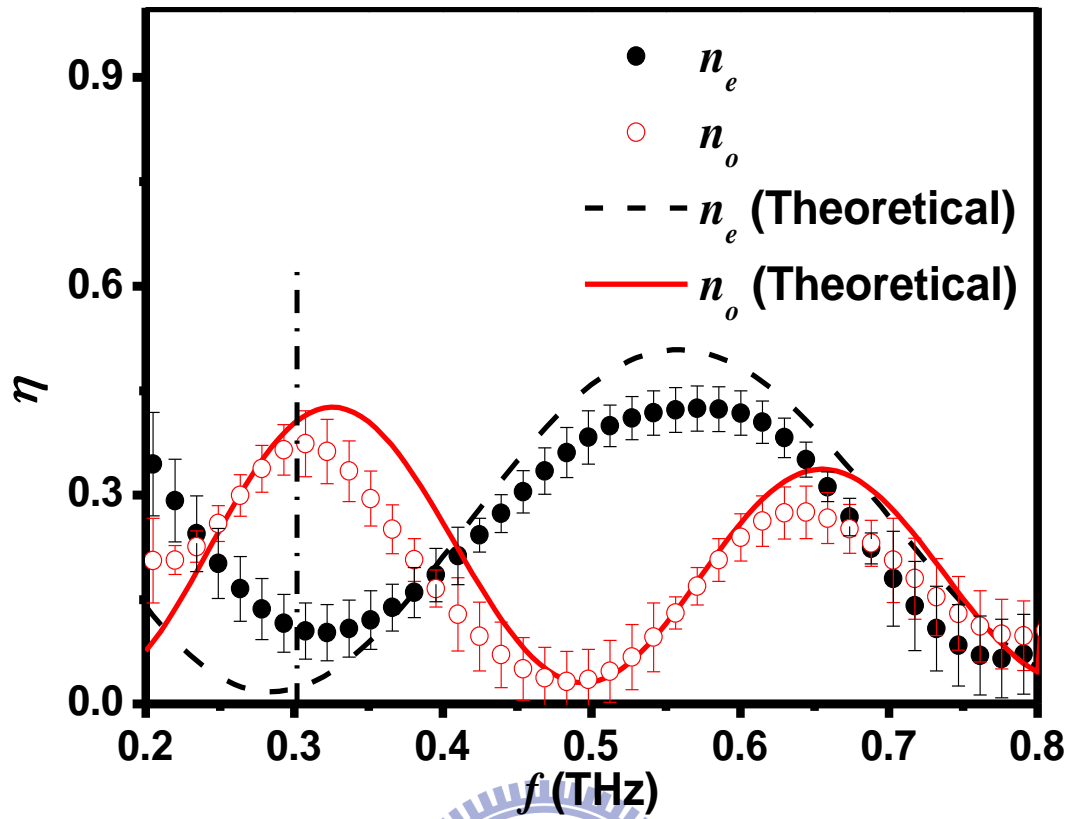


Figure 4-5 Diffraction efficiencies of the 0th order as a function of frequency. The solid and dashed lines are theoretical curves for ordinary and extraordinary waves. The open and the closed circles represented experimental result

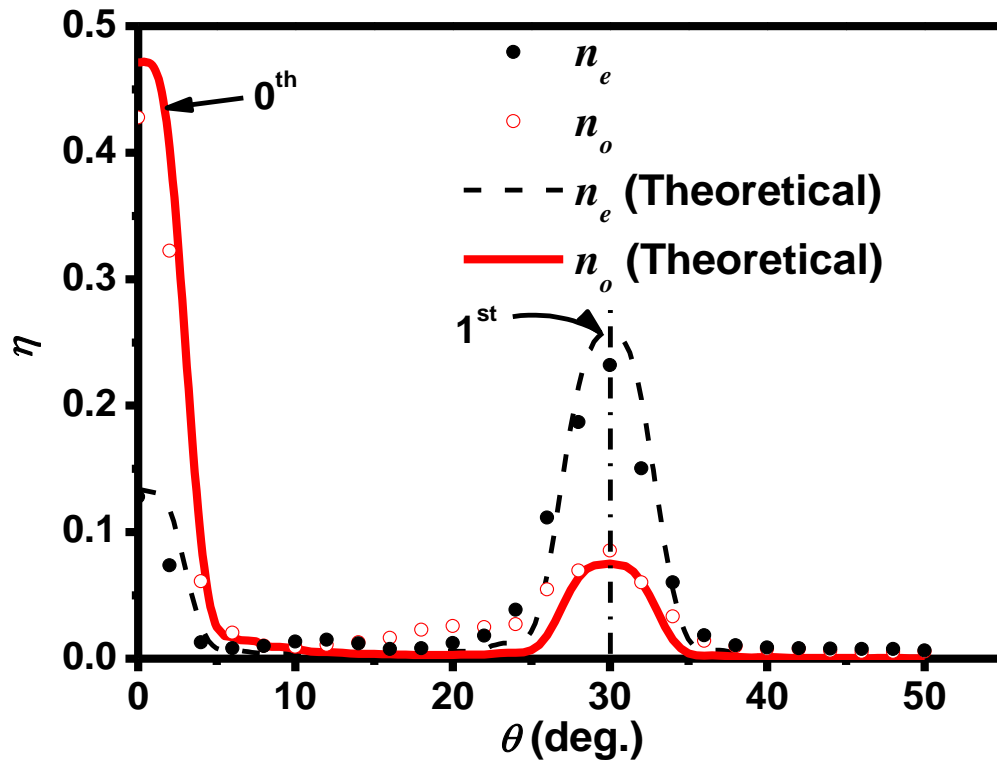
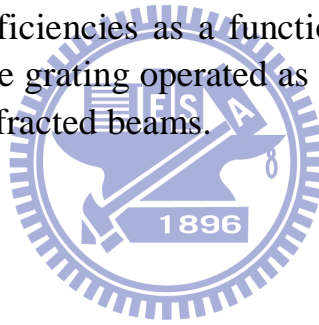


Figure 4-6 Diffraction efficiencies as a function of diffraction angle (θ) for the 0.3 THz-beam. The grating operated as a variable beam splitter for the 0th and 1st orders diffracted beams.



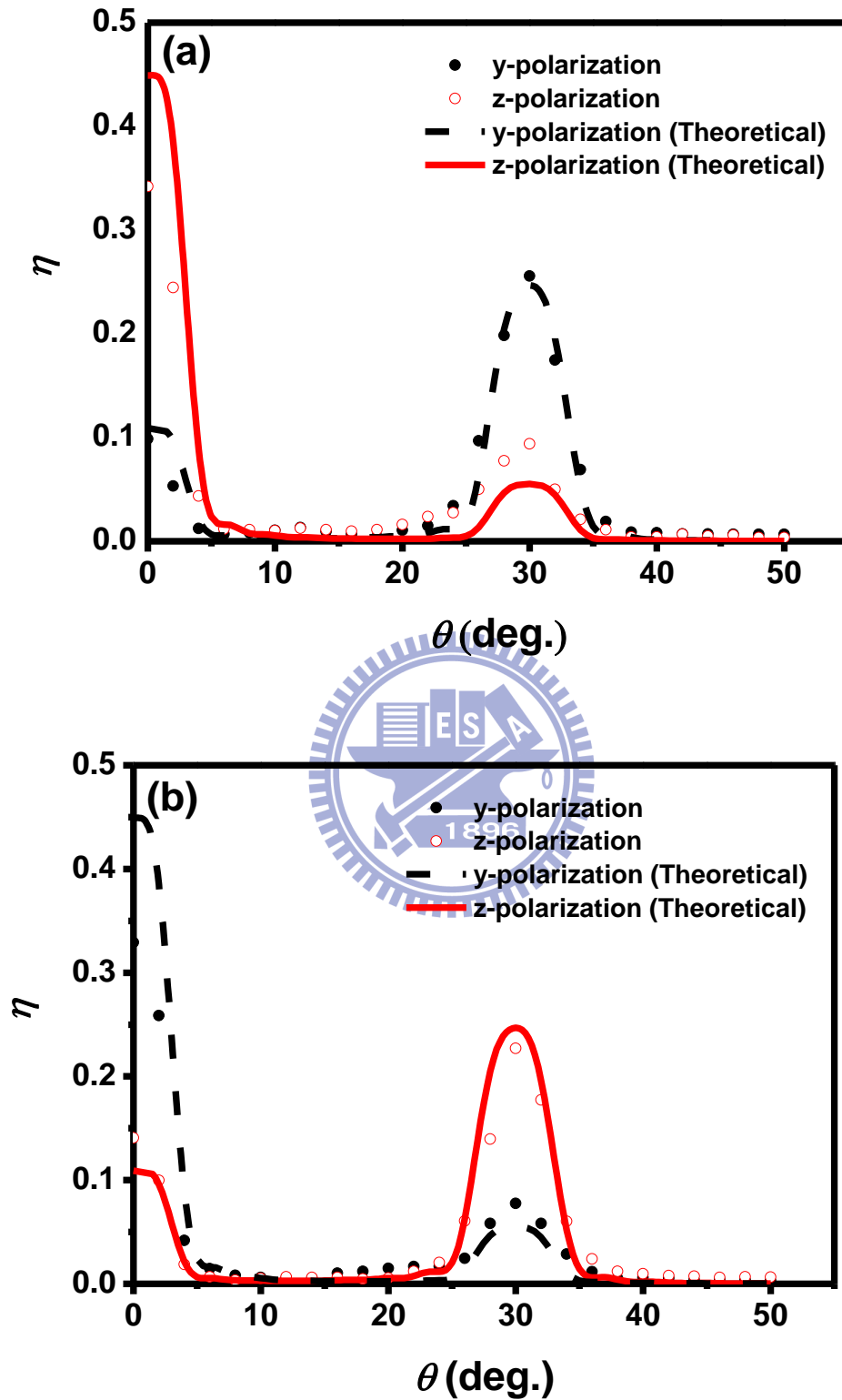


Figure 4-7 Polarization beam splitting using the LC phase grating. (a) Magnetic field was in the y-direction. (b) Magnetic field was in the z-direction.

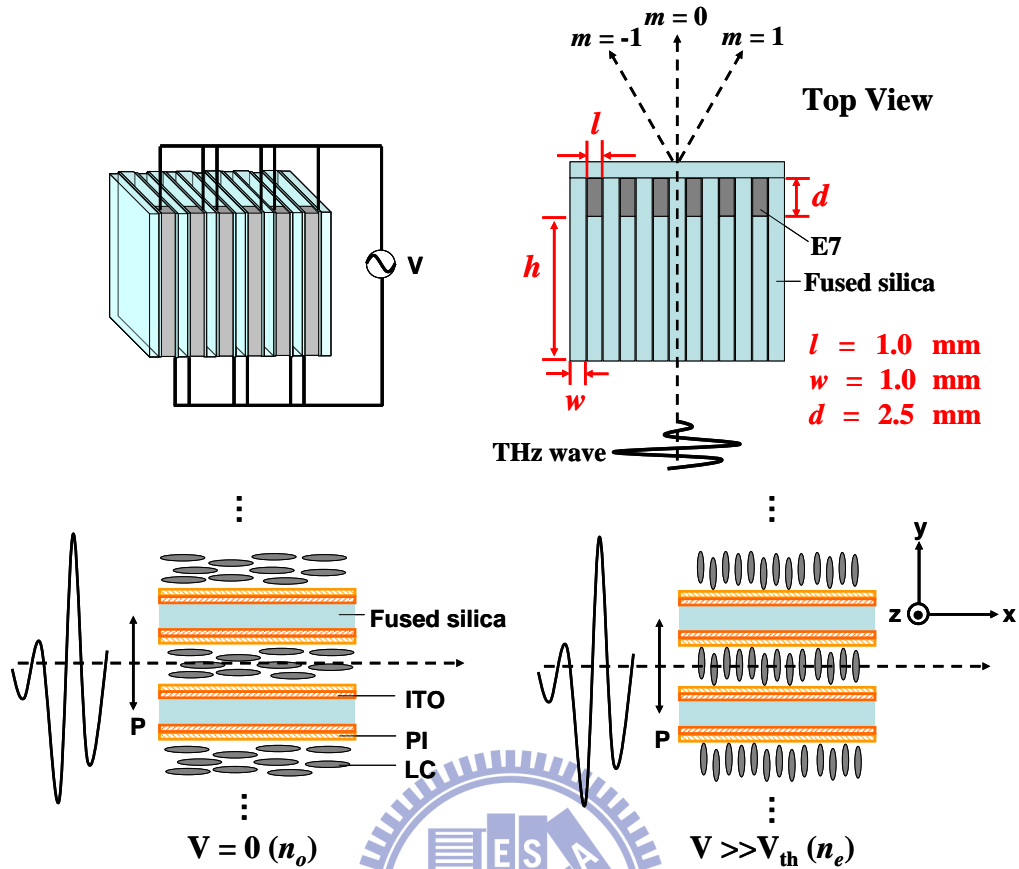


Figure 4-8 Schematic structure of the electrically controlled THz NLC phase grating. The dimensions of the structure are shown. P: polarization, ITO: Indium Tin Oxide, PI: polyimide, V_{th} : threshold voltage. Two different base dimensions of the sample, $h_1=17.5\text{mm}$ and $h_2=7.5\text{mm}$, are prepared to analyze the loss caused by the base.

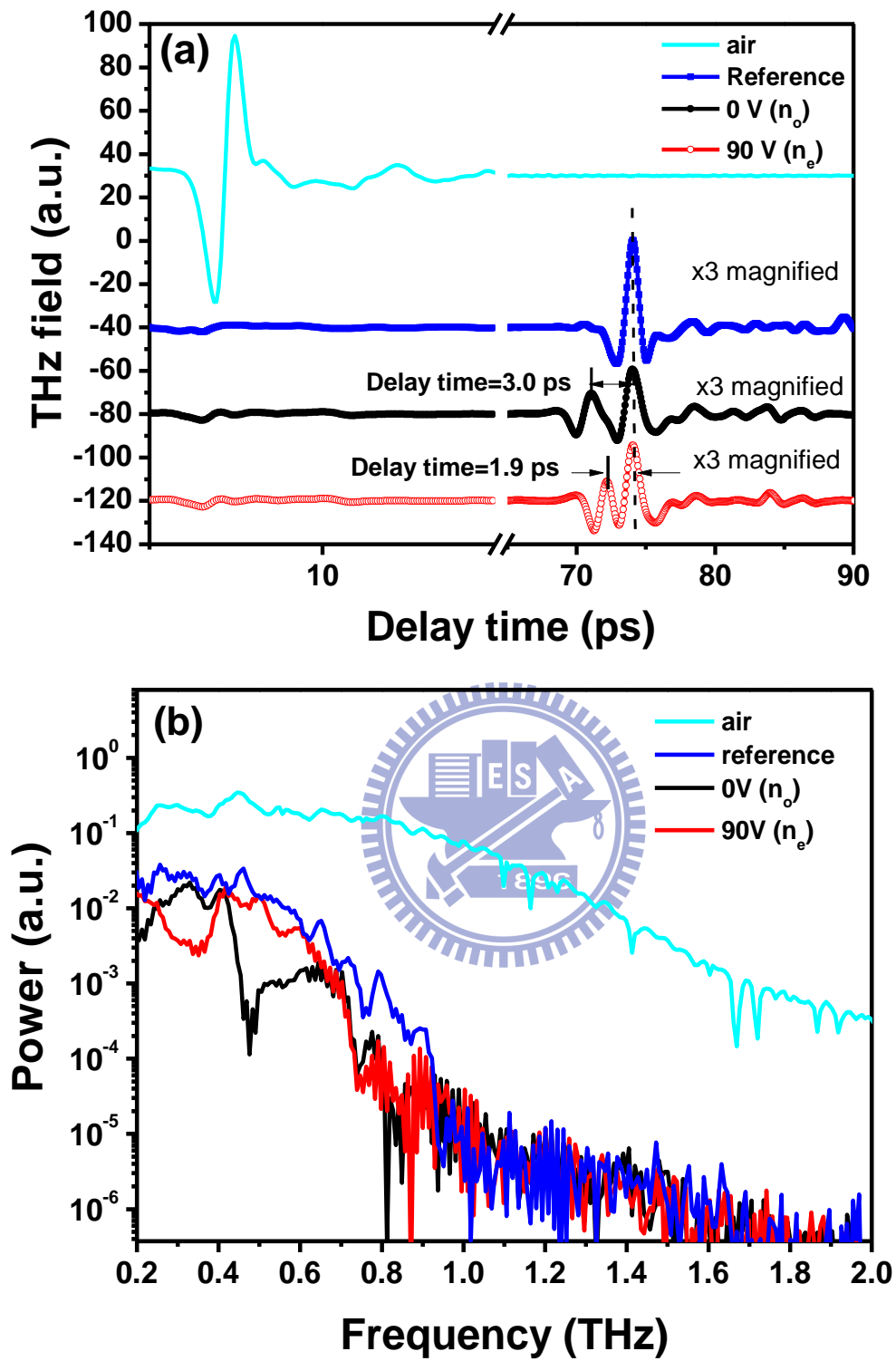


Figure 4-9 Time-domain (a) and spectral-domain (b) characteristics of the device. Explanations of the various curves are given in the text.

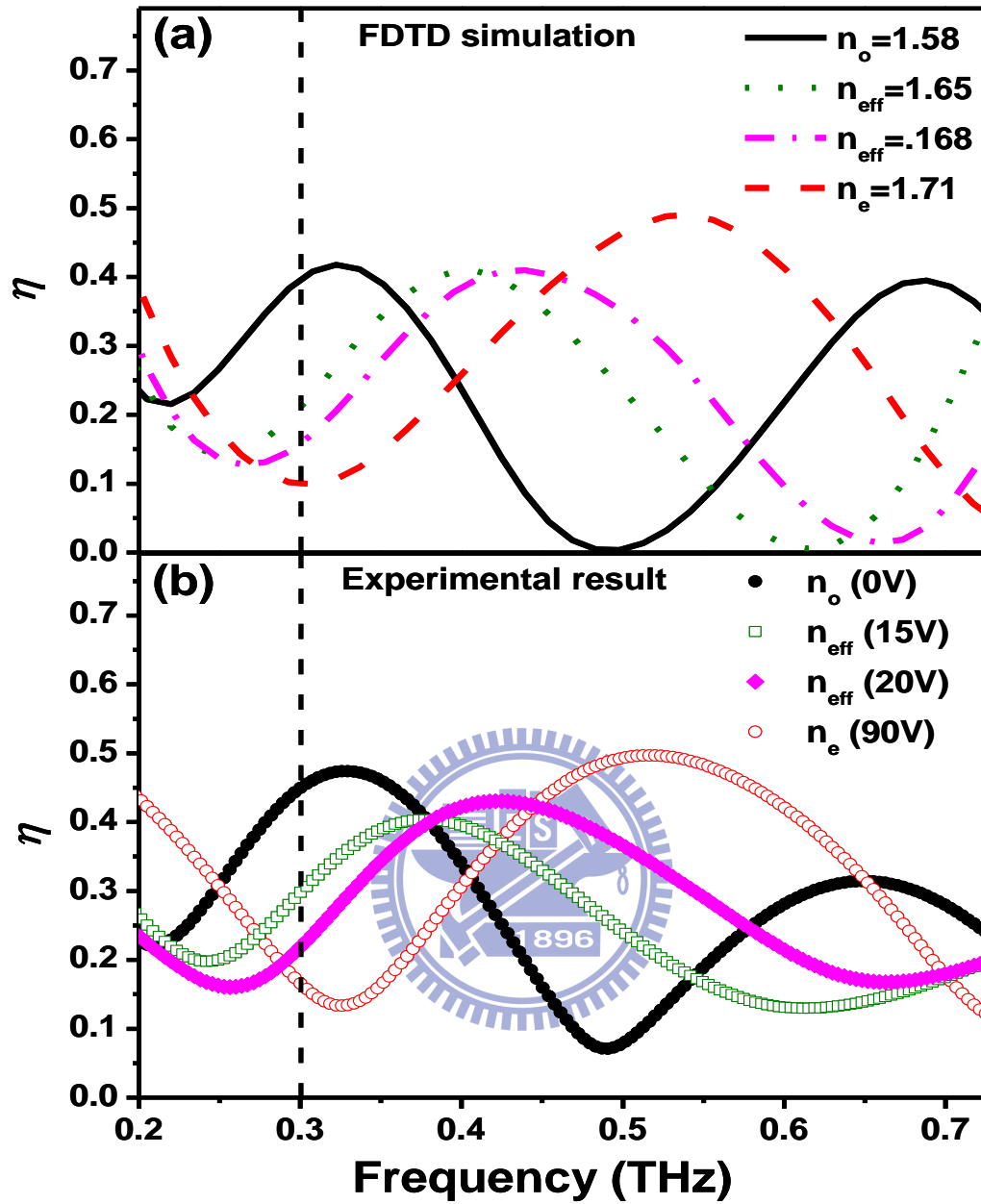


Figure 4-10 (a) FDTD simulation and (b) Experimental results of the frequency dependence of the 0th diffraction efficiencies of the phase grating operated at four applied voltages

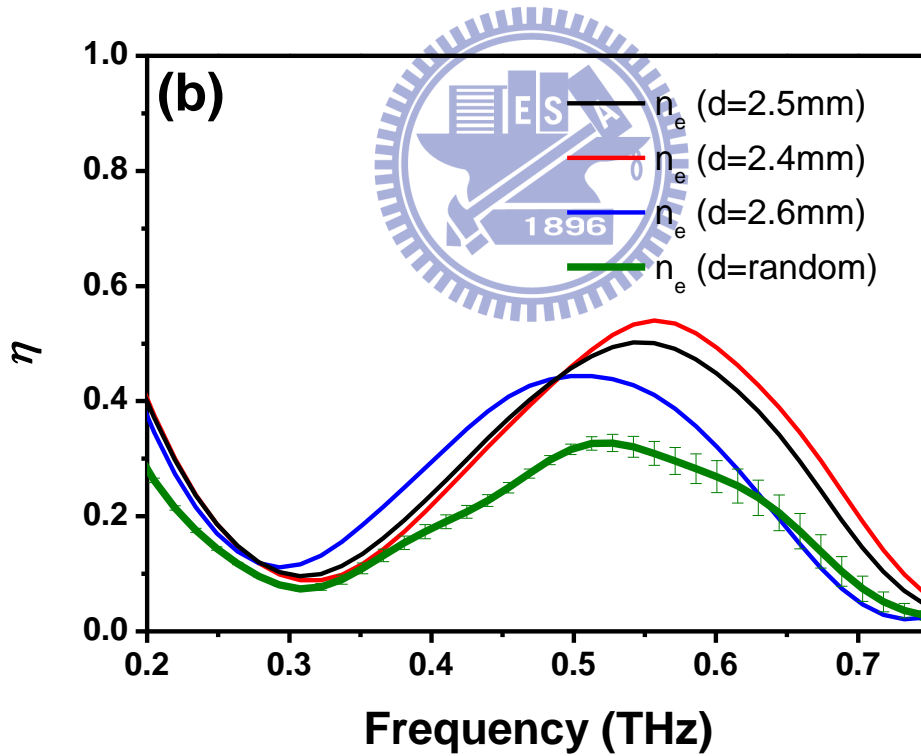
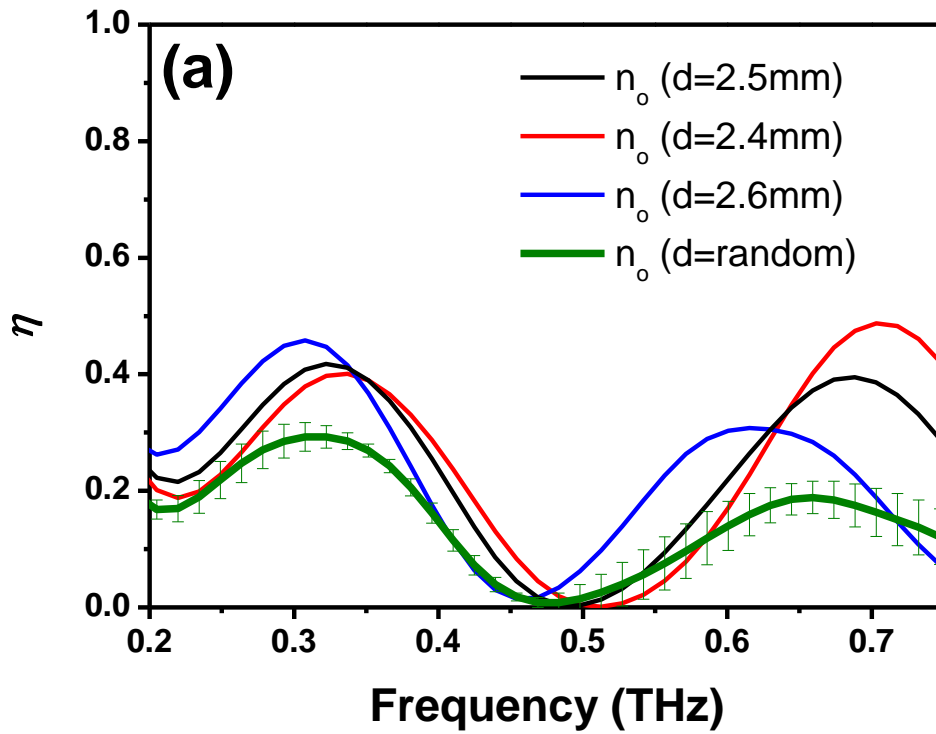


Figure 4-11 FDTD simulation - diffraction efficiency as a function of frequency for different thickness (a) o-wave (b) e-wave.

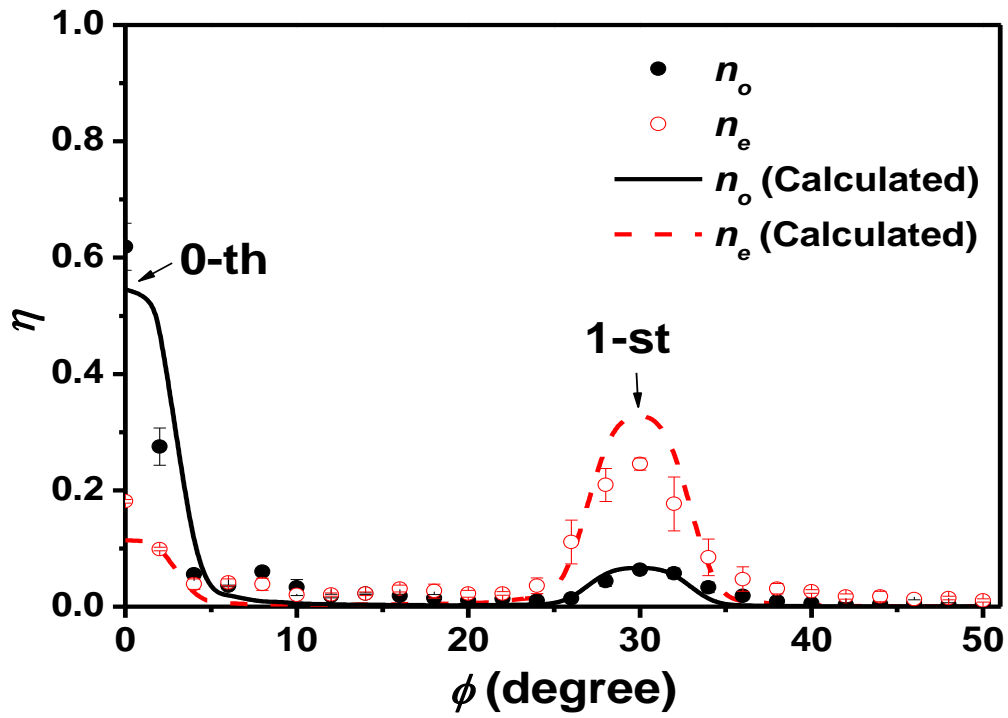


Figure 4-12 Diffraction efficiency as a function of diffraction angle for the 0.3-THz-beam



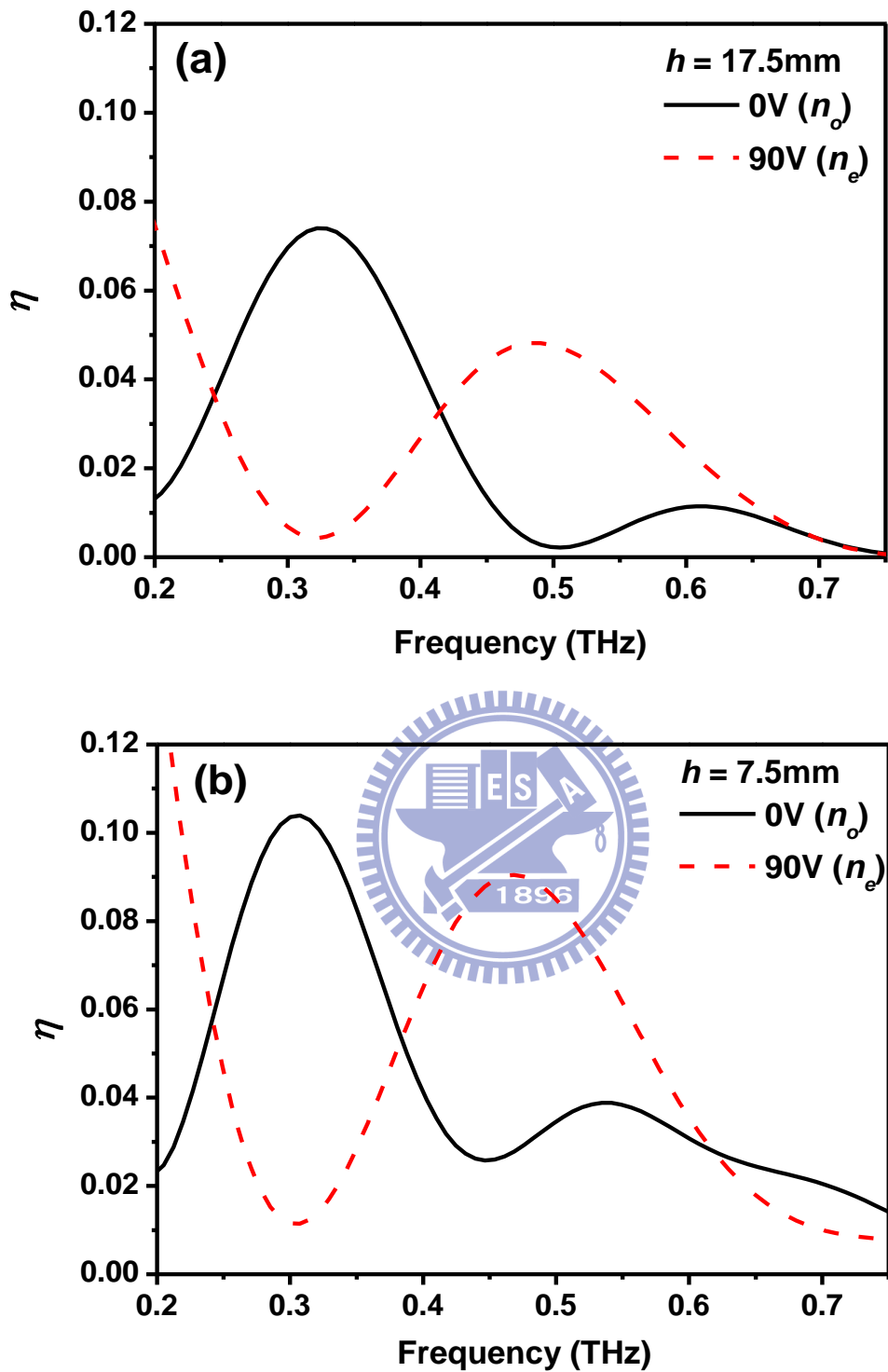


Figure 4-13 Ddiffraction efficiency of the devices (a) $h=17.5\text{mm}$ (b) $h=7.5\text{mm}$

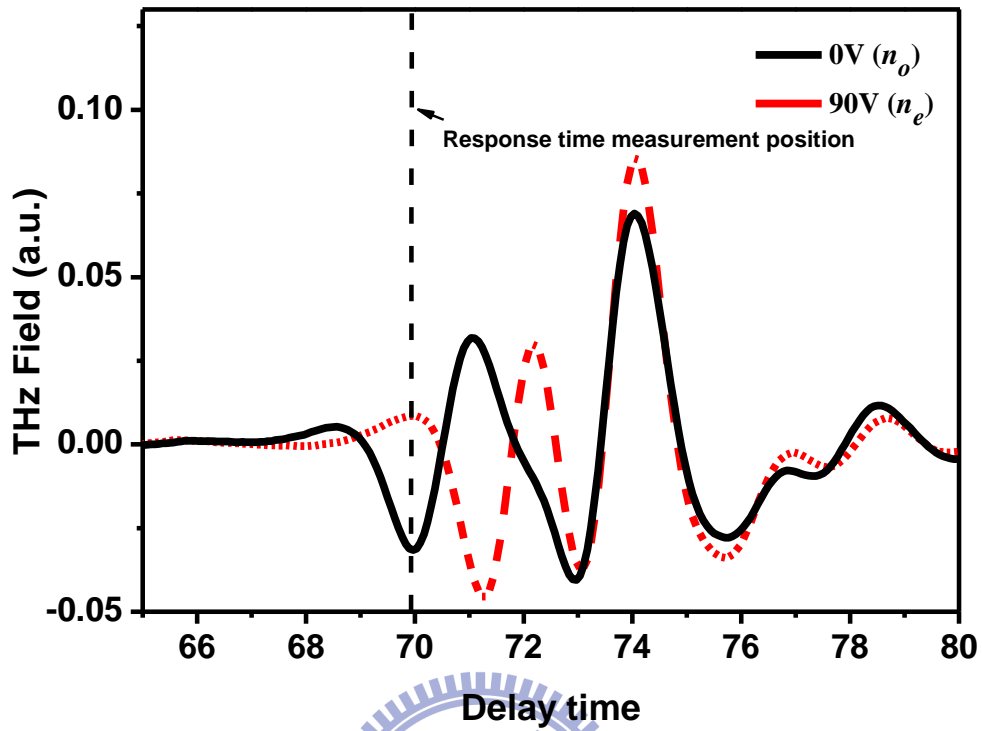


Figure 4-14 Signal profiles in time domain. The turn-on and turn-off times are measured by monitoring the pulse signal (electric field) variation in time domain with THz-TDS. The monitoring position of THz-TDS for response time measurement is shown.

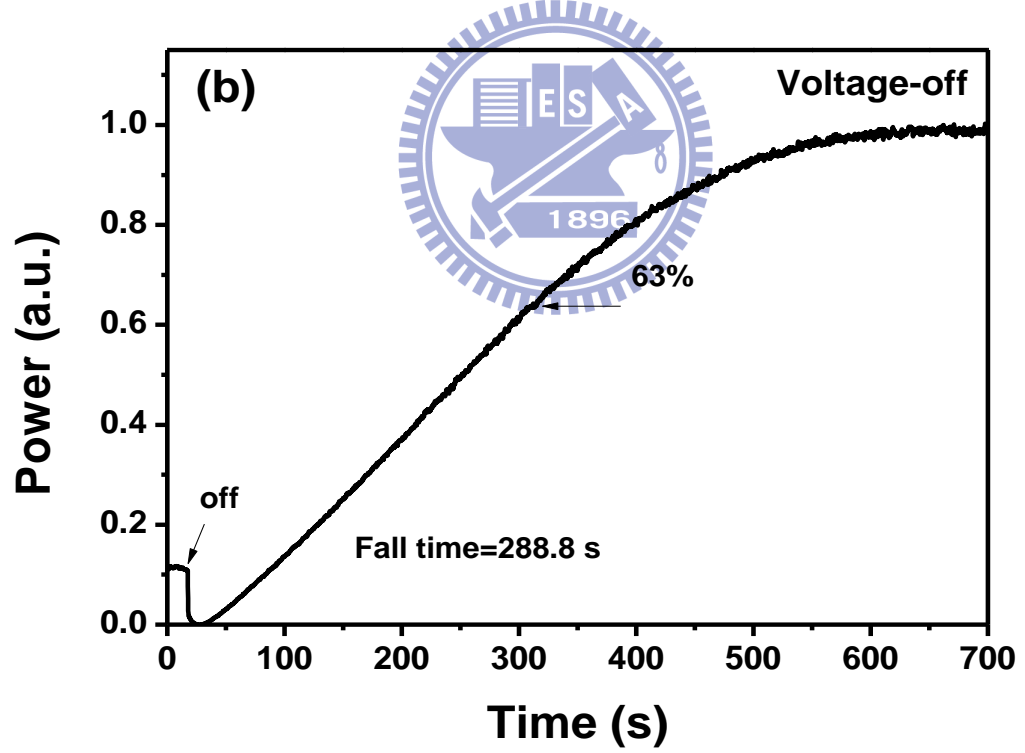
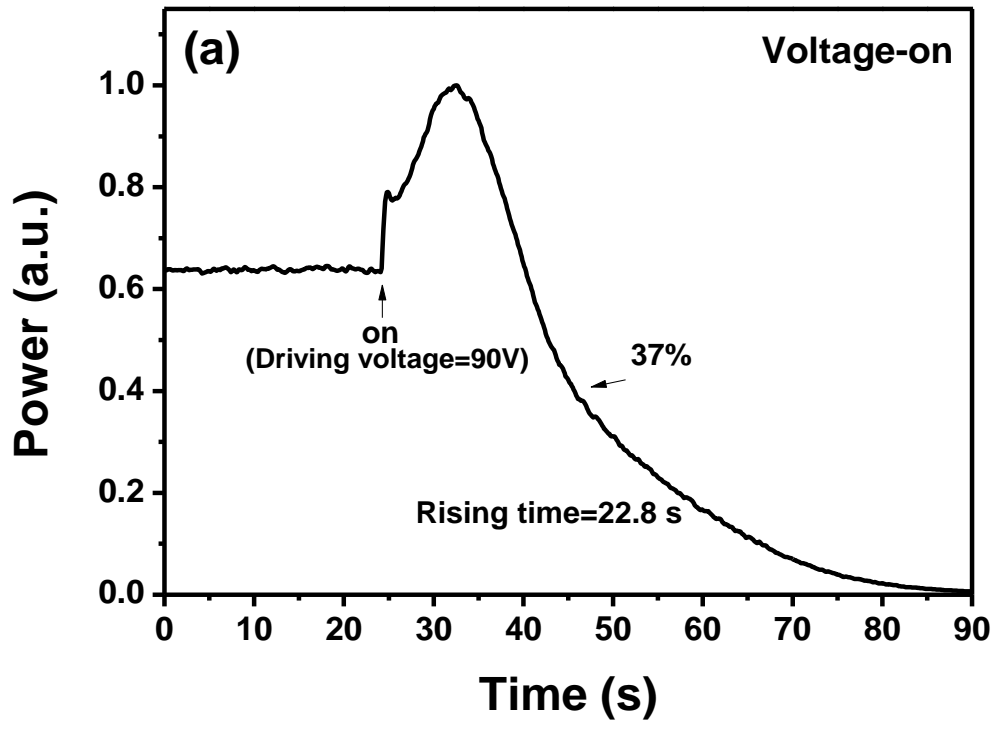


Figure 4-15 Response time of phase grating (a) turn-on (b) turn-off

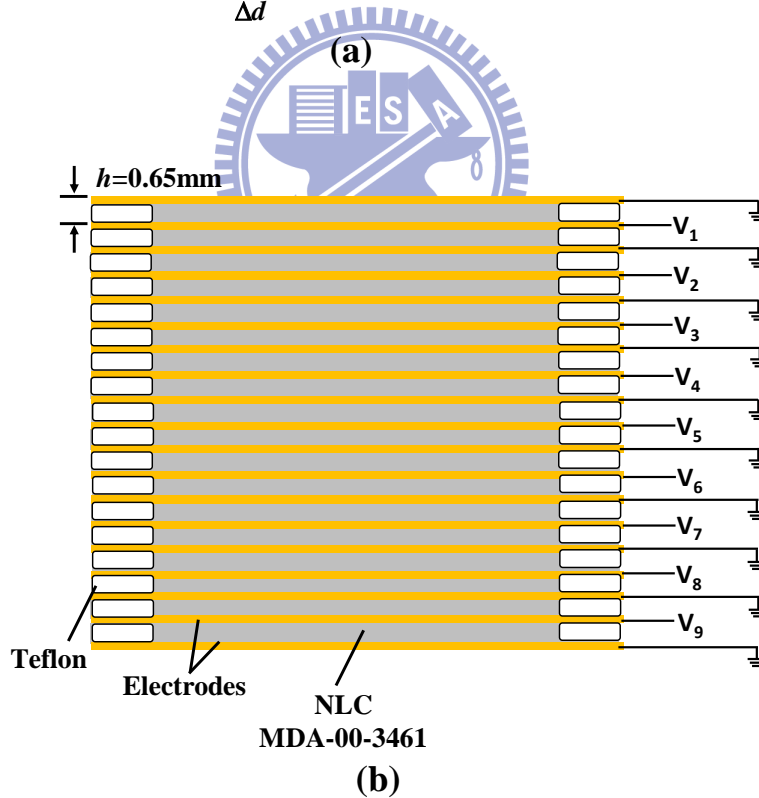
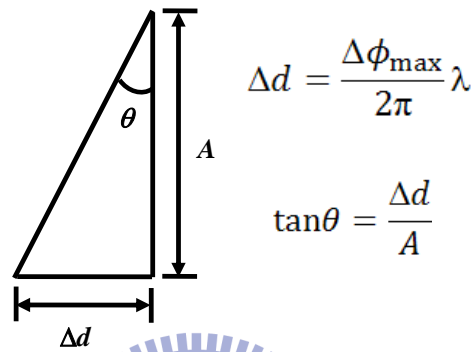
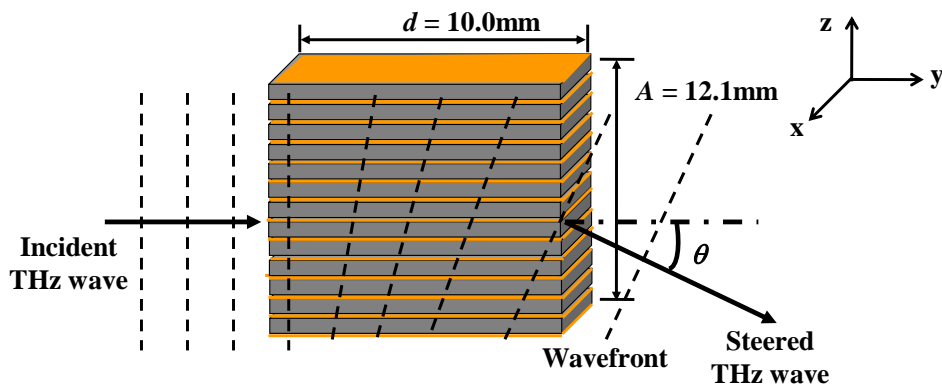


Figure 4-16 Schematic structure of the electrically controlled THz phase shifter array. (a) Construction of beam steering experiment and the relationship between steering angle θ , optical delay length Δd , and aperture A . (b) Structure of device with applying voltage arrangement. Dimensions of the structure are shown.

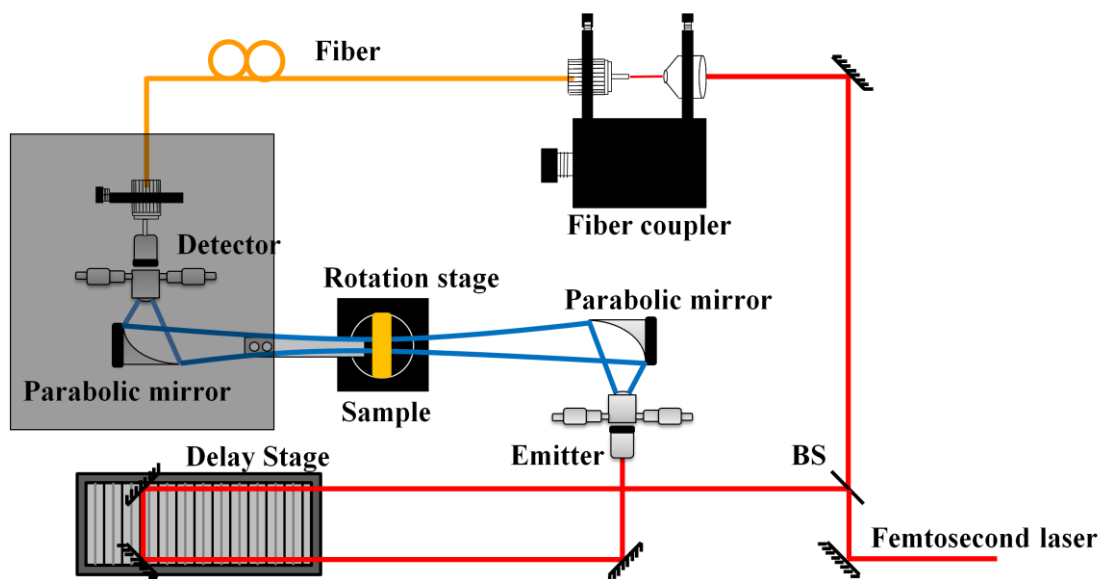


Figure 4-17 Improved THz-TDS. Probe beam is guided with a 1m-long optical fiber directly to the antenna. The detecting part is movable.

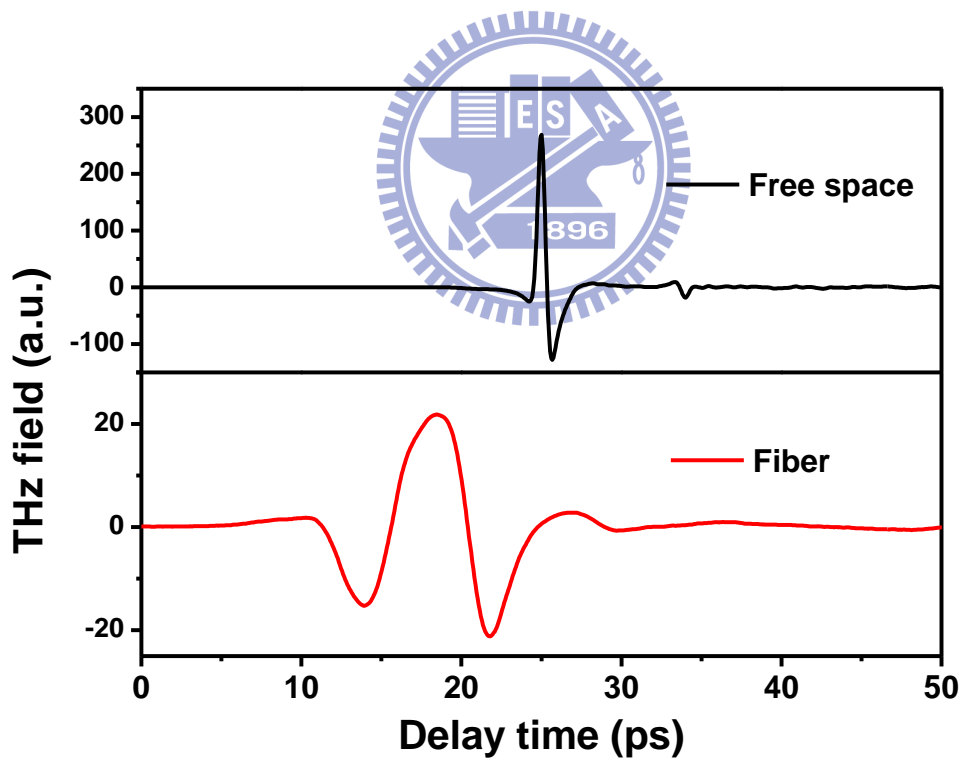


Figure 4-18 Comparison of THz signals in time domain between probe beam in free space (black line) and fiber-guided (red line).

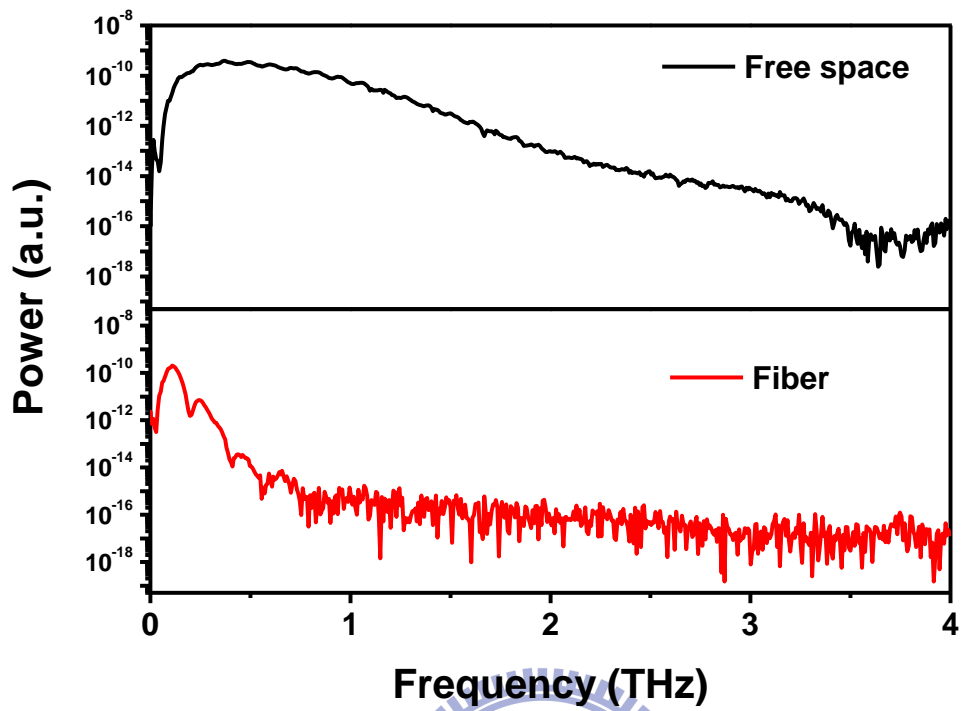


Figure 4-19 Comparison of THz spectra in frequency domain between probe beam in free space (black line) and fiber-guided (red line).

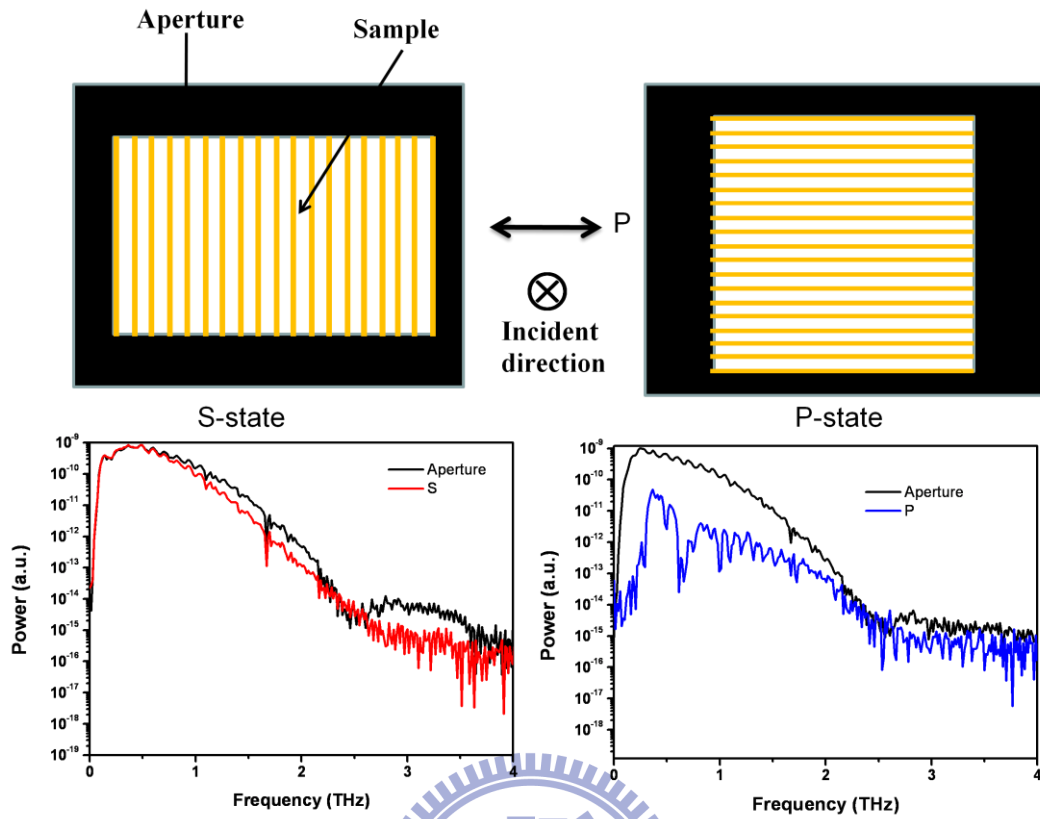


Figure 4-20 Transmitted properties of grating structure measured by THz-TDS. S-state or P-state is represented the polarization of THz wave (P) perpendicular or parallel to the electrodes, respectively.

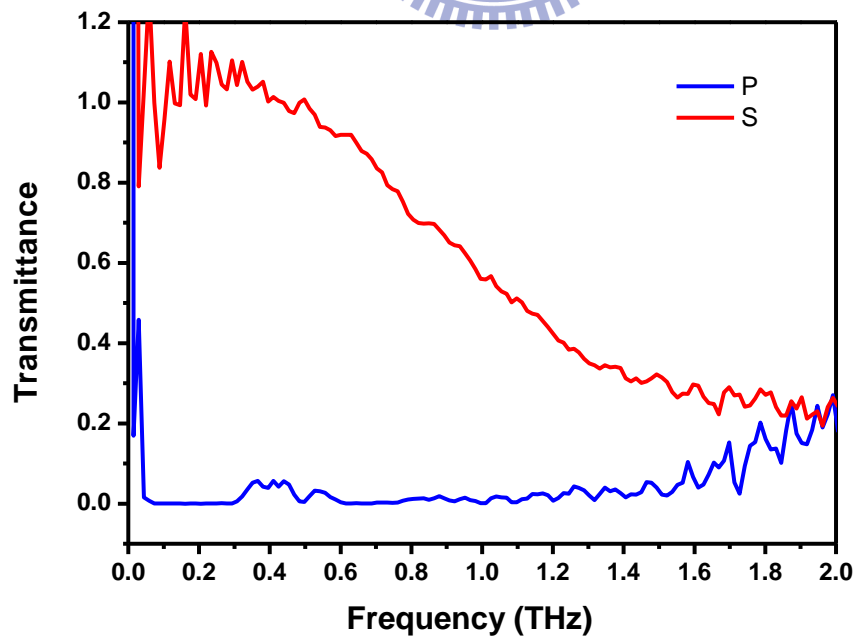


Figure 4-21 Transmittances of P-state and S-state measured by THz-TDS

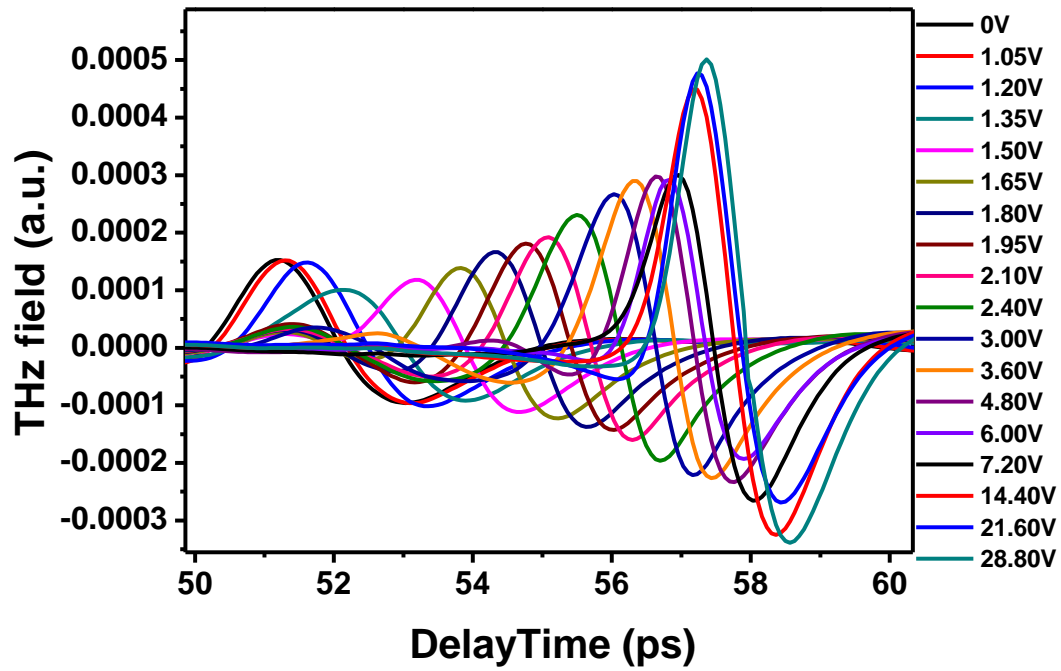


Figure 4-22 THz signal delay in time domain. Delay time increases as applying voltage increases.

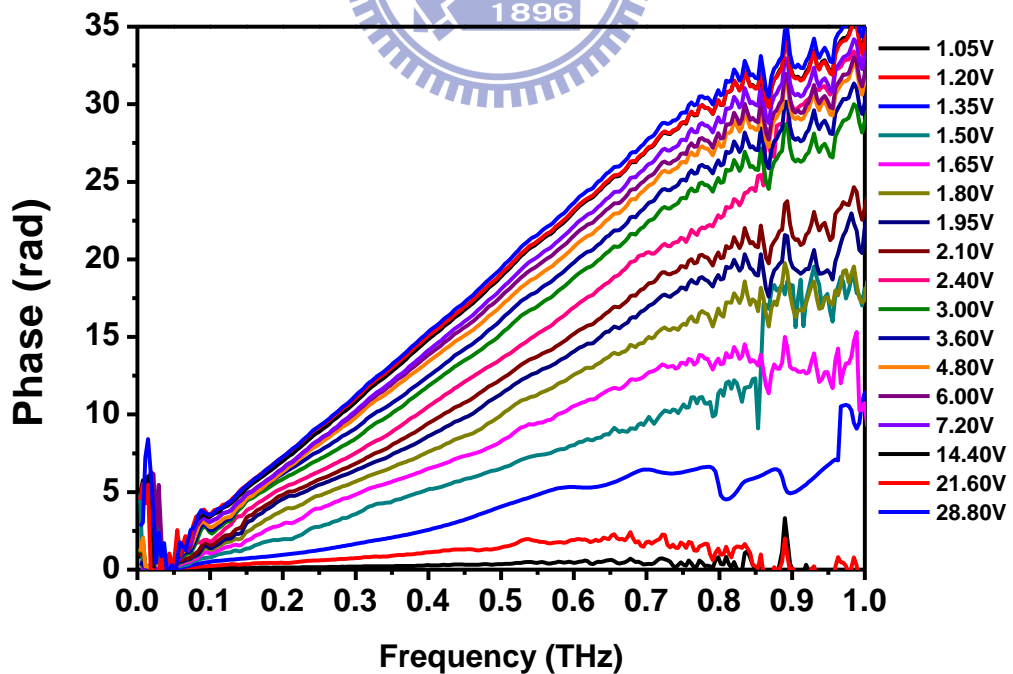


Figure 4-23 Spectra of phase shift of THz signal. Phase increases as applying voltage increases.

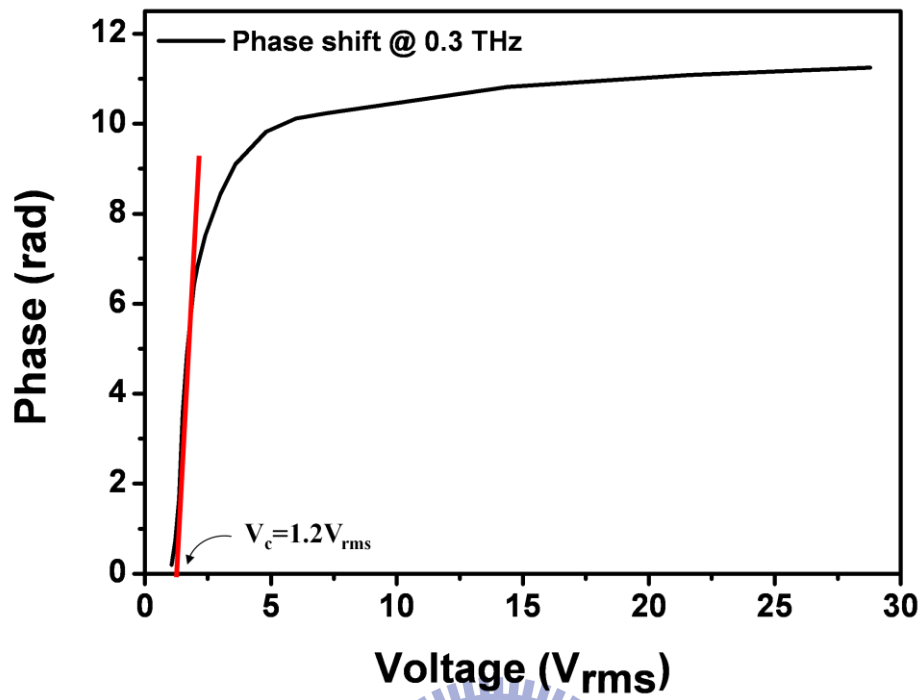


Figure 4-24 Phase shift at 0.3 THz as a function of the control voltage.



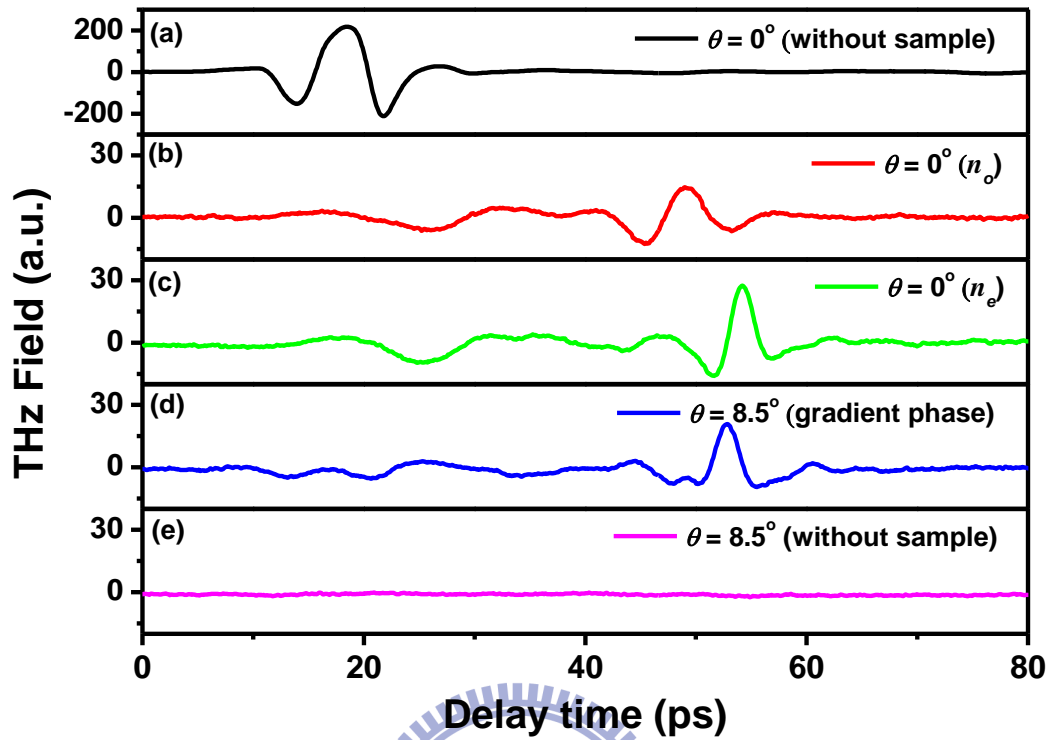


Figure 4-25 THz signals before steered at $\theta=0^\circ$: (a) without sample; with sample (b) at no-state, (c) at ne-state; steered signals at $\theta=8.5^\circ$: (d) sample applied voltage to yield gradient phase, (e) without sample.

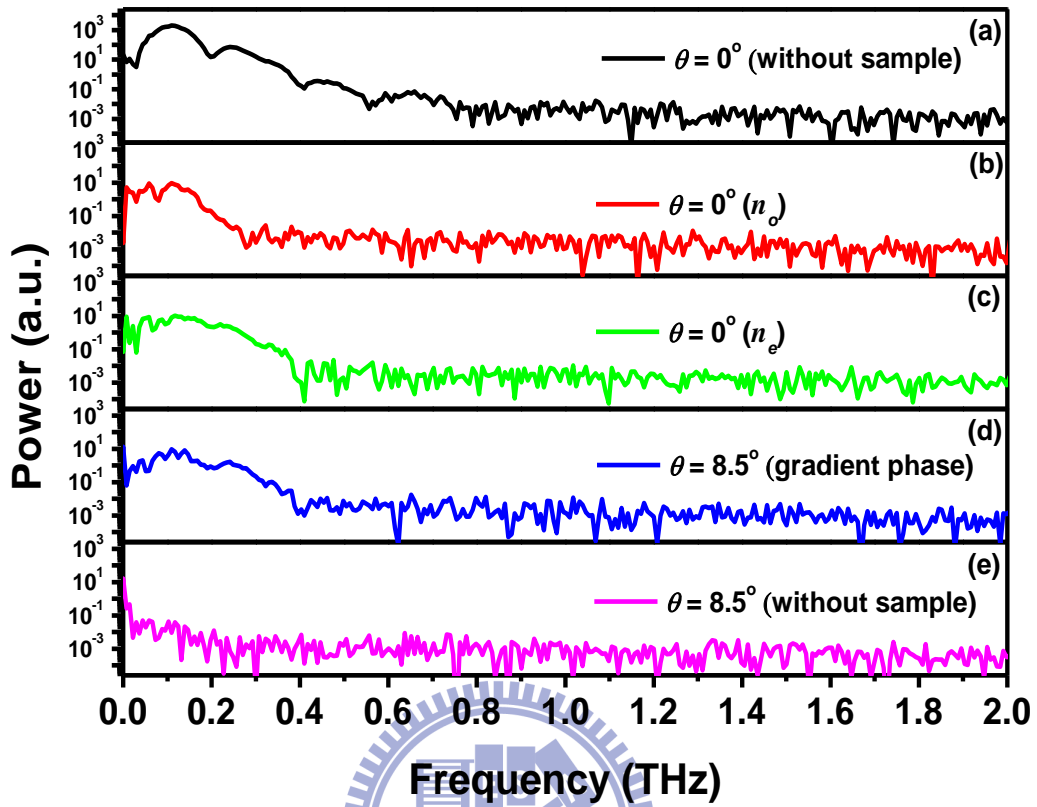


Figure 4-26 Spectra of THz signals before steered at $\theta=0^\circ$: (a) without sample; with sample (b) at no-state, (c) at ne-state; steered signals at $\theta=8.5^\circ$: (d) sample applied voltage to yield gradient phase, (e) without sample.

Chapter 5 Conclusions and Future Work

Conclusions

We constructed a Kerr-lens-mode locking Ti:sapphire laser with 450 mW maximum power, 90 MHz repetition rate, and 64 fs in pulse width. A conventional photoconductive antenna based THz-TDS was constructed that can characterize the broadband THz signal in the range, 0.1 - 4.0 THz. To investigate the THz beam steering, an improved THz-TDS with movable detecting part was constructed with an optical fiber. The improved THz-TDS can characterize the THz signal below 1.0 THz. It can detect the THz pulse directly and can be more convenient and lower cost than that using the liquid-helium-cooled Si bolometer.

Optical constants in the THz region are important to design the tunable THz devices. The materials for tunable devices design should have the properties of large birefringence and small absorption. We choose the fused silica and NLC E7 and MDA-00-3461 to fabricate our devices. The complex refractive indices of these materials were characterized by the conventional THz-TDS at room temperature 24.5°C. In the THz range, 0.2-2.0 THz, the complex refractive indices of fused silica are $n=1.95$, $\kappa < 0.01$. The ordinary and extraordinary indices of NLC E7 are $n_o = 1.58$, $n_e = 1.71$, $\kappa_o=0.03$, and $\kappa_e=0.01$, and which of NLC MDA-00-3461 are $n_o = 1.54$, $n_e = 1.72$, $\kappa_o=0.03$, and $\kappa_e=0.01$, respectively. In this frequency range, these materials do not show any sharp resonant absorption and clear dispersion. The studies of the optical

constants of NLC E7 and MDA-00-3461 in THz range show the attractive potential of the applications due to the comparable large birefringence and relative small extinction coefficient.

A magnetically controlled tunable LC phase grating for manipulating the THz wave at room temperature was demonstrated. The waveform of the broadband THz wave was modified in the time-domain and the spectral transmittance could be varied in the frequency-domain. The splitting ratio of the diffracted THz-beam (0.3 THz) polarized in a direction perpendicular to that of the grooves of the grating could be tuned from 4:1 to 1:2. Additionally, when the THz wave was polarized in any other direction, this device had the potential to operate as a polarizing beam splitter. The experimental results were in good agreement with theoretical calculations.

We have also demonstrated the electrically controlled liquid-crystal-based phase grating for manipulating the THz waves. This device can be utilized as a tunable terahertz beam splitter and its beam splitting ratio of the zeroth- to the first-order diffractions can be tuned from 10:1 to 1:1. The finite-differential time-domain simulation was used to investigate the diffraction effect of the phase grating. The experimental and simulation results were in general agreement. The signal losses of this device were also discussed and the insertion loss can be reduced by decreasing the thickness of fused silica plates in the base of the device. The phase grating does not have fast response because of the thick LC layer. As a result, the present device is not suitable for applications that require fast modulation. Instead, the device is excellent for

instrumentation or apparatus that require, e.g., a fixed beam splitting ratio with occasional fine tuning.

We demonstrated a grating structure phase shifter array that can be the THz shifter and THz beam steerer. For phase shift, applying the controlled voltages equally on the NLC layers of the device to vary the refractive index of NLC can shift the phase of THz signal. For beam steering, the broadband THz signal below 0.5 THz can be steered to the direction that has 8.5° with respect to the incident beam as the control voltages were varied to yield the phase gradient. The experimental results are in good agreement with theoretical predictions.

Future work

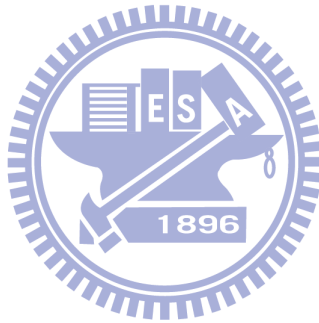


The devices we demonstrated have the relative thick NLC layers due to the larger wavelength in THz range. Therefore, the response times of the devices are relative slow, especially the turn-off time that can reach about several hundred seconds. The dual-frequency NLC is a solution to faster the relaxation time. The dual-frequency NLC has certain critical frequency that can switch the NLC either positive or negative dielectric anisotropy. Thus, we can apply the voltage both on o-state and e-state that can faster the response times. The other type LC, like blue phase, has fast response time is also the solution.

The insertion losses of the electrically controlled devices with grating structure can be estimate as stacked parallel-plate waveguides. The insertion losses are also large due to the relative thick NLC in

propagation length for THz wave. For practical applications, we can reduce the base of the device in propagation or find more suitable materials to reduce the conductor loss and dielectric loss.

For beam steering, we used the fiber-guided THz-TDS to characterize the steered THz wave. The system can only resolve the THz signal below 1THz because the laser pulse was broadened by dispersion. The laser pulse can be compressed with pre-compensating the positive group-velocity dispersion. Thus, the broader THz signal can be characterized.



Publication List

(a) Journal paper

1. Chia-Jen Lin, Guo-Teng Hong, and Ru-Pin Pan, "Alignment Control of Rubbed Polyimide Layers by UV-Irradiation," *Mol. Cryst. Liq. Cryst.*, Vol. 512, pp. 91/[1937]–99/[1945], 2009.
2. Chia-Jen Lin, Chuan-Hsien Lin, Cho-Fan Hsieh, Ru-Pin Pan, Yu-Tai Li, and Ci-Ling Pan, "Some Characteristics of a Liquid-Crystal Phase Grating for THz Waves," *Mol. Cryst. Liq. Cryst.*, Vol. 507, pp. 114–121, Jan 01, 2009.
3. Hsin-Ying Wu, Chih-Yu Wang, Chia-Jen Lin, Ru-Pin Pan, Song-Shiang Lin, Chein-Dhau Lee, and Chwung-Shan Kou, "Surface Alignment with High Pretilt Angle Using the Photoreactive Fluorinated Polymer Films," *Mol. Cryst. Liq. Cryst.*, Vol. 507, pp. 290–300, 2009.
4. Chia-Jen Lin, Chuan-Hsien Lin, Yu-Tai Li, Ru-Pin Pan, and Ci-Ling Pan, "Electrically Controlled Liquid Crystal Phase Grating for Terahertz Waves," *IEEE Photo. Tech. Lett.*, Vol. 21, No.11, pp730-732, June 1, 2009.
5. Hsin-Ying Wu, Chiu-Yu Wang, Chia-Jen Lin, Ru-Pin Pan, Song-Shiang Lin, Chein-Dhau Lee, and Chwung-Shan Kou "Mechanism in determining pretilt angle of liquid crystals aligned on fluorinated copolymer films," *J. Phys. D: Appl. Phys.* Vol. 42, 155303, Jul 7, 2009.
6. Chia-Jen Lin, Yu-Tai Li, Cho-Fan Hsieh, Ru-Pin Pan, and Ci-Ling Pan, "Manipulating Terahertz Wave by a Magnetically Tunable Liquid Crystal Phase Grating," *Opt. Exp.*, Vol. 16, No. 5, pp. 2995-3001, March 3, 2008.
7. Tsung-Ta Tang , Hsin-Ying Wu, Chia-Jen Lin, and Ru-Pin Pan, "A simple method of determining the pitch of a chiral nematic liquid crystal," *Mol. Cryst. Liq. Cryst.*, Vol. 478, pp. 143-150, 2007.
8. Tsung-Ta Tang, Hsin-Ying Wu, Chia-Jen Lin, Ru-Pin Pan, "Improved method for Measurement of liquid crystal azimuthal anchoring strength," *J. Appl. Phys.*, Vol. 102, pp. 063108, Sep. 2007.

(B) Conference paper

I. International conference paper

1. Ru-Pin Pan, Cheng-Wei Lai, Chia-Jen Lin, Cho-Fan Hsieh, Ci-Ling Pan, "ACHROMATIC LIQUID CRYSTAL PHASE PLATE FOR SHORT LASER PULSES," The 13th Topical Meeting on Optics of Liquid Crystals, Erice, Italy,

Sep 28- Oct 2, 2009.

2. Chia-Jen Lin, Guo-Teng Hong, and Ru-Pin Pan, "Alignment Control of Rubbed Polyimide Layers by UV-Irradiation," 22st International Liquid Crystal Conference, APP117, Jun 29-Jul 4, 2008, Jeju, Korea.
3. Chia-Jen Lin, Chuan-Hsien Lin, Yu-Tai Li, Cho-Fan Hsieh, Ru-Pin Pan, and Ci-Ling Pan, "Electrically Controlled Liquid Crystal Terahertz Phase Grating," 22st International Liquid Crystal Conference, APP117, Jun 29-Jul 4, 2008, Jeju, Korea.
4. Chia-Jen Lin, Yu-Tai Li, Cho-Fan Hsieh, Ru-Pin Pan, and Ci-Ling Pan, "Terahertz Beam Splitting by Tunable Liquid Crystal Phase Grating," Frontiers in Optics (FiO) 2007 the 91st OSA Annual Meeting, , San Jose, California, U.S.A., September 16-20, 2007.
5. Chia-Jen Lin, Yu-Tai Li, Cho-Fan Hsieh, Ru-Pin Pan, and Ci-Ling Pan, "Magnetically Controlled Liquid Crystal Terahertz Tunable Phase Grating," Paper P-10, 1st Asian-Pacific THz Photonics Workshop, Hsinchu, Taiwan, December 14, 2006.
6. Tsung-Ta Tang, Hsin-Ying Wu, Chia-Jen Lin, and Ru-Pin Pan, "A Simple Method to Determine the Pitch of Chiral Nematic Liquid Crystal," the 21st International Liquid Crystal Conference, Keystone, Colorado, U.S.A., July 02-07, 2006.

II. Local Conference Paper

1. 古正彬, 林家任, 趙如蘋, 潘犀靈, "液態晶體 MBBA 在兆赫波段下的光學特性," 2009 年中國液態晶體學會年會暨研討會, Hsinchu, Taiwan, Dec 18, 2009.
2. Chia-Jen Lin(林家任), Chuan-Hsien Lin(林俊賢), Ru-Pin Pan(趙如蘋), and Ci-Ling Pan(潘犀靈), "Insertion Loss Analysis of Electrically Controlled Liquid Crystal Phase Grating for Terahertz Waves," 2009 年中國液態晶體學會年會暨研討會, Hsinchu, Taiwan, Dec 18, 2009.
3. Cheng-Wei Lai, Chia-Jen Lin, Ru-Pin Pan and Ci-Ling Pan, "Liquid Crystal Achromatic Half Wave Plates for Ultrashort Laser Pulses," 2009 年中國液態晶體學會年會暨研討會, Hsinchu, Taiwan, Dec 18, 2009.
4. 賴呈暉(Cheng-Wei Lai), 林家任(Chia-Jen Lin), 趙如蘋(Ru-Pin Pan), 潘犀靈(Ci-Ling Pan), "超短脈衝雷射之可調式液晶消色差波長板," Optics and Photonics Taiwan, Taipei, Taiwan, Dec 11-12, 2009.
5. Chia-Jen Lin, Chuan-Hsien Lin, Ru-Pin Pan, and Ci-Ling Pan, "Terahertz Wave Manipulating by Electrically Controlled Liquid Crystal Phase Grating," Annual Meeting of ROC TLCS, PP-11, Hsinchu, Taiwan, December 19, 2008.

6. Chia-Jen Lin, Yu-Tai Li, Cho-Fan Hsieh, Ru-Pin Pan, and Ci-Ling Pan, "Tunable Liquid Crystal Phase Grating for Terahertz Beam Splitting," Annual Meeting of The Physical Society of Republic of China, aE-05, Hsinchu, Taiwan, January 28-30, 2008.
7. Chuan-Hsien Lin, Chia-Jen Lin, Ru-Pin Pan, and Ci-Ling Pan, "Photo-aligned Liquid Crystal Cell as an Electrically Controlled Terahertz Phase Grating," The Annual Meeting of The Physics Society of Republic of China, Taiwan, January 23-25, 2007.
8. 林家任、黎宇泰、謝卓帆、趙如蘋、潘犀靈, "可調制之磁控式兆赫波液晶相位光柵," 中國液態晶體學會年會暨研討會, December 22, 2006.
9. 洪國騰, 林家任, 湯宗達, 趙如蘋, "液晶於摩刷聚醯亞胺薄膜之光致重新配向研究," 中國液態晶體學會年會暨研討會, December 22, 2006.
10. 郭政穎, 湯宗達, 林家任, 趙如蘋, "陽極處理氧化鋁薄膜基板對液晶配向之研究", 2006 中國液態晶體學會年會暨研討會, PP-12, December 22, 2006.
11. 張佳瑩, 湯宗達, 林家任, 趙如蘋, "摩刷配向與紫外光配向之聚亞醯胺薄膜其相位延遲研究及與表面錨定強度之關係," 中國液態晶體學會年會暨研討會, PP-13, December 22, 2006.
12. Tsung-Ta Tang, Hsin-Ying Wu, Chia-Jen Lin, and Ru-Pin Pan, "Precision improvement for azimuthal anchoring strength determination of liquid crystal surface," Optics and Photonics Taiwan, Taiwan, paper GO-22, *ibid.*, December 15-16, 2006.
13. 洪國騰, 林家任, 趙如蘋, 溫度控制下之紫外光配向方法及性質研究," 中國液態晶體學會年會暨研討會," December 30, 2005.
14. Chia-Jen Lin, Tsung-Ta Tang, and Ru-Pin Pan, "Photo-induced Alignment of Polyimide with UV-Laser and Xenon Arc Lamp," The Annual Meeting of The Physics Society of Republic of China, Kaohsiung, February, 1-3, 2005.
15. 林家任, 趙如蘋, "紫外光照射配向膜之液晶光配向方法及性質研究," 中國液態晶體學會年會暨研討會, December 17, 2004.
16. C.J. Lin, Tsung-Ta Tang, and Ru-Pin Pan, "Photo-induced Alignment of Low-Molecular-Weight Photo-Cross-Linkable Composites with UV-light," The Annual Meeting of The Physical Society of Republic of China, Taiwan, February 9-11, 2004.
17. Chia-Jen Lin, Tsung-Ta Tang, and Ru-Pin Pan, "Photo-induced Alignment of Low-Molecular-Weight Photo-Cross-Linkable Composites with UV-light," The Annual Meeting of Taiwan Liquid Crystal Society, Hsinchu, Taiwan, December 19, 2003.
18. C. J. Lin, C. F. Hsieh, and T. Y. Fu, "Surface Diffusion of Pd Adatoms on W Surface", The Annual Meeting of the Physical Society of Republic of China,

Taiwan, February, 2001 (Poster Prize)

(c) Patent

台灣專利

1. 趙如蘋(Ru-Pin Chao), 潘犀靈(Ci-Ling Pan), 林家任(Chia-Jen Lin), 林俊賢 (Chuan-Hsien Lin), “兆赫波分束器裝置” Taiwan (ROC) patent being filed, # 097140108, October 20 2008

美國專利

2. Ru-Pin Chao, Ci-Ling Pan, Chia-Jen Lin, and Chuan-Hsien Lin, “Electrically tunable THz beam splitter using liquid crystal phase grating,” US applying.



Curriculum Vitae

Biography:

Name: Chia-Jen Lin (林家任)

Data of Birth: June 10th, 1979

Sex: Male

Nationality: Taiwan (R.O.C.)

E-mail: allen0610.ep93g@nctu.edu.tw



Education:

- 9/2004~ 6/2010 **Ph.D.** in Department of Electrophysics, National Chiao-Tung University, Hsinchu, Taiwan.
- 9/2002~6/2004 **M.S.** in Department of Electrophysics, National Chiao-Tung University, Hsinchu, Taiwan.
- 9/1997~6/2001 **B.S.** in Department of Physics, National Taiwan Normal University, Taipei, Taiwan.

Specialties and Research Experience:

1. Ultrafast laser and THz technology:

- Assembling the commercial Kerr-lens mode-locking laser with 50fs pulse width
- THz time-domain spectroscopy with LT-GaAs photoconductive antenna

- Other THz detecting technique such as liquid-He-cooling Si bolometer, Fourier transform infrared (FTIR) spectroscopy

2. Tunable liquid crystal devices for THz wave

- Magnetically controlled phase grating
- Electrically controlled LC phase grating
- Electrically controlled phase shifter array for THz beam steering
- Tunable achromatic waveplates

3. Liquid crystal applications

- Surface alignment such as rubbing technique, photoalignment technique, polymer-stabilized alignment
- LC based devices such as filters, gratings, phase shifters , waveplates

4. Software programming and computer modeling

- LabVIEW programming to control the experimental components
- Rsoft for the finite differential time-domain (FDTD) simulations
- COMSOL Multiphysics for the finite element method calculation
- SolidWorks for devices design
- Mathematical and data analysis software: Mathematica, Mathcad, and Origin

Honors and Awards:

2008 Student Traveling Award, International Liquid Crystal Conference

2004 Scholarship of Wintek Corporation, Wintek Corporation

2001 Superior Report Award, National Science Council Project for undergraduate student

2001 Best Poster Award, The Physics Society of Republic of China
Annual Conference

Teaching Experience:

• **Teaching assistant:**

Department of Electrophysics, National Chiao-Tung University
Hsinchu, Taiwan, 06/2002- 06/2009

Job description: To give lectures to undergraduate students in
fundamental Physics course and assist graduate students in liquid
crystal experiments

• **Physics Teacher:**

Taipei first girls high school, Taipei, Taiwan, 07/2001-06/2002

Job description: To give Physics lectures and guide students in
scientific experiments

